

Warming does not delay the start of autumnal leaf coloration but slows its progress rate

Nan Jiang^{1,2}  | Miaogen Shen²  | Philippe Ciais³ | Matteo Campioli⁴ | Josep Peñuelas^{5,6} | Christian Körner⁷ | Ruyin Cao⁸ | Shilong Piao^{1,9}  | Licong Liu² | Shiping Wang¹ | Eryuan Liang¹  | Nicolas Delapierre¹⁰ | Kamel Soudani¹⁰ | Yuhan Rao¹¹ | Leonardo Montagnani^{12,13} | Lukas Hörtnagl¹⁴ | Eugénie Paul-Limoges¹⁵ | Ranga Myneni¹⁶ | Georg Wohlfahrt¹⁷ | Yongshuo Fu¹⁸ | Ladislav Šigut¹⁹ | Andrej Varlagin²⁰ | Jin Chen² | Yanhong Tang⁹ | Wenwu Zhao²

¹State Key Laboratory of Tibetan Plateau Earth System, Resources and Environment (TPESRE), Institute of Tibetan Plateau Research, Chinese Academy of Sciences, Beijing, China

²State Key Laboratory of Earth Surface Processes and Resource Ecology, Faculty of Geographical Science, Beijing Normal University, Beijing, China

³Laboratoire des Sciences du Climat et de l'Environnement (LSCE), CEA CNRS UVSQ, Gif Sur Yvette, France

⁴Centre of Excellence PLECO (Plants and Ecosystems), Department of Biology, University of Antwerp, Wilrijk, Belgium

⁵CSIC, Global Ecology Unit CREAM-CEAB-UAB, Bellaterra, Spain

⁶CREAF, Cerdanyola del Vallès, Spain

⁷Institute of Botany, University of Basel, Basel, Switzerland

⁸School of Resources and Environment, University of Electronic Science and Technology of China, Chengdu, China

⁹College of Urban and Environmental Sciences, Peking University, Beijing, China

¹⁰CNRS, AgroParisTech, Ecologie Systématique et Evolution, Université Paris-Saclay, Orsay, France

¹¹North Carolina Institute for Climate Studies, North Carolina State University, Asheville, North Carolina, USA

¹²Forest Service, Autonomous Province of Bolzano-Bozen, Bolzano-Bozen, Italy

¹³Faculty of Science and Technology, Free University of Bolzano, Bolzano, Italy

¹⁴Department of Environmental Systems Science, Institute of Agricultural Sciences, ETH Zurich, Zurich, Switzerland

¹⁵Department of Geography, University of Zurich, Zurich, Switzerland

¹⁶Department of Earth and Environment, Boston University, Boston, Massachusetts, USA

¹⁷Department of Ecology, University of Innsbruck, Innsbruck, Austria

¹⁸College of Water Sciences, Beijing Normal University, Beijing, China

¹⁹Department of Matter and Energy Fluxes, Global Change Research Institute of the Czech Academy of Sciences, Brno, Czech Republic

²⁰A.N. Severtsov Institute of Ecology and Evolution, Russian Academy of Sciences, Moscow, Russia

Correspondence

Miaogen Shen, State Key Laboratory of Earth Surface Processes and Resource Ecology, Faculty of Geographical Science, Beijing Normal University, Beijing 100875, China.

Email: shen.miaogen@gmail.com

Handling Editor: Stephanie Pau

Abstract

Aim: Initiation of autumnal leaf senescence is crucial for plant overwintering and ecosystem dynamics. Previous studies have focused on the advanced stages of autumnal leaf senescence and reported that climatic warming delayed senescence, despite the fundamental differences among the stages of senescence. However, the timing of onset of leaf coloration (D_{LCO}), the earliest visual sign of senescence, has rarely been studied. Here, we assessed the response of D_{LCO} to temperature.

Location: 30–75° N in the Northern Hemisphere.

Time period: 2000–2018.

Major taxa studied: Deciduous vegetation.

Methods: We retrieved D_{LCO} from high-temporal-resolution satellite data, which were then validated by PhenoCam observations. We investigated the temporal changes in D_{LCO} and the relationship between D_{LCO} and temperature by using satellite and ground observations.

Results: D_{LCO} was not significantly ($p > .05$) delayed between 2000 and 2018 in 94% of the area. D_{LCO} was positively ($p < .05$) correlated with pre- D_{LCO} mean daily minimum temperature (T_{min}) in only 9% of the area, whereas the end of leaf coloration (D_{LCE}) was positively correlated with pre- D_{LCE} mean T_{min} over a larger area (34%). Further analyses showed that warming slowed the progress of leaf coloration. Interestingly, D_{LCO} was less responsive to pre- D_{LCO} mean T_{min} in areas where daylength was longer across the Northern Hemisphere, particularly for woody vegetation.

Main conclusions: The rate of progress of coloration is more sensitive to temperature than its start date, resulting in an extension of the duration of leaf senescence under warming. The dependence of D_{LCO} response to temperature on daylength indicates stronger photoperiodic control on initiation of leaf senescence in areas with longer daylength (i.e., shorter nights), possibly because plants respond to the length of uninterrupted darkness rather than daylength. This study indicates that the onset of leaf coloration was not responsive to climate warming and provides observational evidence of photoperiod control of autumnal leaf senescence at biome and continental scales.

KEYWORDS

autumnal leaf senescence, global warming, leaf coloration onset, Northern Hemisphere, photoperiod

1 | INTRODUCTION

In contrast to the leaves of evergreen conifers, those of northern deciduous plants are not sufficiently tolerant of freezing to survive cold periods and, therefore, are shed before the onset of winter. This autumnal senescence process is controlled by changes in gene expression and metabolic adjustments that include the degradation of macromolecules (e.g., chlorophyll), a decrease in photosynthesis and, importantly, the recycling and re-allocation of nutrients (Gan & Amasino, 1997; Thomas & Stoddart, 1980). In parallel to leaf senescence, carbon sink activity ceases progressively, and plants switch to nutrient recovery and resorption processes (Estiarte & Peñuelas, 2015; Keskitalo et al., 2005). Without timely leaf senescence and abscission, early frost would reduce nutrient resorption, leading to a loss of leaf resources. Changes in the timing of key steps of leaf senescence extensively influence ecosystem structure and functions, such as vegetation activity, trophic interaction, carbon and nutrient cycling, land-atmosphere moisture and energy fluxes (Keenan et al., 2014; Morissette et al., 2009), which could further affect the climate system (Peñuelas et al., 2009; Richardson et al., 2013).

Senescence starts as a cryptic phenological process before any visible symptoms become apparent (Körner & Basler, 2010). The timing of the start of the leaf coloration following senescence varies, depending on the rate of the senescence process, which is

related to environmental conditions (e.g., temperature) (Fracheboud et al., 2009). Hence, the process of autumnal leaf senescence has two phases (Figure 1a): (1) a visually indistinguishable ontogenetic stage that precedes (2) a visible change in leaf colour (Tang et al., 2016). The timings of the middle and end of leaf coloration are the focus of *in situ* phenological observations and have been the main concern of most autumnal phenological studies to date.

Satellite and ground-based observations indicate that climate warming in the last several decades has substantially advanced the onset of spring green-up and the peak of the growing season, and it has slightly delayed the timing of the end of leaf coloration [D_{LCE} , the time when the normalized difference vegetation index (NDVI) decreases by 50% of its annual amplitude in the second half of a year in satellite-based studies (Ganguly et al., 2010; Lukasová et al., 2019; Melaas et al., 2013; Nagai et al., 2010; White et al., 1997; Yu et al., 2010)] in the Northern Hemisphere (Figure 1b) (Fu et al., 2015, 2019; Gill et al., 2015; Jeganathan et al., 2014; Menzel et al., 2020; Xu et al., 2016). In addition to temperature, an increase in precipitation also delays D_{LCE} in temperate dry grasslands in the northern middle latitudes (Liu et al., 2016). Besides these abiotic factors, temporal changes in D_{LCE} are also associated with the onset of green-up in some temperate tree species (Keenan & Richardson, 2015) and in boreal ecosystems (Liu et al., 2016). In contrast to D_{LCE} , the timing of onset of leaf coloration (D_{LCO} ; Figure 1b) has been studied inadequately. In

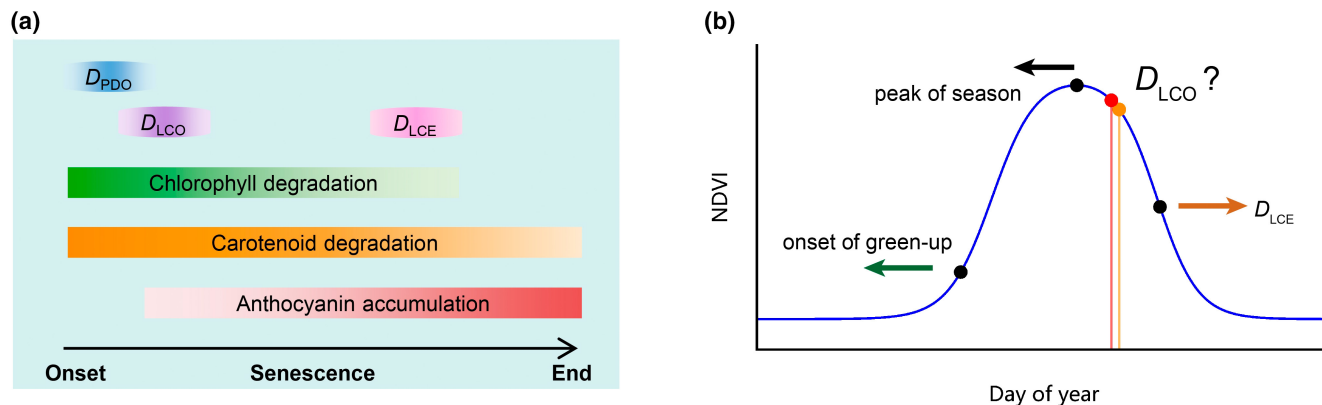


FIGURE 1 Conceptual graphs illustrating (a) the developmental processes in pigments during leaf senescence that are related to photosynthetic capacity and leaf colour; and (b) phenological changes retrieved from the normalized difference vegetation index (NDVI) in the last few decades. In (a), D_{PDO} and D_{LCO} are the timings of the onsets of the decrease in maximum canopy photosynthetic capacity and leaf coloration in autumn, respectively; D_{LCE} is the timing of the end of leaf coloration. In (b), the onset of green-up corresponds to a 20% increase in NDVI in spring, the peak of the season corresponds to the maximum NDVI, and D_{LCE} corresponds to a 50% decrease in NDVI in autumn. D_{LCO} was defined by two methods, corresponding to a 10% decrease in NDVI (orange point) and the inflection point at which NDVI begins to decline (red point), respectively (for details, see Section 2). The leftward and rightward arrows indicate advances of onset of green-up and peak of season and delay of D_{LCE} , respectively, over the past few decades. The question mark indicates a research gap regarding temporal changes in D_{LCO} and their drivers.

particular, it is not known whether D_{LCO} is sensitive to climate and whether it has been responsive to recent climate change. D_{LCO} is of key importance because it indicates when leaf senescence becomes detectable from NDVI and its progress accelerates (Figure 1b). As shown by experiments on young trees, some temperate and boreal woody species use the shortening of the photoperiod as a signal for the onset of leaf senescence (Supporting Information Table S1), but many *in situ* and satellite observations indicate that increased temperature induces delays in the advanced stages of senescence, such as D_{LCE} (Delpierre et al., 2009; Estrella & Menzel, 2006; Ge et al., 2015; Gill et al., 2015; Jeong et al., 2011; Liu et al., 2016).

A dominant photoperiodic control of early senescence implies that D_{LCO} should not be delayed, even if the temperature increases, because its timing is controlled only by daylength (hypothesis 1). Moreover, because D_{LCE} delays with warmer temperature, we may further hypothesize that earlier stages of leaf senescence are less sensitive to temperature than are more advanced stages and expect an extension of the period between D_{LCE} and D_{LCO} under warming. In contrast, without photoperiodic control, shifts in D_{LCO} are expected in the case of climatic warming (hypothesis 2). Alternatively, if D_{LCO} is influenced by both photoperiod and temperature, the relationships between D_{LCO} and temperature should vary among different areas, because the strength of the photoperiod signal varies (hypothesis 3).

To test these hypotheses, we initially investigated the temporal changes in D_{LCO} and the interannual relationships between D_{LCO} and pre- $D_{LCO} T_{min}$ (the mean of monthly average daily minimum temperature for an optimized period preceding D_{LCO}) for northern vegetation (30–75° N, with cropland pixels excluded) during the period 2000–2018. We then examined whether the timings of earlier stages of leaf coloration are less responsive to temperature and show fewer delays and assessed the impacts of temperature on the progress of leaf coloration. Given that only a few *in situ* observational programs

or networks have monitored D_{LCO} , we determined D_{LCO} from a 5-day composite time series of the NDVI derived from daily surface spectral reflectance (MOD09CMG) at a spatial resolution of .05°, provided by the spaceborne Moderate Resolution Imaging Spectroradiometer (MODIS) (Vermote, 2015). To complement the NDVI data, we also used 332 time series of D_{LCO} observed by professional observers according to standard observation guidelines (China Meteorological Administration, 1993) in the field in China (Supporting Information Figure S1a; Table S2) and the timing of onset of autumnal decline in maximum canopy photosynthetic capacity (D_{PDO}) derived from eddy covariance CO_2 flux observations (Gu et al., 2009; Shen, Tang, et al., 2014) at 36 sites from within the FLUXNET2015 dataset (Pastorello et al., 2017) (Supporting Information Figure S1b; Table S3).

2 | MATERIALS AND METHODS

2.1 | Estimating timings of stages of leaf coloration from satellite observations of NDVI time series

2.1.1 | Dataset and preprocessing

The NDVI is a proxy for vegetation greenness and has been widely used for phenological studies at large spatial scales (Buitenwerf et al., 2015; Gao et al., 2019; Keenan et al., 2014; Myneni et al., 1997; Wu et al., 2018). NDVI has also been proved capable of detecting the onset of leaf coloration (Mariën et al., 2019; Soudani et al., 2012, 2021; Yang et al., 2014; Zhao et al., 2020). Previous studies have usually used half-month/16-day composite NDVI time series to retrieve phenological metrics. However, because the duration of leaf coloration could be as short as 4 weeks in some areas (Ye & Zhang, 2021), NDVI time-series data with higher temporal resolution are required.

We estimated phenological metrics (i.e., the timings of the onset and the advanced stages of leaf coloration and the onset of green-up) for 2000–2018 from a 5-day composite NDVI time series produced from the MODIS reflectance product (MOD09CMG Collection 6, available at: <https://ladsweb.modaps.eosdis.nasa.gov>, accessed on 29 January 2019) (Vermote, 2015). MOD09CMG provides an estimate of daily surface spectral reflectance at a spatial resolution of .05°. The quality of the daily surface reflectance data from MOD09CMG is unsatisfactory owing to cloud and snow contamination (Vermote, 2015); therefore, we used the 5-day maximum value composite approach (Zhang, 2015), combined with a Savitzky–Golay filter (Cao et al., 2018), to produce a high-quality NDVI time series before determining D_{LCO} . Initially, NDVI values that were lower than the uncontaminated winter (December–February) mean NDVI were replaced by the latter (Beck et al., 2006; Zhang et al., 2007). After that, cloud-contaminated and irregularly high and low NDVI values were identified and reconstructed by using a Savitzky–Golay filter (Cao et al., 2018). Details for preparation of the high-quality NDVI time series are given in the Supporting Information (Section 1 of the Supplementary Methods).

We focused on natural vegetation by excluding pixels dominated by cropland, artificial surfaces, permanent snow or ice, and water bodies, on the basis of the MODIS land-cover map (MCD12C1 Version 6, available at: <https://ladsweb.modaps.eosdis.nasa.gov>, accessed on 20 August 2018) (Friedl & Sulla-Menashe, 2015) for the middle year of the time series (2009). Some pixels were also excluded from analysis because of sparse vegetation coverage, weak seasonality, or NDVI peaking in October–April. We adopted three criteria for pixel inclusion: mean annual NDVI must be $>.10$ (Jeong et al., 2011); NDVI should peak between May and September in the multiyear mean NDVI time series (Shen et al., 2020); and mean NDVI for July and August must be >1.15 times the mean NDVI for December and for January–February in every year (Shen, Zhang, et al., 2014).

2.1.2 | Estimation of timings of leaf coloration

Two methods can generally be used to estimate the parameters of vegetation phenology (Chen et al., 2016; Shang et al., 2017), including D_{LCO} from annual NDVI profiles. One is based on thresholds (White et al., 1997), whereas the other is based on inflection points (Zhang et al., 2003). We applied the threshold-based method by initially using a generalized sigmoid function to fit the NDVI annual profile [Equation (7) in the paper by Klosterman et al., 2014] and then determining D_{LCO} as the first date when NDVI decreased by 10% of its annual amplitude in the descending period (Leblans et al., 2017; Richardson et al., 2018). Although a smaller decrease in NDVI corresponds to an earlier stage of leaf coloration, consideration of it would introduce more uncertainty. We also determined D_{LCO} by using the algorithm based on inflection point. In this method, D_{LCO} was defined as the date when the rate of change of the curvature of a double logistic function (Beck et al., 2006; Elmore et al., 2012) fitted to the NDVI time series

reached its first local minimum in the descending period (Zhang et al., 2003). Theoretically, the D_{LCO} defined by the inflection method is close to the date when NDVI decreases by *c.* 9% of its annual magnitude (Shang et al., 2017).

The advanced stages of leaf coloration were determined as the dates when NDVI decreases by 20, 30, 40 and 50% (corresponding to the timing of the end of leaf coloration, D_{LCE}) of its annual amplitude, respectively. In addition, given that in a few studies (Berman et al., 2020; Ren et al., 2017) the end of leaf coloration was defined as the dates when NDVI drops by 60 or 90% of its annual amplitude, we also included these definitions in analysis. We defined the timing of the onset of green-up as the date when NDVI increased by 20% (Yu et al., 2010).

2.1.3 | Evaluation of satellite D_{LCO} using PhenoCam

It is unreasonable to validate the satellite-derived D_{LCO} by comparing it with the D_{LCO} of a few plant individuals from ground observation, because of mismatch in spatial coverage, different definitions of phenological metrics, and the spatial heterogeneity in phenological phases among individuals for a pixel. Fortunately, pairs of field observations of NDVI and leaf coloration showed good consistency between the start of NDVI decrease and the onset of leaf coloration (Soudani et al., 2012, 2021). Moreover, the comparison between the start of autumn from satellite-observed NDVI and field observations of leaf coloration onset for the entire area covered by the pixel also showed little difference between them (Zhao et al., 2020). Those studies suggest that NDVI is capable of detecting the onset of leaf coloration if the observed leaves or individuals are identical between ground and satellite observations. However, there are very limited pairs of compatible observations of NDVI and leaf coloration that can be used for validation.

Considering the high capability of PhenoCam in capturing the variations in leaf coloration onset at the landscape scale (Klosterman et al., 2014; Klosterman & Richardson, 2017; Nezval et al., 2020; Wingate et al., 2015), we used the PhenoCam dataset v.2.0 (Richardson et al., 2018; Seyednasrollah, Young, Hufkens, Milliman, Friedl, Frohling, & Richardson, 2019; Seyednasrollah, Young, Hufkens, Milliman, Friedl, Frohling, Richardson, Abraha, et al., 2019) to assess the relationships between satellite-derived D_{LCO} and the D_{LCO} derived from time series of the green chromatic coordinate (GCC) and vegetation contrast index (VCI) observed by PhenoCam. The GCC and VCI were determined from the digital numbers (DN) in red (R), green (G) and blue (B) channels. Specifically, GCC and VCI were calculated as $DN_G/(DN_R + DN_G + DN_B)$ and $DN_G/(DN_R + DN_B)$, respectively. Details for the determinations of D_{LCO} from time series of GCC and VCI are given in the Supporting Information (Section 2 of the Supplementary Methods).

2.2 | D_{LCO} from *in situ* phenological observations

D_{LCO} was extracted at the species level from datasets of *in situ* phenological observations in China provided by the Chinese Academy of

Sciences (CAS). The CAS dataset uses the date of first leaf colouring as D_{LCO} . For a given species at a given site, the date of first leaf colouring was identified as the day when the first batch (c. 5%) of leaves on more than half of three to five marked individuals started to change colour (China Meteorological Administration, 1993). The *in situ* phenological observations were performed visually according to standard observation guidelines (China Meteorological Administration, 1993) every other day by professional observers trained well by CAS. The CAS dataset is available from National Earth System Science Data Sharing Infrastructure, National Science and Technology Infrastructure of China (<http://www.geodata.cn>, accessed on 25 July 2018).

2.3 | D_{PDO} estimated from maximum canopy photosynthetic capacity

The timing of the onset of the decrease in maximum canopy photosynthetic capacity in autumn (as day of year, D_{PDO}) is defined as the date when the capacity decreases by 10% of its annual amplitude after the data have been fitted to a generalized sigmoid function [Equation (7) in the paper by Klosterman et al., 2014]. The capacity was calculated from half-hourly or hourly gross primary productivity (GPP_NT_CUT_MEAN) based on eddy covariance measurements in the FLUXNET2015 dataset (<http://fluxnet.fluxdata.org/data/fluxnet2015-dataset/>, accessed on 10 March 2018) (Pastorello et al., 2017). We followed the procedure of Shen, Tang et al. (2014) to estimate daily canopy photosynthetic capacity, except that the parameters in the rectangular hyperbolic function were estimated by using half-hourly/hourly gross primary productivity and incident short-wave radiation calculated by using 15-day moving windows throughout a year. We used data from the sites in non-Mediterranean (Köppen–Geiger climate classification) and non-cultivated (International Geosphere–Biosphere Programme classification) regions at middle and high northern latitudes (30–75° N). In a similar way to the pixel exclusion process that was applied to the satellite retrievals, we discarded sites where weak seasonality (i.e., the mean maximum canopy photosynthesis for June–August was <1.15 times that for December or for January and February) was detected in any year and sites where capacity did not peak in May–September.

2.4 | Analyses

2.4.1 | Temporal changes

Temporal changes of D_{LCO} over the study period were assessed using temporal trends in D_{LCO} , which were quantified as the slopes of linear regressions between D_{LCO} and year by using ordinary least squares regression (OLSR) and *t* tests. To complement the temporal changes assessed by using OLSR, a nonparametric approach (the Theil–Sen estimator and Mann–Kendall test; Sen, 1968; Theil, 1992) was also used to calculate the trends in D_{LCO} . Temporal changes of timings of advanced stages of leaf coloration were assessed in the same way.

The temporal trend was calculated for each time series for the ground-based observations and for each pixel for the satellite observations. We focused only on the temporal trends for the pixels and time series of *in situ* phenological observations with a multiyear mean of D_{LCO} occurring after the summer solstice. Phenological records were not available for some of the years of the time series for calculating more trends, because the time series might have had missing values owing to a lack of observation. However, the time series used for the regressions contained ≥ 10 years of observational records and at least one record for any 3 years consecutively. If two or more parts of the time series met these criteria, the most recent part was used.

2.4.2 | Partial correlation between D_{LCO} and temperature or precipitation

T_{min} has long been recognized as the indicator of the thermal condition that induces autumnal leaf coloration (Tang et al., 2016), and the duration of the period preceding D_{LCO} in which T_{min} has the largest influence on D_{LCO} could vary among different locations because of differential vegetation characteristics and climate conditions (Gao et al., 2019; Jeong et al., 2011; Matsumoto et al., 2003; Wu et al., 2018). In addition, precipitation might also regulate leaf coloration in dry climates (Liu et al., 2016). Initially, we determined the duration of this period preceding D_{LCO} (referred to as the pre- D_{LCO} period). Taking satellite-derived D_{LCO} , for example, we investigated the impacts of temperature on the D_{LCO} by calculating the partial correlation coefficient (R_{TN}) values between D_{LCO} and the mean of the monthly average daily minimum temperature (T_{min}) for the pre- D_{LCO} period, with concurrent total precipitation as the control variable for 2000–2018. The pre- D_{LCO} period for T_{min} (Supporting Information Figure S2) was defined as the period preceding the multiyear mean D_{LCO} for which T_{min} had the strongest interannual partial correlation with D_{LCO} , with concurrent total precipitation as a control variable (Jeong et al., 2011; Wu et al., 2018). In detail, we first determined several candidate periods that ended at the multiyear mean D_{LCO} and had a duration starting from 1 month, with a step of 1 month. For each of the candidate periods, we calculated the partial correlation coefficient between D_{LCO} and mean T_{min} in each of these periods, then selected the candidate with the highest absolute value of correlation coefficient. If the multiyear mean D_{LCO} was in the first half of a month, then the pre- D_{LCO} period ended at the month preceding the multiyear mean D_{LCO} . Otherwise, the pre- D_{LCO} period ended at the month of the multiyear mean D_{LCO} . The impacts of T_{min} on the advanced stages of leaf coloration were investigated in a similar manner. A few studies have suggested that the date of onset of green-up might affect leaf coloration through carry-over effects (Cong et al., 2017; Fu et al., 2014; Keenan & Richardson, 2015; Liu et al., 2016); therefore, we also considered the case in which the onset of green-up was included as an extra control variable in the partial correlation between D_{LCO} and T_{min} . The pre- D_{LCO} period for precipitation and the impacts of precipitation on D_{LCO} were assessed in a similar manner.

The data for T_{\min} and precipitation were extracted from the Climatic Research Unit (CRU) Time-Series (TS) 4.03 dataset (<http://data.ceda.ac.uk>, accessed on 11 June 2019), which provided monthly data at a spatial resolution of $.5^{\circ} \times .5^{\circ}$ until 2018. It should be noted that T_{\min} in the dataset is an approximation of the mean of daily minimum temperature for a calendar month, which is calculated arithmetically from the gridded monthly mean temperature and the diurnal temperature range (Harris et al., 2014) and does not exactly reflect the interannual variations in the absolute minimum temperature (Körner & Hiltbrunner, 2018) experienced by plants before D_{LCO} . The CRU data were resampled at $.05^{\circ} \times .05^{\circ}$ by replication to match the D_{LCO} data.

Complementary to the pre- D_{LCO} period in which T_{\min} had the strongest interannual partial correlation with D_{LCO} , we also used fixed durations (1 month and 15 days preceding multiyear mean D_{LCO} , respectively) as the pre- D_{LCO} periods. We calculated the partial correlation between D_{LCO} and pre- D_{LCO} T_{\min} , with concurrent total precipitation as the control variable. Moreover, we investigated the partial correlation coefficient between D_{LCO} and the lowest T_{\min} during the 15 days before the multiyear mean D_{LCO} , with the concurrent mean T_{\min} (mean of the remaining 14 T_{\min} values after removal of the lowest T_{\min} during the period) and total precipitation as control variables. Note that when the pre- D_{LCO} period was defined as the 15 days preceding D_{LCO} and when we analysed the relationship between the lowest T_{\min} and D_{LCO} , daily T_{\min} and precipitation were extracted from the CRU-NCEP dataset (v.7.2, available at: <https://vesg.ipsl.upmc.fr>, assessed on 10 January 2019), which provides 6-hourly data at a spatial resolution of $.5^{\circ} \times .5^{\circ}$ until 2016 (Viovy, 2018). The CRU-NCEP v.7.2 is a combination of two datasets: the CRU TS3.2 $.5^{\circ} \times .5^{\circ}$ monthly data covering the period 1901–2002 and the NCEP re-analysis $2.5^{\circ} \times 2.5^{\circ}$ 6-hourly data covering the period 1948–2016. We determined daily T_{\min} as the minimum value of the four 6-hourly minimum temperature values for each day. The CRU-NCEP data were resampled at $.05^{\circ} \times .05^{\circ}$ by replication to match the D_{LCO} data.

We also investigated the impact of T_{\min} and precipitation on D_{LCO} from ground-based observations in China and on D_{PDO} from eddy-covariance sites as complementary to satellite-derived D_{LCO} . Climatic data for *in situ* observations in China were extracted from the “Daily Surface Climate Variables of China” catalogue (a dataset named SURF_CLI_CHN_MUL_DAY_V3.0), which includes daily climate data for 2,474 sites in China from January 1951 to July 2014, provided by the Chinese Meteorological Administration. The distance between phenological and meteorological stations was <25 km. Climatic data for D_{PDO} were calculated from the half-hourly temperature dataset provided by FLUXNET2015.

2.4.3 | Relationships between the progress of leaf coloration and temperature

The impacts of temperature on the progress of leaf coloration were assessed in four ways.

First, we calculated the partial correlation coefficient between each of the timings of different stages in leaf coloration (determined

as NDVI decreases by 20, 30, 40, 50, 60 and 90%) and preceding T_{\min} using the approach described in Section 2.4.2. We then compared the percentage of area corresponding to the partial correlation coefficient among the different timings.

Second, the difference in temperature sensitivity between the D_{LCE} and D_{LCO} was used to assess the differential responses to T_{\min} between D_{LCE} and D_{LCO} . The temperature sensitivity of D_{LCO} was defined as the coefficient for pre- D_{LCO} T_{\min} in a linear regression in which D_{LCO} was set as the dependent variable, and pre- D_{LCO} T_{\min} and pre- D_{LCO} total precipitation were independent variables. The temperature sensitivity of D_{LCE} was calculated in a similar manner. See Section 2.4.2 for the details of the determination of pre- D_{LCO} (or pre- D_{LCE}) T_{\min} and total precipitation.

Third, the temperature sensitivity of the duration of leaf coloration was used to assess the impact of temperature on the duration of leaf coloration. The duration of leaf coloration was defined as the difference between D_{LCE} and D_{LCO} . Its temperature sensitivity was estimated as the coefficient for mean T_{\min} in the linear regression in which the duration was set as the dependent variable and the mean T_{\min} and total precipitation in the period between D_{LCE} and D_{LCO} were independent variables.

Fourth, the temperature sensitivity of the speed of leaf coloration was used to assess the impact of temperature on the speed of leaf coloration within a season. The speed of leaf coloration within a season was defined as the normalized decreasing speed of NDVI between D_{LCE} and D_{LCO} , calculated as $-(\text{NDVI}_{\text{DLCE}} - \text{NDVI}_{\text{DLCO}}) / (D_{\text{LCE}} - D_{\text{LCO}}) / \text{AMP}_{\text{NDVI}}$, where AMP_{NDVI} is the annual amplitude of NDVI for a given pixel and given year. The temperature sensitivity of the speed of leaf coloration was then calculated as the coefficient for mean T_{\min} when regressing the speed of leaf coloration against mean T_{\min} and total precipitation between D_{LCE} and D_{LCO} . Here, T_{\min} and precipitation were extracted from the CRU TS 4.03 monthly data.

2.4.4 | Dependence of D_{LCO} on daylength

Previous experimental findings suggest that daylength is a signal for the start of autumn leaf senescence (Supporting Information Table S1), indicating a photoperiodic control of D_{LCO} . However, it is difficult to assess the role of daylength by using interannual correlations between D_{LCO} and daylength in natural conditions, because the daylength on a given date does not vary among years. Alternatively, because control of photoperiod on autumn leaf phenology might vary with daylength across different regions (Howe et al., 1995; Pau et al., 2011; Paus et al., 1986; Saikkonen et al., 2012), we examined the variabilities in the correlation between D_{LCO} and T_{\min} and in temporal changes in D_{LCO} against the spatial gradient of daylength to explore the dependence of D_{LCO} on daylength. Meanwhile, the spatial variations in the response of autumn leaf phenology to temperature might be associated with local background temperature conditions (Ford et al., 2017; Zohner et al., 2016). Hence, the spatial variations in background

temperature should be minimized when assessing the dependence of D_{LCO} on daylength. To do this, we first calculated the daylength for each pixel at the date of multiyear mean D_{LCO} over the period 2000–2018 and the mean T_{min} of the period before multiyear mean D_{LCO} . The period before multiyear mean D_{LCO} was the month preceding the multiyear mean D_{LCO} if the multiyear mean D_{LCO} was in the first half of a month; otherwise, the period was the month of the multiyear mean D_{LCO} . Next, for each cell of 1.5-h daylength and 4 °C mean T_{min} in the space of the daylength and mean T_{min} (for a graphical illustration, see Figure 5), we calculated the percentage of area with significant ($p < .05$, t test) D_{LCO} delays, the average of positive correlation, and the percentage of area with a positive correlation between D_{LCO} and T_{min} (or precipitation).

In addition, there is more experimental evidence of photoperiodic control on the onset of leaf senescence for woody plants than for herbaceous plants (Supporting Information Table S1), indicating that woody and herbaceous vegetation might respond to photoperiod in different ways. Therefore, the above exploration was also performed separately for woody and herbaceous vegetation. The woody and herbaceous vegetation were merged from Classes 1–6 and Class 10, respectively, in the MODIS land-cover product (MCD12C1, v.6) for 2009 (Friedl & Sulla-Menashe, 2015).

2.4.5 | Possible effect of summer NDVI

In some deciduous forests, NDVI can decline in early summer (i.e., late May–July) before leaf coloration, and this might potentially interfere to some extent with the determination of D_{LCO} (Elmore et al., 2012) and its relationship with temperature. To address this, for the pixels classified as deciduous broadleaf forest in the MODIS land-cover product (Friedl & Sulla-Menashe, 2015), we redefined D_{LCO} considering the possible effect of summer NDVI decline on D_{LCO} and then re-analysed the trends in D_{LCO} and the relationship between D_{LCO} and temperature as described in Sections 2.4.1 and 2.4.2.

For the sake of robustness, the possible effect of summer NDVI decline on D_{LCO} was considered in three different ways. First, we used a modified double logistic model that considers early summer NDVI decline (Elmore et al., 2012) to fit the NDVI time series instead of the original double logistic function for the pixels classified as deciduous broadleaf forest. D_{LCO} was then determined as the date when the rate of change of the curvature of a double logistic function fitted to the NDVI time series reached its first local minimum in the descending period. Second, D_{LCO} was defined as the date when NDVI decreased by 10% of its annual amplitude from 1 August. The maximum value used to determine the annual amplitude was the mean value of the upper quartile of the fitted NDVI values in August. Third, D_{LCO} was defined as the date when NDVI decreased by 10% of its annual amplitude from 16 August. The maximum value used to determine the annual amplitude was the mean value of the upper quartile of the fitted NDVI values in the second half of August.

2.4.6 | Possible cold events before D_{LCO} (or D_{PDO})

A sudden drop of night-time temperature to the freezing point can induce leaf coloration in a few days (Körner, 2007), and this might interfere with our partial correlation analysis between D_{LCO} (or D_{PDO}) and temperature. Hence, we re-examined the temporal changes in D_{LCO} and the correlation between D_{LCO} and temperature as described in Sections 2.4.1 and 2.4.2, after excluding possible cold events estimated using an empirical approach as follows (taking satellite-derived D_{LCO} as an example).

First, we determined the T_{min} threshold below which there could potentially be a cold event for each pixel. Given that a cold event that induces rapid leaf senescence should happen 1–5 days before D_{LCO} , the lowest T_{min} during the 6–35 days before D_{LCO} for all years was set as the T_{min} threshold. A temperature higher than such a threshold will not induce a cold event. For vegetation in middle and high latitudes, a temperature higher than freezing (0°C) does not cause frost damage (Körner, 2021; Lenz et al., 2013; Sakai & Larcher, 1987; Taschler & Neuner, 2004). Therefore, if the lowest T_{min} was $>0^{\circ}\text{C}$, the T_{min} threshold was set to 0°C.

Second, for a given pixel, a year was determined as a candidate cold event year if the lowest T_{min} in the period 1–5 days before D_{LCO} was lower than the above-mentioned T_{min} threshold. Then, from the years in which there was no candidate cold event, we determined the latest D_{LCO} that was not caused by a cold event for that pixel.

Finally, a D_{LCO} was recognized as possibly being caused by a cold event if it was in the candidate cold event years and also earlier than the latest D_{LCO} that was not caused by a cold event. For a D_{LCO} (referred to as D'_{LCO}) from the candidate cold event years and later than the latest D_{LCO} that was not caused by a cold event, it (D'_{LCO}) would be recognized as a D_{LCO} possibly caused by a cold event if one of the following two conditions was met: (1) the decreasing rate of T_{min} in the period 1–5 days before D'_{LCO} was faster than the maximum decreasing rate of T_{min} among the years in which there was no candidate cold event; or (2) the decrease (absolute value) in T_{min} in the period 1–5 days before D'_{LCO} was greater than the maximum decrease in T_{min} among the years with no candidate cold event. Here, for a given year, the decreasing rate of T_{min} in the period 1–5 days before D_{LCO} (or D'_{LCO}) was calculated as the minimum of the slopes of T_{min} against calendar date. A slope of T_{min} against calendar date was calculated as $[T_{\text{min}}(\text{time}2) - T_{\text{min}}(\text{time}1)] / (\text{time}2 - \text{time}1)$, where $\text{time}2 = D_{\text{LCO}} - 1, D_{\text{LCO}} - 2, D_{\text{LCO}} - 3, D_{\text{LCO}} - 4$ or $D_{\text{LCO}} - 5$ and $\text{time}1 = D_{\text{LCO}} - 2, D_{\text{LCO}} - 3, D_{\text{LCO}} - 4$ or $D_{\text{LCO}} - 5$, and $\text{time}2$ is later than $\text{time}1$. The decrease in T_{min} in the period 1–5 days before D_{LCO} (or D'_{LCO}) for a given year was the maximum value of magnitudes of $[T_{\text{min}}(\text{time}2) - T_{\text{min}}(\text{time}1)]$.

This empirical approach might have overestimated the number of years with cold events before D_{LCO} (hereafter, these identified events are referred to as possible cold events), but our objective here was to exclude as many cold events as possible, then to examine whether the main findings of our study were caused by cold events. In addition, under clear skies, the temperature of the canopy surface could be lower than the air temperature; therefore, we also

determined the possible cold events by using 2°C as the T_{min} threshold (Körner, 2021).

Here, the daily T_{min} used to determine possible cold events for satellite-derived D_{LCO} was extracted from the CRU-NCEP v.7.2 dataset. Daily T_{min} for ground-based observations in China was derived from the nearest meteorological station (<25 km), provided by the Chinese Meteorological Administration. Daily T_{min} for D_{PDO} was calculated from the half-hourly temperature dataset provided by FLUXNET2015.

3 | RESULTS

3.1 | Comparison of satellite D_{LCO} with PhenoCam D_{LCO}

The satellite D_{LCO} explained >80% of the variations in PhenoCam-derived D_{LCO} ($n = 378$ and 377 for GCC and VCI, respectively; Figure 2). The differences between the satellite-derived D_{LCO} and the PhenoCam-derived D_{LCO} are caused by the mismatch between the annual NDVI and GCC (or VCI) trajectories owing to the difference in spatial coverage between the PhenoCam and satellite pixels in the case of phenologically heterogeneous land surface (see Supporting Information Supplementary Methods Section 2).

3.2 | Proportion of possible cold events before D_{LCO} (or D_{PDO})

Possible cold events occurred before D_{LCO} or D_{PDO} in very small fractions of pixel-years/site-years with phenological data (1.6, 1.7 and .6% for satellite-derived D_{LCO} , ground-based observations in China, and D_{PDO} from eddy-covariance sites, respectively; Table 1). The proportion of years possibly affected by cold events was slightly higher when using the method based on a temperature threshold of 2°C than that of 0°C.

3.3 | Temporal trends in D_{LCO} and the advanced stages of leaf coloration

D_{LCO} was not significantly delayed in 94% of the area during the study period, as assessed by OLSR. The few pixels with a significant delay trend (6%; $p < .05$, t test) were scattered across the Northern Hemisphere (Figure 3a). Excluding years with possible cold events before D_{LCO} produced similar results (Supporting Information Figure S3; Table S4). The Theil–Sen estimator generated results supporting the lack of changes in D_{LCO} (no significant delay in 96% of the area; $p < .05$, Mann–Kendall test; Supporting Information Figure S4a; Table S5). When we defined D_{LCO} as the inflection point at which NDVI begins to decline, we obtained similar results (Supporting Information Figure S4b,c). Considering early summer NDVI decline produced similar results (Supporting Information Figures S5–S7).

Complementary to satellite-derived D_{LCO} , we also examined the temporal changes of D_{LCO} by using ground-based leaf coloration data from China. D_{LCO} was not significantly delayed for 90 and 94% of the 332 time series as shown by OLSR (Figure 3b) and the Theil–Sen method (Supporting Information Table S5), respectively. Similar results were produced when possible cold events were excluded (Supporting Information Table S4).

The timings of earlier stages of leaf coloration exhibited delaying trends in fewer areas. The leaf coloration stages determined as the dates when NDVI decreases by 50% (i.e., D_{LCE}), 40, 30, 20 and 10% (i.e., D_{LCO}) were significantly ($p < .05$, t test) delayed for 14, 14, 12, 9 and 6% of the area, respectively (Supporting Information Figure S8).

3.4 | Correlation between D_{LCO} and temperature or precipitation

D_{LCO} was not consistently correlated with pre- D_{LCO} T_{min} , with only 9% of the area in scattered pixels showing a significant positive correlation and 5% showing a significant negative correlation (Figure 4a). D_{LCO} was positively correlated with pre- D_{LCO} total precipitation in

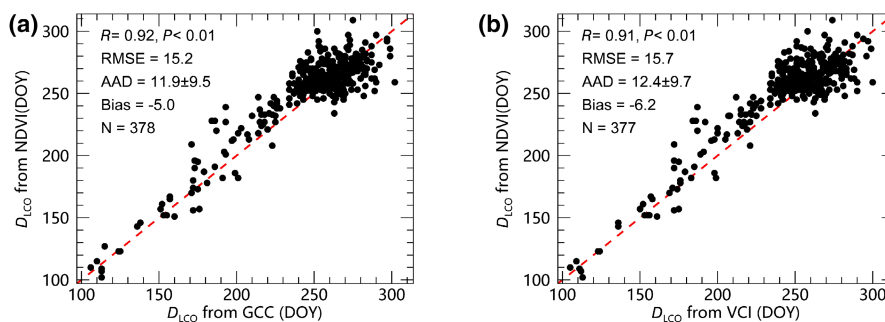


FIGURE 2 Comparison between satellite timing of the onset of leaf coloration in autumn (D_{LCO}) and PhenoCam-derived D_{LCO} . The PhenoCam-derived D_{LCO} was determined from the green chromatic coordinate (GCC; a) and vegetation contrast index (VCI; b), respectively. AAD = average absolute difference; bias is defined as the difference between the mean of satellite-derived D_{LCO} and the mean of PhenoCam-derived D_{LCO} , and negative bias means that the PhenoCam-derived D_{LCO} is earlier than satellite-derived D_{LCO} ; R = Pearson's correlation coefficient; RMSE = root mean square error.

TABLE 1 Proportions of years with possible cold events before D_{LCO} (for satellite and *in situ* observations) and before D_{PDO} (for FLUXNET2015)

Metrics	Satellite D_{LCO} (2000–2016)	<i>In situ</i> D_{LCO} China	FLUXNET2015 D_{PDO}
Proportion (%) of years with possible cold events (0°C)	1.6	1.7	.6
Proportion (%) of years with possible cold events (2°C)	2.1	3.5	1.0

Note: Possible cold events were determined mainly by using a threshold-based method with a daily minimum temperature of 0 or 2°C (for identification of possible cold events, see Section 2.4.5).

Abbreviations: D_{LCO} , timing of onset of leaf coloration in autumn; D_{PDO} , timing of onset of the decrease in maximum canopy photosynthetic capacity in autumn.

13% of the area, mainly in the temperate grassland of North America and in the middle latitudes of Eurasia, sub-arctic grassland, and alpine steppe of the Tibetan Plateau (Supporting Information Figure S9). Therefore, neither pre- $D_{LCO} T_{min}$ nor precipitation was a useful predictor of D_{LCO} in most areas. We obtained similar results when using the month preceding D_{LCO} (Supporting Information Figure S10) or 15 days preceding D_{LCO} (Supporting Information Figure S11) as the pre- D_{LCO} period, with only 6 and 5%, respectively, of the area showing a significant positive correlation between D_{LCO} and pre- $D_{LCO} T_{min}$. We also investigated the relationship between D_{LCO} and the lowest daily minimum temperature during the 15 days before the multiyear mean D_{LCO} , and only 3% of the area showed a significant positive correlation (Supporting Information Figure S12). Moreover, including the date of onset of green-up as an extra control variable in the partial correlation analyses did not affect the results (Supporting Information Figure S13). The *in situ* phenological records in China indicated that ground-observed D_{LCO} was positively correlated with pre- $D_{LCO} T_{min}$ for 13% of the time series and was not correlated with pre- $D_{LCO} T_{min}$ for 82% of the time series (Table 2). Excluding D_{LCO} possibly caused by cold events produced similar results (Supporting Information Figure S14; Table S6). Overall, these results suggest that an increase in pre- $D_{LCO} T_{min}$ is not likely to delay D_{LCO} in most areas in the middle and high northern latitudes.

3.5 | Impacts of temperature on the progress of leaf coloration

We first examined whether the timings of earlier stages of leaf coloration are less closely related to temperature than later stages. The fact that the earlier stages of leaf coloration had fewer areas with a significantly delayed trend (Supporting Information Figure S8) is in agreement with the finding that the significantly positive correlations between the timings of earlier stages of leaf coloration and T_{min} were observed in fewer areas (Figure 4c). The timings of leaf coloration stage corresponding to NDVI decreases by 40, 30, 20 and

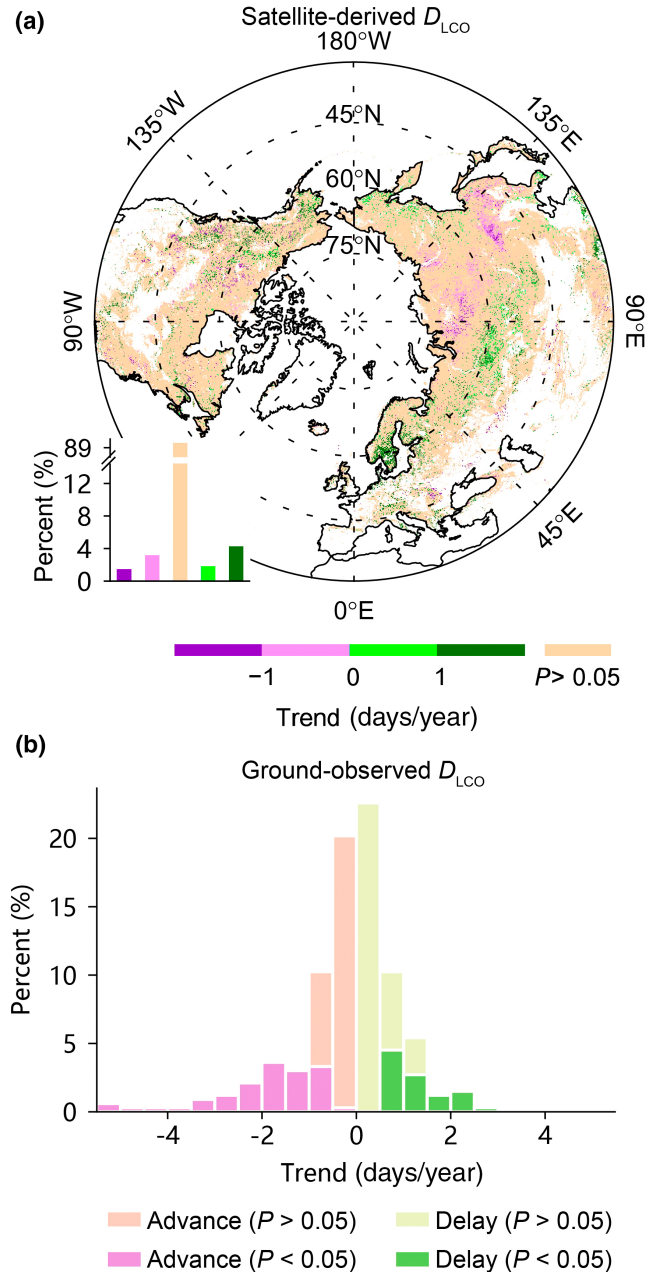


FIGURE 3 Temporal trends in the timing of the onset of leaf coloration (D_{LCO}), as retrieved from satellite and *in situ* observations. (a) Satellite-derived D_{LCO} trends over 2000–2018. The bar chart in the bottom-left corner shows the percentage of area within each interval of the significant temporal trends and the percentage of area with non-significant trends, indicated by the colour scale at the bottom. Positive and negative trend values refer to significantly delayed and advanced D_{LCO} , respectively. D_{LCO} corresponds to a 10% decrease in normalized difference vegetation index. (b) Ground-observed D_{LCO} trends derived over 1971–1997 from observations of *in situ* leaf coloration in China. Significant temporal trends were determined using *t* tests at $p < .05$ and ordinary least squares regression.

10% (i.e., D_{LCO}) exhibited a significant positive correlation with T_{min} in 30, 25, 17 and 9% of the area, respectively (Figure 4a,c; Supporting Information Figure S15). In particular, D_{LCE} exhibited a significant

positive correlation with pre- $D_{LCE} T_{min}$ in 34% of the area (Figure 4b), substantially more than that for the $D_{LCO}-T_{min}$ correlations (9%; Figure 4a). The proportion increased to 38 and 41% for the timings of leaf coloration stage corresponding to a 60 and 90% decrease in NDVI, respectively (Supporting Information Figure S16).

These results show decreasing correlations with temperature of earlier stages of leaf senescence. To verify this, we examined the correlation between D_{PDO} , an indicator of leaf senescence earlier than D_{LCO} , and pre- $D_{PDO} T_{min}$. D_{PDO} and pre- $D_{PDO} T_{min}$ exhibited a less positive correlation than NDVI-derived D_{LCO} and pre- $D_{LCO} T_{min}$ at the same sites during the same periods (3 and 6% of the sites for D_{PDO} and D_{LCO} , respectively; Supporting Information Table S7). Among all the eddy-covariance towers, D_{LCO} exhibited a significant positive correlation with pre- $D_{LCO} T_{min}$ in 3% of the 36 and was not correlated with pre- $D_{PDO} T_{min}$ in 89% of the eddy-covariance records (Table 2). Moreover, excluding D_{PDO} possibly caused by cold events produced similar results (Supporting Information Table S6).

We then examined whether D_{LCO} is less sensitive to temperature than D_{LCE} . In most regions (66%) of the middle and high northern latitudes, the temperature sensitivity of D_{LCO} was less than that of D_{LCE} (Figure 4d). The temperature sensitivity of D_{LCO} was less than D_{LCE} by ≥ 4 days/°C in 39% of the study area, mainly in northern Europe, the eastern USA, eastern Canada and western Russia. In 14% of the area, the temperature sensitivity of D_{LCO} was > 4 days/°C greater than D_{LCE} , mainly distributed in the Tibetan Plateau, western North America, areas in Europe near 60° N, northern Kazakhstan, and between 45 and 65° N in Russia.

As can be expected from the lower temperature sensitivity of D_{LCO} relative to that of D_{LCE} , warming could extend the duration of leaf coloration in 71% of the area (Figure 4e). In 42% of the area, the temperature sensitivity of the duration of leaf coloration was > 3 days/°C, mainly in Russia, eastern North America and northern Europe. The area with a temperature sensitivity < -3 days/°C accounted for 11% of the study area, scattered in the Tibetan Plateau, central USA, western North America, between 45 and 60° N in Europe, northern Kazakhstan and south-eastern Russia.

Moreover, warming could slow the progress of leaf coloration. In 69% of the area, the speed of leaf coloration could be reduced by higher temperature (Figure 4f), particularly in the region north of

60° N. The temperature sensitivity of the speed of leaf coloration was $< -1\%$ /day/°C in 34% of the study area (negative values of temperature sensitivity indicate that warming reduces the speed of leaf coloration), mainly in eastern and northern Canada, northern Europe and northern Russia. Only 13% of the area showed a large increase in the speed of leaf coloration under increasing temperature ($> 1\%$ /day/°C), scattered in Mongolia, the Tibetan Plateau, western Canada, central and western USA, and central and south-eastern Russia.

When considering early summer NDVI decline, we also found that more advanced stages of leaf coloration were more responsive to temperature (Supporting Information Figures S17c,d and S18c,d), and that warming could slow the progress of coloration (Supporting Information Figures S17f and S18f) and extend the duration of leaf coloration (Supporting Information Figures S17e and S18e).

3.6 | Dependence of D_{LCO} on daylength

We attempted to explore the dependence of D_{LCO} on daylength by examining the variabilities in the correlation between D_{LCO} and T_{min} and in temporal changes in D_{LCO} against the spatial gradient of daylength. In the areas with longer daylengths at multiyear mean D_{LCO} , there were proportionally fewer significant D_{LCO} delays during 2000–2018 (Figure 5a; Supporting Information Figure S19a), and the positive relationship between D_{LCO} and pre- $D_{LCO} T_{min}$ was slightly weaker, as indicated by the lower partial correlation coefficient between them (Figure 5d). Such patterns were more prominent for woody vegetation than for herbaceous vegetation (Figure 5b,c,e,f; Supporting Information Figure S19b,c). For vegetation with a daylength at D_{LCO} of > 13.5 h, D_{LCO} was more positively correlated with pre- $D_{LCO} T_{min}$ in colder areas at a given daylength (Figure 5d–f). The dependences of D_{LCO} trends on daylength and of the correlation between D_{LCO} and pre- $D_{LCO} T_{min}$ on daylength were also found when years with possible cold events before D_{LCO} were excluded (Supporting Information Figure S20) and when we considered summer decline in NDVI (Supporting Information Figures S21 and S22). The correlation between D_{LCO} and pre- D_{LCO} total precipitation was independent of daylength and was slightly stronger for the areas with a higher temperature before D_{LCO} , mostly because of the

FIGURE 4 Impacts of temperature on the timing of different stages of leaf coloration and on the progress of leaf coloration over the period 2000–2018. (a) Spatial pattern of the partial correlation coefficient (R_{TN}) between the onset of leaf coloration [D_{LCO} , 10% decrease in normalized difference vegetation index (NDVI)] and pre- D_{LCO} mean daily minimum temperature (T_{min}). (b) Spatial pattern of R_{TN} between timing of the end of leaf coloration (D_{LCE} , 50% decrease in NDVI) and pre- $D_{LCE} T_{min}$. The bar charts inset in (a) and (b) show the percentage of area for each interval of the partial correlation coefficient ($p < .05$), with the coefficient indicated by the colour scale on the right. Non-significant correlations ($p > .05$) are in grey. (c) Percentage of area for which R_{TN} between the timing of a given stage of leaf coloration and preceding T_{min} is higher than a given threshold indicated by the horizontal axis. For example, R_{TN} for the onset of leaf coloration is $> .2$ in c. 40% of the area. (d) Difference in temperature sensitivity between D_{LCE} and D_{LCO} . Positive values indicate that D_{LCE} is more sensitive to temperature than D_{LCO} , whereas negative values indicate that D_{LCO} is more sensitive to temperature than D_{LCE} . (e) Temperature sensitivity of the duration of leaf coloration. Positive values indicate that warming extends the duration of leaf coloration, whereas negative values indicate that warming shortens the leaf coloration duration. (f) Temperature sensitivity of the speed of leaf coloration. Positive values indicate that warming increases the speed of leaf coloration, whereas negative values indicate that warming reduces the speed of leaf coloration. The bar charts inset in (d–f) show the percentage of area for each interval of the temperature sensitivity indicated by the colour scale on the right.

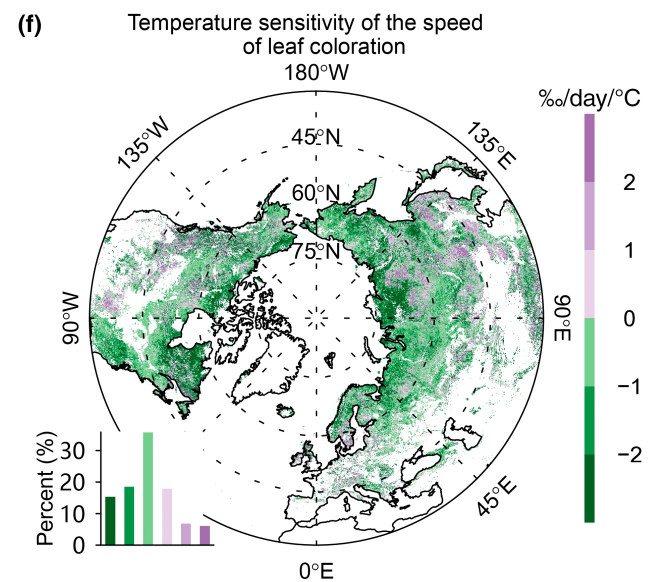
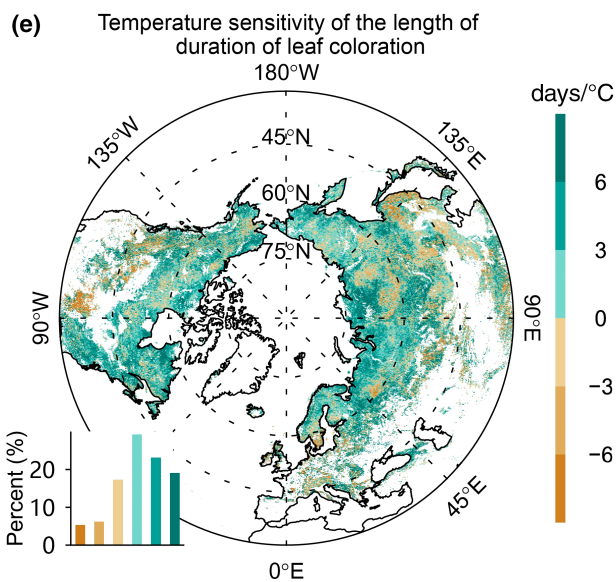
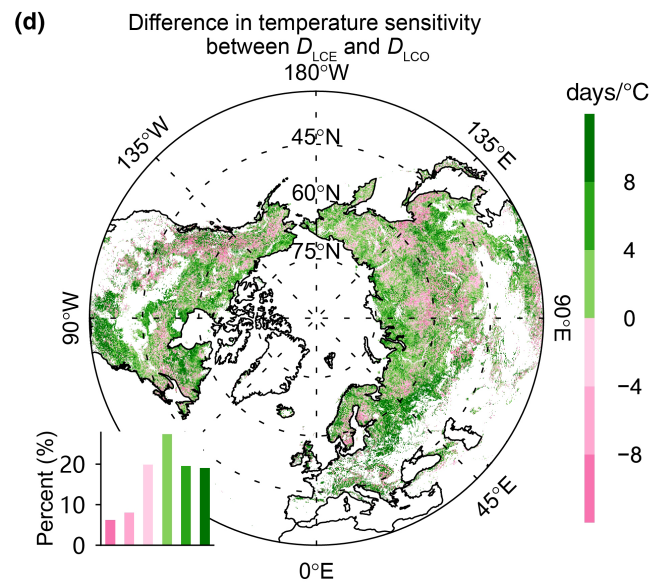
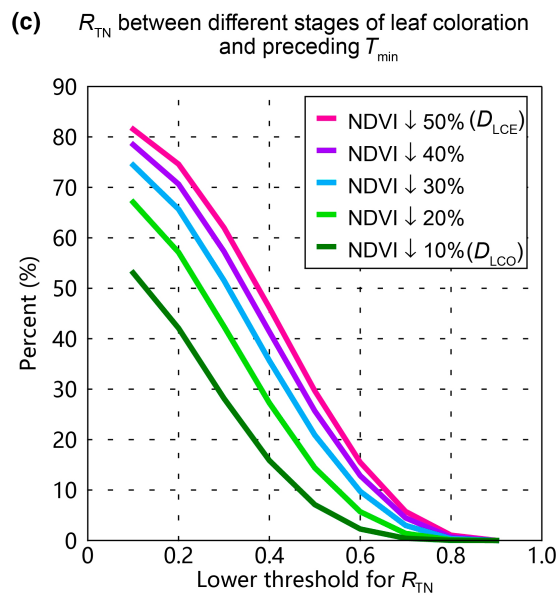
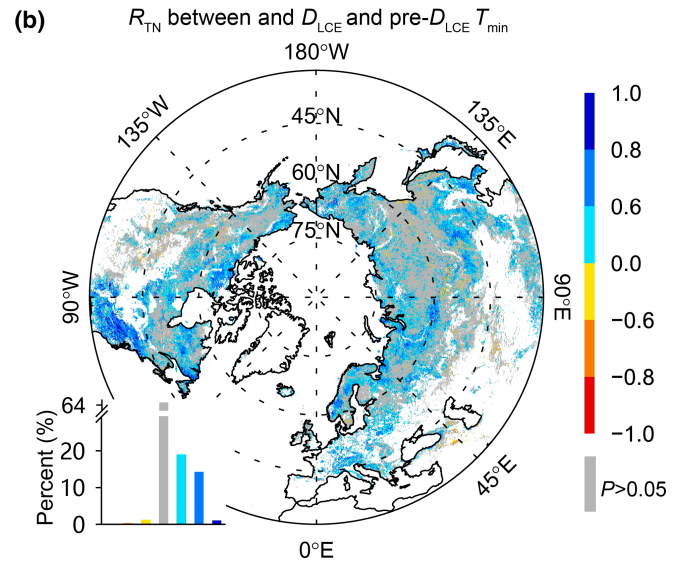
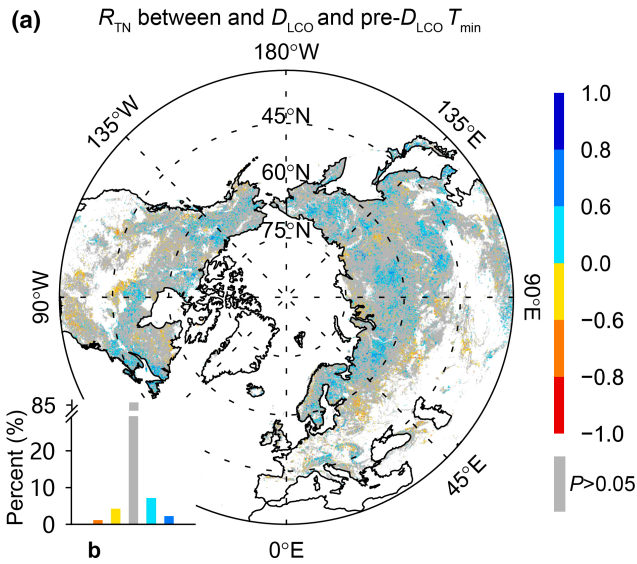


TABLE 2 Percentage of correlations between D_{LCO} or D_{PDO} and each climate factor for each interval of the partial correlation coefficient

Metric	Number of time series	Climate factor	Interval of the partial correlation coefficient ($p < .05$)						$p > .05$
			(-1.0, -.8)	(-.8, -.6)	(-.6, 0)	(0, .6)	(.6, .8)	(.8, 1.0)	
<i>In situ</i> D_{LCO} China	332	Temperature	0	2	3	4	8	1	82
		Precipitation	0	3	3	4	5	0	85
FLUXNET2015 D_{PDO}	36	Temperature	0	5	3	0	3	0	89
		Precipitation	0	6	0	8	3	5	78

Note: The data in the rightmost column indicate the percentages of area or time series with non-significant correlations.

Abbreviations: D_{LCO} , timing of the onset of leaf coloration in autumn; D_{PDO} , timing of the onset of the decrease in maximum canopy photosynthetic capacity in autumn.

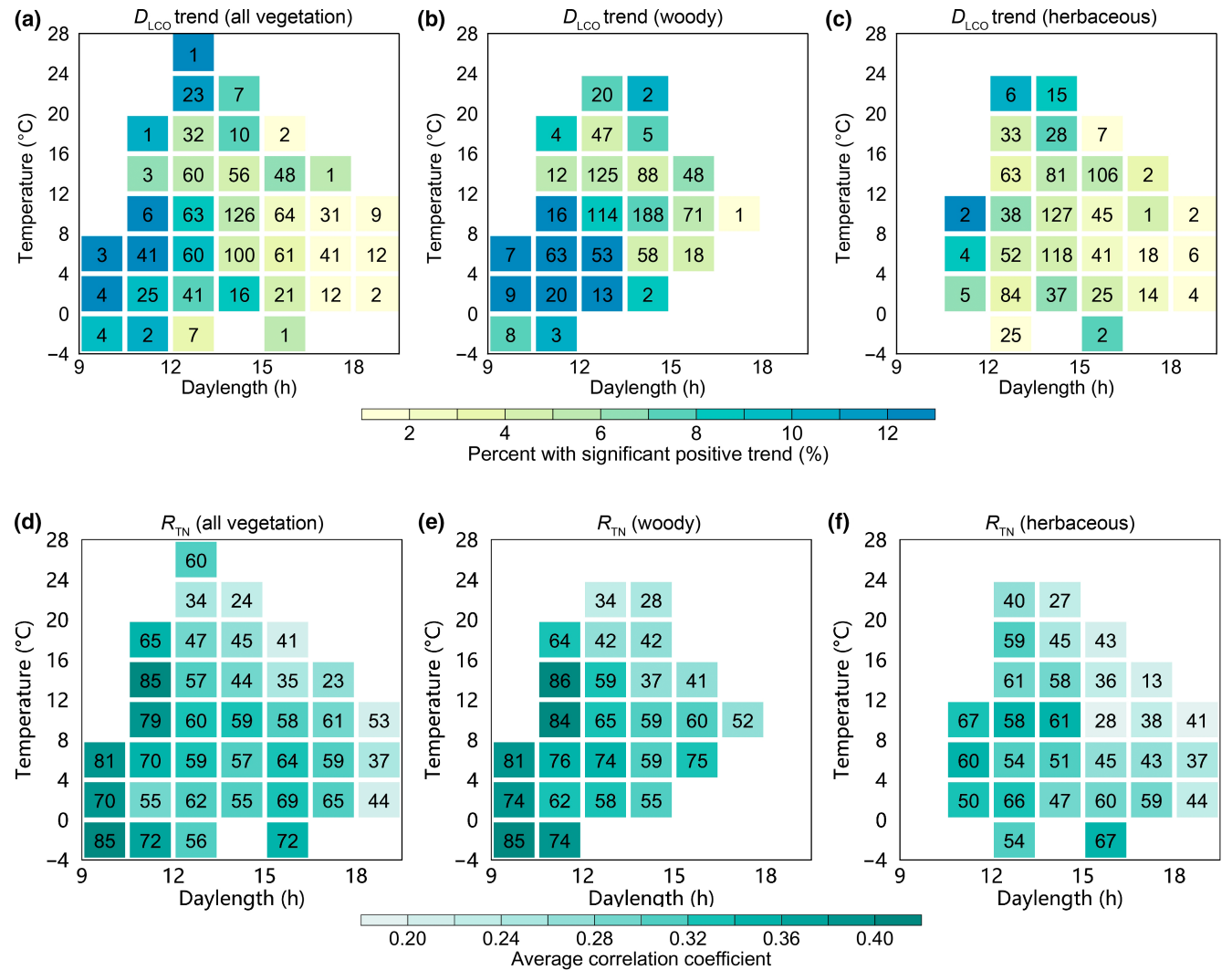


FIGURE 5 Dependence of temporal trends in the timing of the onset of leaf coloration [D_{LCO} , 10% decrease in normalized difference vegetation index (NDVI); a-c] and of the partial correlation coefficient (R_{TN} ; d-f) between D_{LCO} and pre- D_{LCO} mean daily minimum temperature (T_{min}) on daylength and temperature over the period 2000–2018. (a) All vegetation. Colour indicates the percentage of area with significant ($p < .05$) D_{LCO} delays in each cell (i.e., a specific temperature \times daylength combination), as indicated in the scale at the bottom. The number in each cell indicates the ratio (unit: %) of the area in each cell to the total area with D_{LCO} retrieval. The temporal trends and their significances were determined with ordinary least squares regression and t tests. (b,c) The same as (a), but for woody and herbaceous vegetation, respectively. (d) All vegetation. Colour indicates the average of the positive R_{TN} , as indicated in the scale at the bottom. The number in each cell indicates the percentage of area with a positive correlation in each cell. (e,f) The same as (d), but for woody and herbaceous vegetation, respectively. Only cells where the ratio of the area of the cell to the total area is $>1\%$ are represented.

stronger effect of precipitation in delaying D_{LCO} in herbaceous vegetation (Supporting Information Figures S9 and S23).

4 | DISCUSSION

In previous analyses of *in situ* and satellite observations (Garonna et al., 2014; Gill et al., 2015; Liu et al., 2016), the advanced stage of autumnal leaf senescence, indicated by D_{LCE} , was significantly delayed in a larger proportion of areas, or time series, than was D_{LCO} in our study. In the present study, D_{LCE} was also significantly delayed in more areas than D_{LCO} (Supporting Information Figure S8), probably because the timings of the earlier stages of leaf coloration determined from satellite data were less affected by T_{min} than the later stages (Figure 4a–c; Supporting Information Figure S15). Evidence for photoperiodic control of the start of leaf senescence (Fracheboud et al., 2009; Keskitalo et al., 2005) suggests that the early phases of leaf senescence are insensitive to warming, in contrast to the later phases. Given that the degradation of chlorophyll starts earlier than leaf coloration (Lim et al., 2007; Tang et al., 2016), the timing of autumnal phenological metrics that closely follow chlorophyll degradation before D_{LCO} should be less delayed by temperature increase than D_{LCO} if chlorophyll degradation is triggered by the photoperiod. In our analysis, we verified that D_{PDO} was less positively correlated with temperature than D_{LCO} (Supporting Information Table S7), probably because the start of autumnal chlorophyll degradation was controlled by photoperiod and was not delayed by higher temperature (Bauerle et al., 2012; Fracheboud et al., 2009; Keskitalo et al., 2005).

Overall, our results suggest that temperature does not initiate senescence in autumn in most areas; instead, it influences the speed of change in coloration after it starts (Figure 4f) (Fracheboud et al., 2009). The lack of a positive correlation between D_{LCO} (or D_{PDO}) and pre- D_{LCO} (or pre- D_{PDO}) temperature suggests an overriding photoperiodic control that makes the timing of the onset of leaf senescence stable. In the areas with longer daylengths (calculated for each pixel/location at multiyear mean D_{LCO} over 2000–2018), there were proportionally fewer significant D_{LCO} delays during 2000–2018 (Figure 5a; Supporting Information Figure S19a), and the positive relationship between D_{LCO} and pre- D_{LCO} T_{min} was slightly weaker, as indicated by the smaller partial correlation coefficient between them (Figure 5d). Such dependences on daylength were more prominent for woody vegetation than for herbaceous vegetation (Figure 5b,c,e,f; Supporting Information Figure S19b,c), in agreement with experimental findings suggesting that the initiation of leaf senescence in woody plants is likely to be controlled by photoperiod (Fracheboud et al., 2009; Keskitalo et al., 2005). These findings indicate stronger photoperiodic control in areas where daylength at D_{LCO} is longer (i.e., shorter nights), possibly because plants respond to the duration of uninterrupted darkness rather than daylength (Borthwick & Hendricks, 1960; Hamner, 1940; Howe et al., 1995; Paus et al., 1986). Interestingly, for vegetation with a daylength at D_{LCO} of >13.5h, D_{LCO} was more positively correlated with pre- D_{LCO} T_{min} in colder areas (Figure 5d–f), indicating a stronger effect of temperature in areas with harsh

temperature conditions, consistent with experimental studies (Ford et al., 2017; Zohner et al., 2016). Therefore, although for these types of vegetation the correlation between D_{LCO} and temperature is weak, probably because of stronger photoperiodic control, there is still a signal of temperature influence on D_{LCO} , reflecting a stronger selection pressure in harsher temperature environments.

Although observational evidence is limited, experimental results have been reported for the photoperiodic induction of leaf senescence in several, mostly woody, species (Supporting Information Table S1). However, in those manipulative experiments, daylength was altered by several hours (>4 h; Supporting Information Table S1), which is more extreme than the natural conditions plants are likely to experience. Daylength depends only on the day of year and location. Owing to the interannual limited variations in the timings of leaf coloration or senescence onset, the fluctuation in daylength in natural conditions is far less than that in manipulative experiments. Therefore, the role of photoperiod in leaf senescence identified in such experimental conditions does not necessarily apply to plants in natural conditions. The results in the present study support experimental findings in wild plants at the biome and continental scales and show that photoperiod influences the onset of leaf coloration, which closely follows the initiation of leaf senescence.

Autumnal leaf senescence in preparation for overwintering is an evolutionary trade-off between the re-allocation of leaf nutrients before leaf shed to reduce the risk of frost damage and the assimilation of carbon (Estiarte & Peñuelas, 2015). The response of leaf senescence to an increase in temperature in autumn influences this trade-off. The absence of delays over time in the onset of leaf coloration and in the onset of decrease in maximum canopy photosynthetic capacity in response to climate warming, as observed in our study, might limit the detrimental effects of frost in autumn (Liu et al., 2018) and might also have limited impacts on the start of the remobilization and resorption of nutrients (Estiarte & Peñuelas, 2015). The slower rate of progress of leaf senescence (Figure 4f) and extended duration of leaf coloration (Figure 4e) under warming might increase the efficiency of nitrogen resorption (Rennenberg et al., 2010) and increase the vegetation greenness in this period, which will modify the surface energy balance through biophysical processes (Shen et al., 2015). The extended period of leaf coloration might also prolong the plant transpiration time and increase soil water consumption. The impact of autumn warming on net ecosystem productivity is dual, increasing both respiratory flux to the atmosphere (Piao et al., 2008) and forest gross primary photosynthesis (Keenan et al., 2014). The relatively static onset date of leaf coloration and its weak response to temperature would preclude the vegetation from fully using the potential increase in CO_2 assimilation in early autumn induced by warming (Stinziano & Way, 2017). Combined with a delay in the end of the season and an increase in respiration attributable to warming, this suggests that additional warming will probably not result in a continuous increase in autumn CO_2 assimilation.

In summary, satellite NDVI time series and ground-based phenological observations indicated no significant delay in the start of

autumnal leaf coloration for most areas covered by natural vegetation over middle and high northern latitudes. Neither pre- D_{LCO} temperature nor pre- D_{LCO} precipitation significantly affected the interannual variations of the start of leaf coloration in most areas, indicating that the start of leaf senescence is triggered by photoperiod. Interestingly, there was a weaker positive correlation between the start of autumnal leaf coloration and pre- $D_{\text{LCO}} T_{\text{min}}$ for vegetation in regions with longer daylength, indicating strong photoperiodic control of the start of leaf senescence. For vegetation with a given daylength at $D_{\text{LCO}} > 13.5$ h, the positive correlation between D_{LCO} and pre- $D_{\text{LCO}} T_{\text{min}}$ was slightly stronger in colder areas, suggesting that there is strong selection pressure in harsher temperature environments on the timing of leaf coloration onset, and that autumn warming could have a stronger delaying effect on leaf coloration onset in colder areas than in warmer areas. This study suggests that autumnal warming will not change the start date of leaf senescence, but it might slow the rate of senescence. A slower senescence speed might extend the period of senescence and provide more time to re-allocate nutrients and prepare for overwintering. Such changes could substantially affect carbon and nutrient cycles. Our study provides a foundation for understanding the complex relationships among nutrient cycling, vegetation growth, energy exchange and climate change in autumn in temperate and boreal regions dominated by winter deciduous vegetation.

AUTHOR CONTRIBUTIONS

M.S. designed the research and conceived the study; N.J. and M.S. performed the research; N.J. analysed the data; and all the authors interpreted the results and wrote the paper.

ACKNOWLEDGMENTS

This work was funded by the Second Scientific Expedition to the Qinghai-Tibet Plateau (no. 2019QZKK0307) and the Fundamental Research Funds for the Central Universities. M.C. wishes to acknowledge the ERC Starting Grant LEAF-FALL (714916). J.P. acknowledges financial support from the European Research Council Synergy (grant no. ERC-SyG-2013-610028 IMBALANCE-P). L.Š. was supported by the Ministry of Education, Youth and Sports of the Czech Republic within the CzeCOS programme (grant no. LM2015061) and by SustES—Adaptation Strategies for Sustainable Ecosystem Services and Food Security Under Adverse Environmental Conditions (project no. CZ.02.1.01/0.0/0.0/16_019/0000797).

DATA AVAILABILITY STATEMENT

All data used for this study are publicly available online. The satellite reflectance products at .05° resolution (MOD09CMG) used to estimate phenological metrics and the global land cover map (MCD12C1-2009) used to identify natural vegetation are freely available online at: <https://ladsweb.modaps.eosdis.nasa.gov>. The PhenoCam data (PhenoCam Dataset v.2.0) used to evaluate the satellite-derived phenological metrics are available at: <https://doi.org/10.3334/ORNLD AAC/1674>; and the subsets of satellite reflectance products at 500-m resolution (MOD09A1) at PhenoCam sites are downloaded from: <https://modis.ornl.gov/globalsubset/>. The climatic data for the region

are publicly available: CRU TS 4.03 monthly climatic data are available via <http://data.ceda.ac.uk>; and CRU-NCEP v.7.2 6-hourly climatic data are available via <https://vesg.ipsl.upmc.fr>. *In situ* phenological observations in China are available from the National Earth System Science Data Sharing Infrastructure, National Science and Technology Infrastructure of China (<http://www.geodata.cn>). The climatic data of *in situ* observations in China are available from National Meteorological Information Center (<http://data.tpdc.ac.cn>). The site-based gross primary productivity products used to estimate phenological metrics and the corresponding half-hourly climatic data are extracted from the FLUXNET2015 Dataset (<http://fluxnet.fluxdata.org/data/fluxnet2015-dataset/>). The source code of the spatial-temporal Savitzky-Golay filter is available at: https://github.com/cao-sre/STSG_IDL_program. The codes for analyses are available from figshare (<https://figshare.com/s/be760555bb74ef0e6bf2>).

ORCID

Nan Jiang  <https://orcid.org/0000-0001-5151-5715>

Miaogen Shen  <https://orcid.org/0000-0001-5742-8807>

Shilong Piao  <https://orcid.org/0000-0001-8057-2292>

Eryuan Liang  <https://orcid.org/0000-0002-8003-4264>

REFERENCES

- Bauerle, W. L., Oren, R., Way, D. A., Qian, S. S., Stoy, P. C., Thornton, P. E., Bowden, J. D., Hoffman, F. M., & Reynolds, R. F. (2012). Photoperiodic regulation of the seasonal pattern of photosynthetic capacity and the implications for carbon cycling. *Proceedings of the National Academy of Sciences of the United States of America*, 109(22), 8612–8617. <https://doi.org/10.1073/pnas.1119131109>
- Beck, P. S. A., Atzberger, C., Høgda, K. A., Johansen, B., & Skidmore, A. K. (2006). Improved monitoring of vegetation dynamics at very high latitudes: A new method using MODIS NDVI. *Remote Sensing of Environment*, 100(3), 321–334. <https://doi.org/10.1016/j.rse.2005.10.021>
- Berman, E. E., Graves, T. A., Mickle, N. L., Merkle, J. A., Johnston, A. N., & Chong, G. W. (2020). Comparative quality and trend of remotely sensed phenology and productivity metrics across the western United States. *Remote Sensing*, 12(16), 2538. <https://doi.org/10.3390/rs12162538>
- Borthwick, H. A., & Hendricks, S. B. (1960). Photoperiodism in plants. *Science*, 132(3435), 1223–1228. <https://doi.org/10.1126/science.132.3435.1223>
- Buitenwerf, R., Rose, L., & Higgins, S. I. (2015). Three decades of multi-dimensional change in global leaf phenology. *Nature Climate Change*, 5(4), 364–368. <https://doi.org/10.1038/nclimate2533>
- Cao, R., Chen, Y., Shen, M., Chen, J., Zhou, J., Wang, C., & Yang, W. (2018). A simple method to improve the quality of NDVI time-series data by integrating spatiotemporal information with the Savitzky-Golay filter. *Remote Sensing of Environment*, 217, 244–257. <https://doi.org/10.1016/j.rse.2018.08.022>
- Chen, J., Rao, Y., Shen, M., Wang, C., Zhou, Y., Ma, L., Tang, Y., & Yang, X. (2016). A simple method for detecting phenological change from time series of vegetation index. *IEEE Transactions on Geoscience and Remote Sensing*, 54(6), 3436–3449. <https://doi.org/10.1109/TGRS.2016.2518167>
- China Meteorological Administration. (1993). *Observation criterion of agricultural meteorology*. China Meteorological Press (in Chinese).
- Cong, N., Shen, M., & Piao, S. (2017). Spatial variations in responses of vegetation autumn phenology to climate change on the

- Tibetan Plateau. *Journal of Plant Ecology*, 10, 744–752. <https://doi.org/10.1093/jpe/rtw084>
- Delpierre, N., Dufrene, E., Soudani, K., Ulrich, E., Cecchini, S., Boé, J., & François, C. (2009). Modelling interannual and spatial variability of leaf senescence for three deciduous tree species in France. *Agricultural and Forest Meteorology*, 149(6), 938–948. <https://doi.org/10.1016/j.agrformet.2008.11.014>
- Elmore, A. J., Guinn, S. M., Minsley, B. J., & Richardson, A. D. (2012). Landscape controls on the timing of spring, autumn, and growing season length in mid-Atlantic forests. *Global Change Biology*, 18(2), 656–674. <https://doi.org/10.1111/j.1365-2486.2011.02521.x>
- Estiarte, M., & Peñuelas, J. (2015). Alteration of the phenology of leaf senescence and fall in winter deciduous species by climate change: Effects on nutrient proficiency. *Global Change Biology*, 21(3), 1005–1017. <https://doi.org/10.1111/gcb.12804>
- Estrella, N., & Menzel, A. (2006). Responses of leaf colouring in four deciduous tree species to climate and weather in Germany. *Climate Research*, 32(3), 253–267.
- Ford, K. R., Harrington, C. A., & Clair, J. B. S. (2017). Photoperiod cues and patterns of genetic variation limit phenological responses to climate change in warm parts of species' range: Modeling diameter-growth cessation in coast Douglas-fir. *Global Change Biology*, 23(8), 3348–3362. <https://doi.org/10.1111/gcb.13690>
- Fracheboud, Y., Luquez, V., Björkén, L., Sjödin, A., Tuominen, H., & Jansson, S. (2009). The control of autumn senescence in European aspen. *Plant Physiology*, 149(4), 1982–1991. <https://doi.org/10.1104/pp.108.133249>
- Friedl, M., & Sulla-Menashe, D. (2015). MCD12C1 MODIS/Terra+Aqua Land Cover Type Yearly L3 Global 0.05Deg CMG V006 [Data set]. NASA EOSDIS Land Processes DAAC. <https://doi.org/10.5067/MODIS/MCD12C1.006>
- Fu, Y. H., Zhang, X., Piao, S., Hao, F., Geng, X., Vitasse, Y., Zohner, C., Peñuelas, J., & Janssens, I. A. (2019). Daylength helps temperate deciduous trees to leaf-out at the optimal time. *Global Change Biology*, 25(7), 2410–2418. <https://doi.org/10.1111/gcb.14633>
- Fu, Y. H., Zhao, H., Piao, S., Peaucelle, M., Peng, S., Zhou, G., Ciais, P., Huang, M., Menzel, A., Peñuelas, J., Song, Y., Vitasse, Y., Zeng, Z., & Janssens, I. A. (2015). Declining global warming effects on the phenology of spring leaf unfolding. *Nature*, 526(7571), 104–107. <https://doi.org/10.1038/nature15402>
- Fu, Y. S. H., Campioli, M., Vitasse, Y., De Boeck, H. J., Van den Berge, J., AbdElgawad, H., Asard, H., Piao, S., Deckmyn, G., & Janssens, I. A. (2014). Variation in leaf flushing date influences autumnal senescence and next year's flushing date in two temperate tree species. *Proceedings of the National Academy of Sciences of the United States of America*, 111(20), 7355–7360. <https://doi.org/10.1073/pnas.1321727111>
- Gan, S. S., & Amasino, R. M. (1997). Making sense of senescence - Molecular genetic regulation and manipulation of leaf senescence. *Plant Physiology*, 113(2), 313–319. <https://doi.org/10.1104/pp.113.2.313>
- Ganguly, S., Friedl, M. A., Tan, B., Zhang, X., & Verma, M. (2010). Land surface phenology from MODIS: Characterization of the collection 5 global land cover dynamics product. *Remote Sensing of Environment*, 114(8), 1805–1816. <https://doi.org/10.1016/j.rse.2010.04.005>
- Gao, M., Piao, S., Chen, A., Yang, H., Liu, Q., Fu, Y. H., & Janssens, I. A. (2019). Divergent changes in the elevational gradient of vegetation activities over the last 30 years. *Nature Communications*, 10(1), 2970. <https://doi.org/10.1038/s41467-019-11035-w>
- Garonna, I., De Jong, R., De Wit, A. J. W., Múcher, C. A., Schmid, B., & Schaepman, M. E. (2014). Strong contribution of autumn phenology to changes in satellite-derived growing season length estimates across Europe (1982–2011). *Global Change Biology*, 20(11), 3457–3470.
- Ge, Q. S., Wang, H. J., Rutishauser, T., & Dai, J. H. (2015). Phenological response to climate change in China: A meta-analysis. *Global Change Biology*, 21(1), 265–274.
- Gill, A. L., Gallinat, A. S., Sanders-DeMott, R., Rigden, A. J., Short Gianotti, D. J., Mantooth, J. A., & Templer, P. H. (2015). Changes in autumn senescence in northern hemisphere deciduous trees: A meta-analysis of autumn phenology studies. *Annals of Botany*, 116(6), 875–888. <https://doi.org/10.1093/aob/mcv055>
- Gu, L., Post, W. M., Baldocchi, D. D., Black, T. A., Suyker, A. E., Verma, S. B., Vesala, T., & Wofsy, S. C. (2009). Characterizing the seasonal dynamics of plant community photosynthesis across a range of vegetation types. In A. Noormets (Ed.), *Phenology of ecosystem processes* (pp. 35–58). Springer.
- Hamner, K. C. (1940). Interrelation of light and darkness in photoperiod. *Botanical Gazette*, 101(3), 658–687.
- Harris, I., Jones, P. D., Osborn, T. J., & Lister, D. H. (2014). Updated high-resolution grids of monthly climatic observations – the CRU TS3.10 Dataset. *International Journal of Climatology*, 34(3), 623–642. <https://doi.org/10.1002/joc.3711>
- Howe, G. T., Hackett, W. P., Furnier, G. R., & Klevorn, R. E. (1995). Photoperiodic responses of a northern and southern ecotype of black cottonwood. *Physiologia Plantarum*, 93(4), 695–708.
- Jeganathan, C., Dash, J., & Atkinson, P. M. (2014). Remotely sensed trends in the phenology of northern high latitude terrestrial vegetation, controlling for land cover change and vegetation type. *Remote Sensing of Environment*, 143, 154–170. <https://doi.org/10.1016/j.rse.2013.11.020>
- Jeong, S. J., Ho, C. H., Gim, H. J., & Brown, M. E. (2011). Phenology shifts at start vs. end of growing season in temperate vegetation over the Northern Hemisphere for the period 1982–2008. *Global Change Biology*, 17(7), 2385–2399.
- Keenan, T. F., Gray, J., Friedl, M. A., Toomey, M., Bohrer, G., Hollinger, D. Y., Munger, J. W., O'Keefe, J., Schmid, H. P., Wing, I. S., Yang, B., & Richardson, A. D. (2014). Net carbon uptake has increased through warming-induced changes in temperate forest phenology. *Nature Climate Change*, 4(7), 598–604. <https://doi.org/10.1038/nclimate2253>
- Keenan, T. F., & Richardson, A. D. (2015). The timing of autumn senescence is affected by the timing of spring phenology: Implications for predictive models. *Global Change Biology*, 21(7), 2634–2641. <https://doi.org/10.1111/gcb.12890>
- Keskitalo, J., Bergquist, G., Gardeström, P., & Jansson, S. (2005). A cellular timetable of autumn senescence. *Plant Physiology*, 139(4), 1635–1648. <https://doi.org/10.1104/pp.105.066845>
- Klosterman, S., & Richardson, A. D. (2017). Observing spring and fall phenology in a deciduous forest with aerial drone imagery. *Sensors (Basel)*, 17(12), 2852. <https://doi.org/10.3390/s17122852>
- Klosterman, S. T., Hufkens, K., Gray, J. M., Melaas, E., Sonnentag, O., Lavine, I., Mitchell, L., Norman, R., Friedl, M. A., & Richardson, A. D. (2014). Evaluating remote sensing of deciduous forest phenology at multiple spatial scales using PhenoCam imagery. *Biogeosciences*, 11(16), 4305–4320. <https://doi.org/10.5194/bg-11-4305-2014>
- Körner, C. (2007). Significance of temperature in plant life. In J. I. L. Morison & M. D. Morecroft (Eds.), *Plant growth and climate change* (pp. 48–69). Blackwell Publishing Ltd.
- Körner, C. (2021). *Alpine plant life: Functional plant ecology of high mountain ecosystems*. Springer International Publishing.
- Körner, C., & Basler, D. (2010). Response-warming, photoperiods, and tree phenology. *Science*, 329(5989), 278. <https://doi.org/10.1126/science.329.5989.278>
- Körner, C., & Hiltbrunner, E. (2018). The 90 ways to describe plant temperature. *Perspectives in Plant Ecology, Evolution and Systematics*, 30, 16–21. <https://doi.org/10.1016/j.ppees.2017.04.004>
- Leblans, N. I. W., Sigurdsson, B. D., Vicca, S., Fu, Y. S., Peñuelas, J., & Janssens, I. A. (2017). Phenological responses of Icelandic subarctic grasslands to short-term and long-term natural soil warming. *Global Change Biology*, 23(11), 4932–4945.

- Lenz, A., Hoch, G., Vitasse, Y., & Körner, C. (2013). European deciduous trees exhibit similar safety margins against damage by spring freeze events along elevational gradients. *New Phytologist*, 200(4), 1166–1175. <https://doi.org/10.1111/nph.12452>
- Lim, P. O., Kim, H. J., & Nam, H. G. (2007). Leaf senescence. *Annual Review of Plant Biology*, 58, 115–136. <https://doi.org/10.1146/annurev-arplant.07.0602-0115>
- Liu, Q., Fu, Y. H., Zhu, Z., Liu, Y., Liu, Z., Huang, M., Janssens, I. A., & Piao, S. (2016). Delayed autumn phenology in the Northern Hemisphere is related to change in both climate and spring phenology. *Global Change Biology*, 22(11), 3702–3711.
- Liu, Q., Piao, S., Janssens, I. A., Fu, Y., Peng, S., Lian, X., Ciais, P., Myneni, R. B., Peñuelas, J., & Wang, T. (2018). Extension of the growing season increases vegetation exposure to frost. *Nature Communications*, 9(1), 426. <https://doi.org/10.1038/s41467-017-02690-y>
- Lukasová, V., Bucha, T., Škvareninová, J., & Škvarenina, J. (2019). Validation and application of European beech phenological metrics derived from MODIS data along an altitudinal gradient. *Forests*, 10(1), 60.
- Mariën, B., Balzarolo, M., Dox, I., Leys, S., Lorène, M. J., Geron, C., Portillo-Estrada, M., AbdElgawad, H., Asard, H., & Campioli, M. (2019). Detecting the onset of autumn leaf senescence in deciduous forest trees of the temperate zone. *New Phytologist*, 224(1), 166–176.
- Matsumoto, K., Ohta, T., Irasawa, M., & Nakamura, T. (2003). Climate change and extension of the *Ginkgo biloba* L. growing season in Japan. *Global Change Biology*, 9(11), 1634–1642. <https://doi.org/10.1046/j.1365-2486.2003.00688.x>
- Melaas, E. K., Friedl, M. A., & Zhu, Z. (2013). Detecting interannual variation in deciduous broadleaf forest phenology using Landsat TM/ETM+ data. *Remote Sensing of Environment*, 132, 176–185. <https://doi.org/10.1016/j.rse.2013.01.011>
- Menzel, A., Yuan, Y., Matiu, M., Sparks, T., Scheifinger, H., Gehrig, R., & Estrella, N. (2020). Climate change fingerprints in recent European plant phenology. *Global Change Biology*, 26(4), 2599–2612. <https://doi.org/10.1111/gcb.15000>
- Morissette, J. T., Richardson, A. D., Knapp, A. K., Fisher, J. I., Graham, E. A., Abatzoglou, J., Wilson, B. E., Breshears, D. D., Henebry, G. M., Hanes, J. M., & Liang, L. (2009). Tracking the rhythm of the seasons in the face of global change: Phenological research in the 21st century. *Frontiers in Ecology and the Environment*, 7(5), 253–260. <https://doi.org/10.1890/070217>
- Myneni, R. B., Keeling, C. D., Tucker, C. J., Asrar, G., & Nemani, R. R. (1997). Increased plant growth in the northern high latitudes from 1981 to 1991. *Nature*, 386(6626), 698–702. <https://doi.org/10.1038/386698a0>
- Nagai, S., Nasahara, K. N., Muraoka, H., Akiyama, T., & Tsuchida, S. (2010). Field experiments to test the use of the normalized-difference vegetation index for phenology detection. *Agricultural and Forest Meteorology*, 150(2), 152–160. <https://doi.org/10.1016/j.agrformet.2009.09.010>
- Nezval, O., Krejza, J., Světlík, J., Šigut, L., & Horáček, P. (2020). Comparison of traditional ground-based observations and digital remote sensing of phenological transitions in a floodplain forest. *Agricultural and Forest Meteorology*, 291, 108079. <https://doi.org/10.1016/j.agrformet.2020.108079>
- Pastorello, G. Z., Papale, D., Chu, H., Trotta, C., Agarwal, D. A., Canfora, E., Baldocchi, D., & Torn, M. S. (2017). A new data set to keep a sharper eye on land-air exchanges. *Eos, Transactions American Geophysical Union (Online)*. <https://doi.org/10.1029/2017EO071597>
- Pau, S., Wolkovich, E. M., Cook, B. I., Davies, T. J., Kraft, N. J. B., Bolmgren, K., Betancourt, J. L., & Cleland, E. E. (2011). Predicting phenology by integrating ecology, evolution and climate science. *Global Change Biology*, 17(12), 3633–3643. <https://doi.org/10.1111/j.1365-2486.2011.02515.x>
- Paus, E., Nilsen, J., & Junntila, O. (1986). Bud dormancy and vegetative growth in salix-polaris as affected by temperature and photoperiod. *Polar Biology*, 6(2), 91–95.
- Peñuelas, J., Rutishauser, T., & Filella, I. (2009). Phenology feedbacks on climate change. *Science*, 324(5929), 887–888. <https://doi.org/10.1126/science.1173004>
- Piao, S., Ciais, P., Friedlingstein, P., Peylin, P., Reichstein, M., Luysaert, S., Margolis, H., Fang, J., Barr, A., Chen, A., Grelle, A., Hollinger, D. Y., Laurila, T., Lindroth, A., Richardson, A. D., & Vesala, T. (2008). Net carbon dioxide losses of northern ecosystems in response to autumn warming. *Nature*, 451(7174), 49–52. <https://doi.org/10.1038/nature06444>
- Ren, J., Campbell, J., & Shao, Y. (2017). Estimation of SOS and EOS for midwestern US corn and soybean crops. *Remote Sensing*, 9(7), 722. <https://doi.org/10.3390/rs9070722>
- Rennenberg, H., Wildhagen, H., & Ehling, B. (2010). Nitrogen nutrition of poplar trees. *Plant Biology*, 12(2), 275–291. <https://doi.org/10.1111/j.1438-8677.2009.00309.x>
- Richardson, A. D., Hufkens, K., Milliman, T., & Froking, S. (2018). Intercomparison of phenological transition dates derived from the PhenoCam Dataset V1.0 and MODIS satellite remote sensing. *Scientific Reports*, 8, 5679.
- Richardson, A. D., Keenan, T. F., Migliavacca, M., Ryu, Y., Sonnentag, O., & Toomey, M. (2013). Climate change, phenology, and phenological control of vegetation feedbacks to the climate system. *Agricultural and Forest Meteorology*, 169, 156–173. <https://doi.org/10.1016/j.agrformet.2012.09.012>
- Saikkonen, K., Taulavuori, K., Hyvönen, T., Gundel, P. E., Hamilton, C. E., Vänninen, I., Nissinen, A., & Helander, M. (2012). Climate change-driven species' range shifts filtered by photoperiodism. *Nature Climate Change*, 2(4), 239–242. <https://doi.org/10.1038/nclimate1430>
- Sakai, A., & Larcher, W. (1987). *Frost survival of plants* (Vol. 62). Springer Berlin Heidelberg.
- Sen, P. K. (1968). Estimates of the regression coefficient based on Kendall's Tau. *Journal of the American Statistical Association*, 63(324), 1379–1389. <https://doi.org/10.1080/01621459.1968.10480934>
- Seyednasrollah, B., Young, A. M., Hufkens, K., Milliman, T., Friedl, M. A., Froking, S., & Richardson, A. D. (2019). Tracking vegetation phenology across diverse biomes using Version 2.0 of the PhenoCam Dataset. *Scientific Data*, 6(1), 222. <https://doi.org/10.1038/s41597-019-0229-9>
- Seyednasrollah, B., Young, A. M., Hufkens, K., Milliman, T., Friedl, M. A., Froking, S., Richardson, A. D., Abraha, M., Allen, D. W., Apple, M., Arain, M. A., Baker, J., Baker, J. M., Baldocchi, D., Bernacchi, C. J., Bhattacharjee, J., Blanken, P., Bosch, D. D., Boughton, R., ... Zona, D. (2019). *PhenoCam dataset v2.0: Vegetation phenology from digital camera imagery, 2000–2018*. ORNL Distributed Active Archive Center.
- Shang, R., Liu, R., Xu, M., Liu, Y., Zuo, L., & Ge, Q. (2017). The relationship between threshold-based and inflexion-based approaches for extraction of land surface phenology. *Remote Sensing of Environment*, 199, 167–170. <https://doi.org/10.1016/j.rse.2017.07.020>
- Shen, M., Jiang, N., Peng, D., Rao, Y., Huang, Y., Fu, Y. H., Yang, W., Zhu, X., Cao, R., Chen, X., Chen, J., Miao, C., Wu, C., Wang, T., Liang, E., & Tang, Y. (2020). Can changes in autumn phenology facilitate earlier green-up date of northern vegetation? *Agricultural and Forest Meteorology*, 291, 108077. <https://doi.org/10.1016/j.agrformet.2020.108077>
- Shen, M., Tang, Y., Desai, A. R., Gough, C., & Chen, J. (2014). Can EVI-derived land-surface phenology be used as a surrogate for phenology of canopy photosynthesis? *International Journal of Remote Sensing*, 35(3), 1162–1174. <https://doi.org/10.1080/01431161.2013.875636>
- Shen, M., Zhang, G., Cong, N., Wang, S., Kong, W., & Piao, S. (2014). Increasing altitudinal gradient of spring vegetation phenology during the last decade on the Qinghai-Tibetan Plateau. *Agricultural and Forest Meteorology*, 189–190, 71–80. <https://doi.org/10.1016/j.agrformet.2014.01.003>

- Shen, M. G., Piao, S. L., Jeong, S. J., Zhou, L. M., Zeng, Z. Z., Ciais, P., Chen, D., Huang, M., Jin, C.-S., Li, L. Z. X., Li, Y., Myneni, R. B., Yang, K., Zhang, G., Zhang, Y., & Yao, T. D. (2015). Evaporative cooling over the Tibetan Plateau induced by vegetation growth. *Proceedings of the National Academy of Sciences of the United States of America*, 112(30), 9299–9304. <https://doi.org/10.1073/pnas.1504418112>
- Soudani, K., Delpierre, N., Berveiller, D., Hmimina, G., & Dufrêne, R. (2021). A survey of proximal methods for monitoring leaf phenology in temperate deciduous forests. *Biogeosciences*, 18(11), 3391–3408.
- Soudani, K., Hmimina, G., Delpierre, N., Pontailier, J. Y., Aubinet, M., Bonal, D., Caquet, B., de Grandcourt, A., Burban, B., Flechard, C., Guyon, D., Granier, A., Gross, P., Heinesh, B., Longdoz, B., Loustau, D., Moureaux, C., Ourcival, J.-M., Rambal, S., ... Dufrêne, E. (2012). Ground-based network of NDVI measurements for tracking temporal dynamics of canopy structure and vegetation phenology in different biomes. *Remote Sensing of Environment*, 123, 234–245. <https://doi.org/10.1016/j.rse.2012.03.012>
- Stinziano, J. R., & Way, D. A. (2017). Autumn photosynthetic decline and growth cessation in seedlings of white spruce are decoupled under warming and photoperiod manipulations. *Plant, Cell & Environment*, 40(8), 1296–1316. <https://doi.org/10.1111/pce.12917>
- Tang, J., Körner, C., Muraoka, H., Piao, S., Shen, M., Thackeray, S. J., & Yang, X. (2016). Emerging opportunities and challenges in phenology: A review. *Ecosphere*, 7(8), e01436.
- Taschler, D., & Neuner, G. (2004). Summer frost resistance and freezing patterns measured in situ in leaves of major alpine plant growth forms in relation to their upper distribution boundary. *Plant, Cell and Environment*, 27(6), 737–746. <https://doi.org/10.1111/j.1365-3040.2004.01176.x>
- Theil, H. (1992). A rank-invariant method of linear and polynomial regression analysis. In B. Raj & J. Koerts (Eds.), *Henri Theil's contributions to economics and econometrics: Econometric theory and methodology* (Vol. 23, pp. 345–381). Springer Netherlands.
- Thomas, H., & Stoddart, J. L. (1980). Leaf senescence. *Annual Review of Plant Physiology and Plant Molecular Biology*, 31, 83–111. <https://doi.org/10.1146/annurev.pp.31.060180.000503>
- Vermote, E. F. (2015). MOD09CMG MODIS/Terra surface reflectance daily L3 Global 0.05Deg CMG V006 [Data set]. NASA EOSDIS Land Processes DAAC. <https://doi.org/10.5067/MODIS/MOD09CMG.006>
- Viovy, N. (2018). CRUNCEP Version 7 - atmospheric forcing data for the community land model [Data set]. In *Research Data Archive at the National Center for Atmospheric Research*. Computational and Information Systems Laboratory. <https://doi.org/10.5067/MODIS/MOD09CMG.006>
- White, M. A., Thornton, P. E., & Running, S. W. (1997). A continental phenology model for monitoring vegetation responses to interannual climatic variability. *Global Biogeochemical Cycles*, 11(2), 217–234. <https://doi.org/10.1029/97gb00330>
- Wingate, L., Ogée, J., Cremonese, E., Filippa, G., Mizunuma, T., Migliavacca, M., Wilkinson, M., Moureaux, C., Wohlfahrt, G., Hammerle, A., Hörtnagl, L., Gimeno, C., Porcar-Castell, A., Galvagno, M., Nakaji, T., Morison, J., Kolle, O., Knohl, A., Kutsch, W., ... Grace, J. (2015). Interpreting canopy development and physiology using a European phenology camera network at flux sites. *Biogeosciences*, 12(20), 5995–6015. <https://doi.org/10.5194/bg-12-5995-2015>
- Wu, C., Wang, X., Wang, H., Ciais, P., Peñuelas, J., Myneni, R. B., Desai, A. R., Gough, C. M., Gonsamo, A., Black, A. T., Jassal, R. S., Ju, W., Yuan, W., Fu, Y., Shen, M., Li, S., Liu, R., Chen, J. M., & Ge, Q. (2018). Contrasting responses of autumn-leaf senescence to daytime and night-time warming. *Nature Climate Change*, 8(12), 1092–1096. <https://doi.org/10.1038/s41558-018-0346-z>
- Xu, C., Liu, H., Williams, A. P., Yin, Y., & Wu, X. (2016). Trends toward an earlier peak of the growing season in Northern Hemisphere mid-latitudes. *Global Change Biology*, 22(8), 2852–2860. <https://doi.org/10.1111/gcb.13224>
- Yang, X., Tang, J., & Mustard, J. F. (2014). Beyond leaf color: Comparing camera-based phenological metrics with leaf biochemical, biophysical, and spectral properties throughout the growing season of a temperate deciduous forest. *Journal of Geophysical Research: Biogeosciences*, 119(3), 181–191. <https://doi.org/10.1002/2013jg002460>
- Ye, Y., & Zhang, X. (2021). Exploration of global spatiotemporal changes of fall foliage coloration in deciduous forests and shrubs using the VIIRS land surface phenology product. *Science of Remote Sensing*, 4, 100030. <https://doi.org/10.1016/j.srs.2021.100030>
- Yu, H., Luedeling, E., & Xu, J. (2010). Winter and spring warming result in delayed spring phenology on the Tibetan Plateau. *Proceedings of the National Academy of Sciences of the United States of America*, 107(51), 22151–22156. <https://doi.org/10.1073/pnas.1012490107>
- Zhang, X. (2015). Reconstruction of a complete global time series of daily vegetation index trajectory from long-term AVHRR data. *Remote Sensing of Environment*, 156, 457–472. <https://doi.org/10.1016/j.rse.2014.10.012>
- Zhang, X., Friedl, M. A., Schaaf, C. B., Strahler, A. H., Hodges, J. C., Gao, F., Reed, B. C., & Huete, A. (2003). Monitoring vegetation phenology using MODIS. *Remote Sensing of Environment*, 84(3), 471–475.
- Zhang, X., Tarpley, D., & Sullivan, J. T. (2007). Diverse responses of vegetation phenology to a warming climate. *Geophysical Research Letters*, 34(19), L194. <https://doi.org/10.1029/2007gl031447>
- Zhao, B., Donnelly, A., & Schwartz, M. D. (2020). Evaluating autumn phenology derived from field observations, satellite data, and carbon flux measurements in a northern mixed forest, USA. *International Journal of Biometeorology*, 64(5), 713–727. <https://doi.org/10.1007/s00484-020-01861-9>
- Zohner, C. M., Benito, B. M., Svenning, J.-C., & Renner, S. S. (2016). Day length unlikely to constrain climate-driven shifts in leaf-out times of northern woody plants. *Nature Climate Change*, 6(12), 1120–1123. <https://doi.org/10.1038/nclimate3138>

BIOSKETCH

Miaogen Shen is a professor at the Beijing Normal University, China. He is interested in interactions between vegetation and climate. More information is available at: <https://www.researchgate.net/profile/Miaogen-Shen>.

SUPPORTING INFORMATION

Additional supporting information can be found online in the Supporting Information section at the end of this article.

How to cite this article: Jiang, N., Shen, M., Ciais, P., Campioli, M., Peñuelas, J., Körner, C., Cao, R., Piao, S., Liu, L., Wang, S., Liang, E., Delpierre, N., Soudani, K., Rao, Y., Montagnani, L., Hörtnagl, L., Paul-Limoges, E., Myneni, R., Wohlfahrt, G. ... Zhao, W. (2022). Warming does not delay the start of autumnal leaf coloration but slows its progress rate. *Global Ecology and Biogeography*, 00, 1–17. <https://doi.org/10.1111/geb.13581>

1
2
3
4
5
6
7
8
9
10
11
12

Supplementary Information for

Warming does not delay the start of autumnal leaf coloration but slows its progress rate

This PDF file includes:

Figures S1 to S23

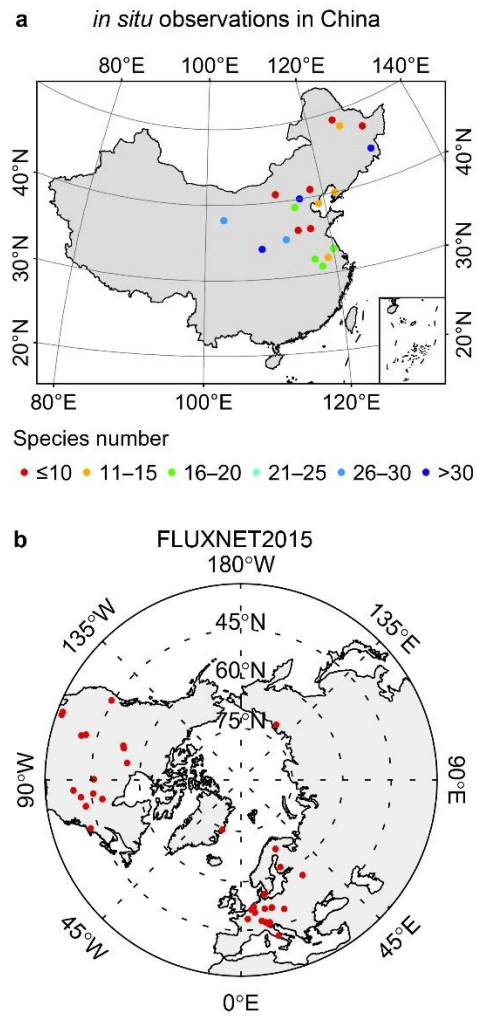
Tables S1 to S7

Supplementary Methods

Supplementary References

13 **Supplementary Figures**

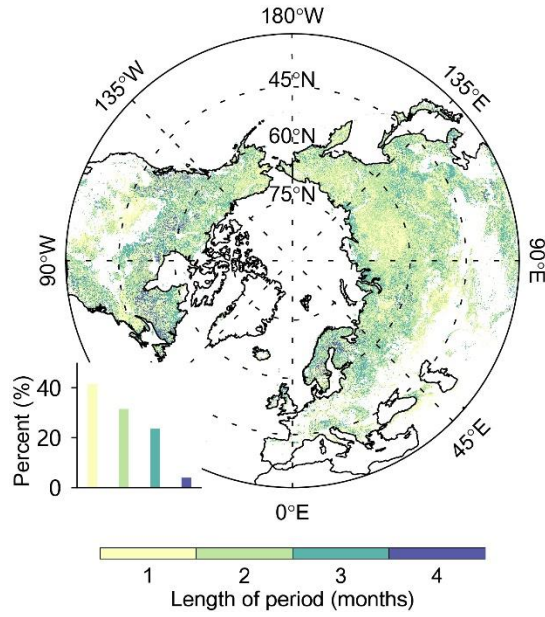
14
15



16

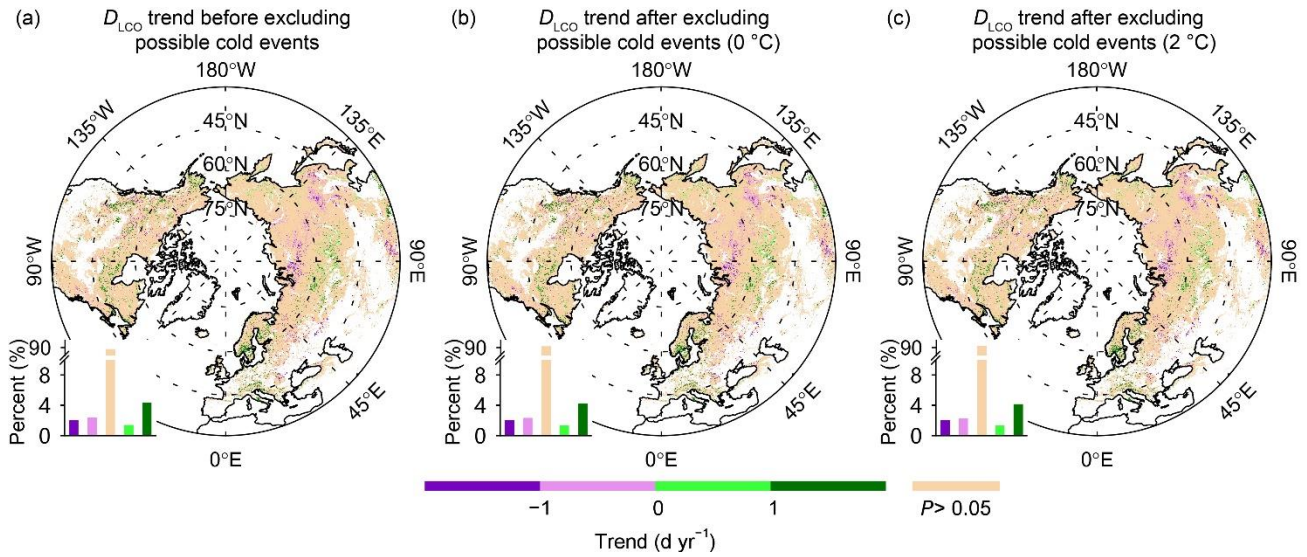
17 **Figure S1.** Locations of the sites of *in situ* observations used in this study. (a) phenological observation
18 sites in China. (b) FLUXNET2015 flux tower sites.

19



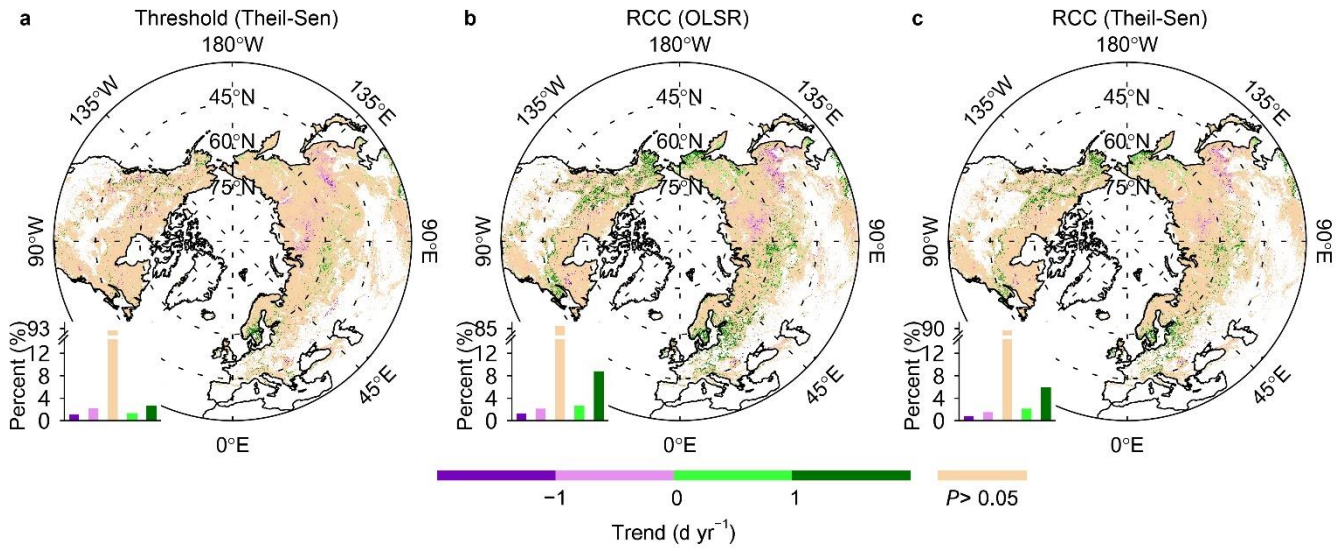
20
21
22
23
24

Figure S2. Spatial pattern of the length of the pre-DLCO period for mean daily minimum temperature (T_{min}). The bar chart shows the percentage of area for each interval of the length of the pre-DLCO period, with the length indicated by the color scale at the bottom.



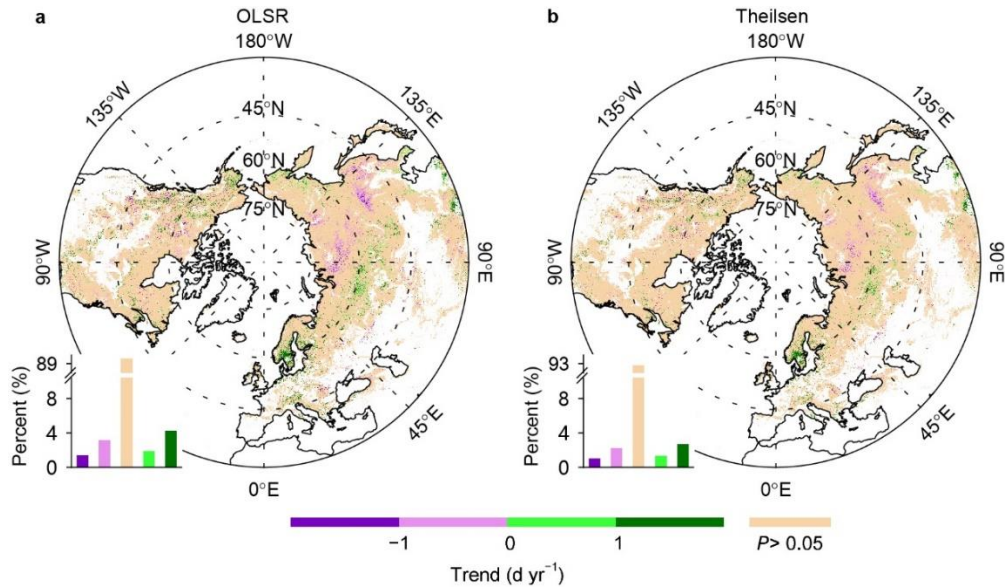
25
26
27
28
29
30
31
32
33
34

Figure S3. Temporal trends in timing of the onset of leaf coloration (D_{LCO}), retrieved from satellite images over the period 2000–2016 before (a) and after (b and c) the exclusion of years with possible cold events before D_{LCO} . Cold events were determined mainly by using a threshold-based method with daily minimum temperatures of 0 °C (b) or 2 °C (c). The bar chart in each panel shows the percentage of area within each interval of the significant temporal trends and the percentage of area with nonsignificant trends, indicated by the color scale at the bottom. The percentage for each interval of the trend is provided in Table S4. D_{LCO} corresponds to a 10% decrease in NDVI. Significant temporal trends were determined by using t -tests at $P < 0.05$ and ordinary least squares regression.



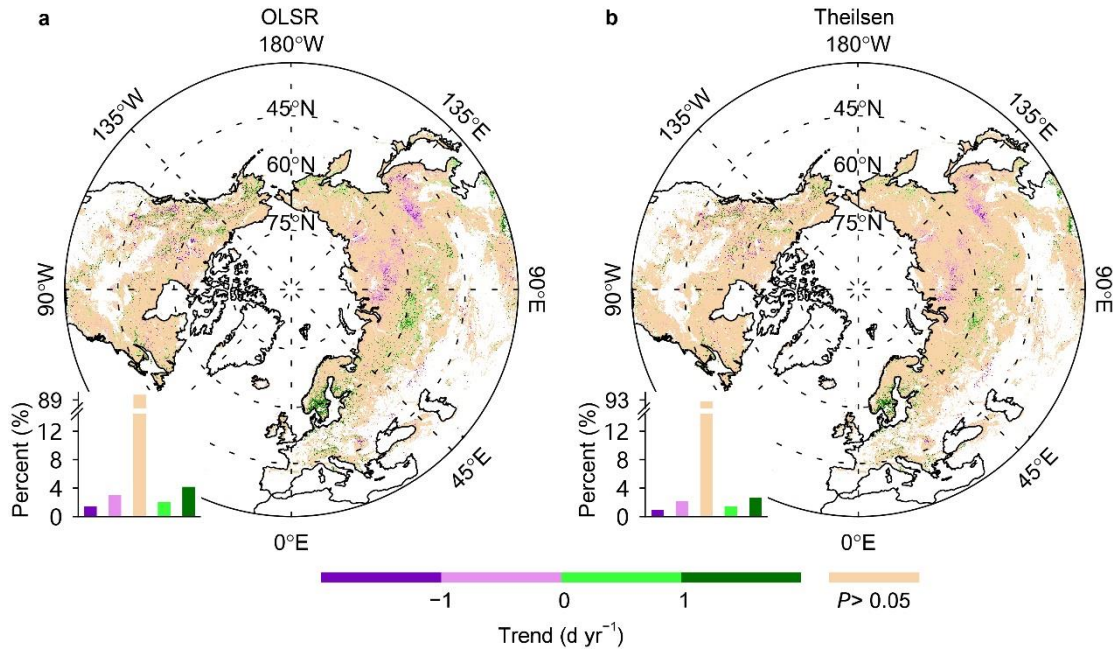
35
 36 **Figure S4.** Temporal trends in timing of the onset of leaf coloration (D_{LCO}), retrieved from satellite
 37 images over the period 2000–2018. The bar chart in each panel shows the percentage of area within each
 38 interval of the significant temporal trends and the percentage of area with nonsignificant trends,
 39 indicated by the color scale at the bottom. Positive and negative trend values refer to significantly
 40 delayed and advanced D_{LCO} , respectively. D_{LCO} in (a) corresponds to a 10% decrease in NDVI
 41 (Threshold). D_{LCO} in (b) and (c) was determined as the date of inflection point when NDVI began to
 42 decline (RCC). In (a) and (c), significant temporal trends were determined by using Mann-Kendall tests
 43 at $P < 0.05$ and a Theil-Sen estimator; in (b), significant temporal trends were determined by using t -
 44 tests at $P < 0.05$ and ordinary least squares regression (OLSR).

45



46
 47 **Figure S5.** Temporal trends in the timing of onset of leaf coloration (D_{LCO}), retrieved from satellite
 48 images for 2000–2018. The bar chart in each panel shows the percentage of area within each interval of
 49 the significant temporal trends and the percentage of area with nonsignificant trends, indicated by the
 50 color scale at the bottom. Positive and negative trend values refer to significantly delayed and advanced
 51 D_{LCO} , respectively. For the pixels identified as deciduous broadleaved forests, D_{LCO} was defined as the
 52 date when NDVI decreased by 10% of its annual amplitude from 1 August (see Section 2.4.4 for details).
 53 In (a), significant temporal trends were determined by using t -tests at $P < 0.05$ and ordinary least squares
 54 regression (OLSR). In (b), significant temporal trends were determined by using Mann-Kendall tests at
 55 $P < 0.05$ and a Theil-Sen estimator.

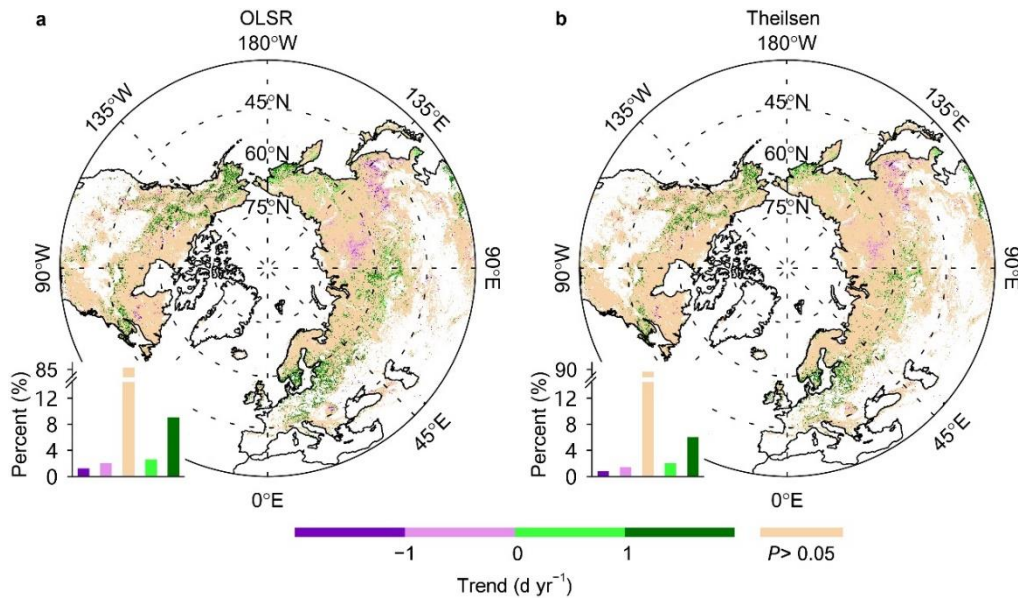
56



57

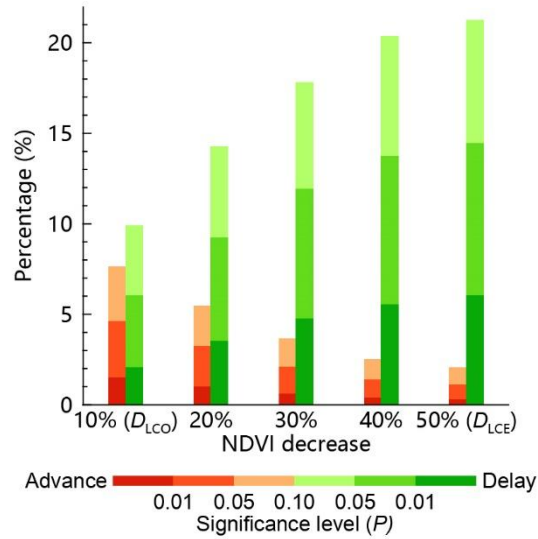
58 **Figure S6.** Temporal trends in the timing of onset of leaf coloration (D_{LCO}), as retrieved from satellite
 59 images for the period 2000–2018. The bar chart in each panel shows the percentage of area within each
 60 interval of the significant temporal trends and the percentage of area with nonsignificant trends,
 61 indicated by the color scale at the bottom. Positive and negative trend values refer to significantly
 62 delayed and advanced D_{LCO} , respectively. For the pixels identified as deciduous broadleaved forests,
 63 D_{LCO} was defined as the date when NDVI decreased by 10% of its annual amplitude from 16 August
 64 (see section 2.4.4 for details). In (a), significant temporal trends were determined by using t -tests at $P <$
 65 0.05 and ordinary least squares regression (OLSR). In (b), significant temporal trends were determined
 66 by using Mann-Kendall tests at $P <$ 0.05 and a Theil-Sen estimator.

67



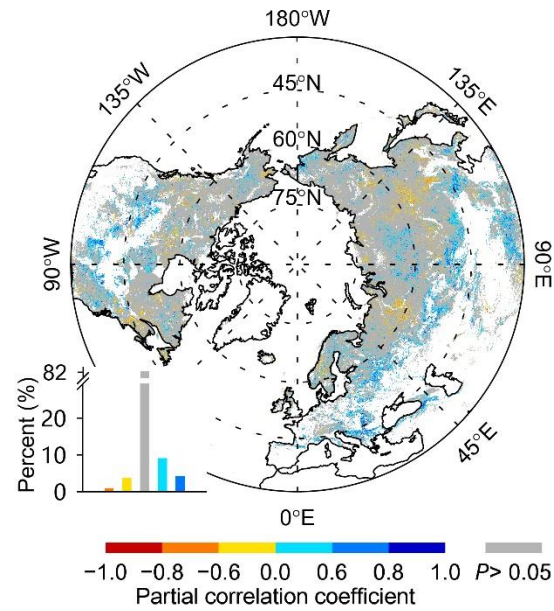
68
 69 **Figure S7.** Temporal trends in the timing of onset of leaf coloration (D_{LCO}), as retrieved from satellite
 70 images for 2000–2018. The bar chart in each panel shows the percentage of area within each interval of
 71 the significant temporal trends and the percentage of area with nonsignificant trends, indicated by the
 72 color scale at the bottom. Positive and negative trend values refer to significantly delayed and advanced
 73 D_{LCO} , respectively. D_{LCO} was determined as the date of inflection point when NDVI began to drop. For
 74 the pixels identified as deciduous broadleaved forests, the fitting function was a modified double logistic
 75 function that considered summer NDVI green-down. In (a), significant temporal trends were determined
 76 by using t -tests at $P < 0.05$ and ordinary least squares regression (OLSR). In (b), significant temporal
 77 trends were determined by using Mann-Kendall tests at $P < 0.05$ and a Theil-Sen estimator.

78



79
 80 **Figure S8.** Percentage of area with significant temporal trends in the timing of different stages of leaf
 81 coloration, as retrieved from satellite images. Significance levels of the temporal trends were determined
 82 by using *t*-tests for ordinary least squares regression over the period 2000–2018 at middle and high
 83 northern latitudes (30°N–75°N). The timings of the different stages of leaf coloration were defined as
 84 the dates when NDVI decreased by 10% (i.e., D_{LCO}), 20%, 30%, 40%, or 50% (i.e., D_{LCE}) of its annual
 85 amplitude in autumn.

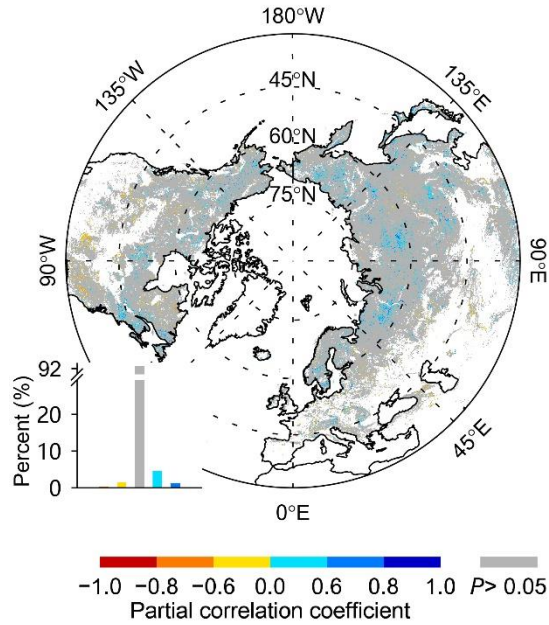
86



88

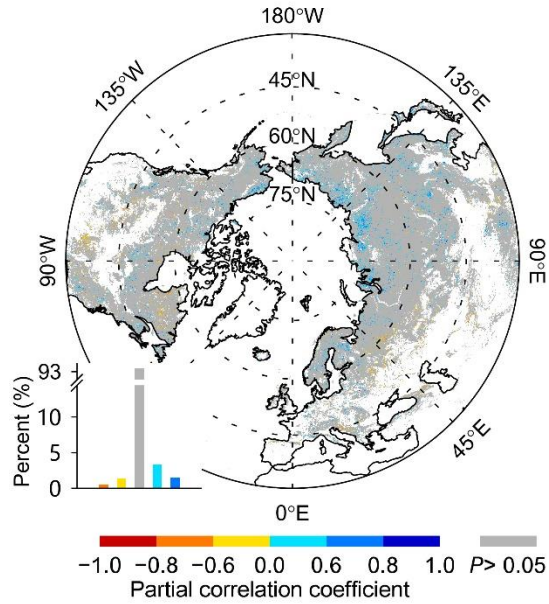
89 **Figure S9.** Spatial pattern of the partial correlation coefficient between the timing of onset of leaf
 90 coloration (D_{LCO}) and pre- D_{LCO} total precipitation over the period 2000–2018. The bar chart in the
 91 bottom-left corner shows the percentage of area for each interval of the partial correlation coefficient,
 92 with the coefficient values indicated by the color scale at the bottom.

93

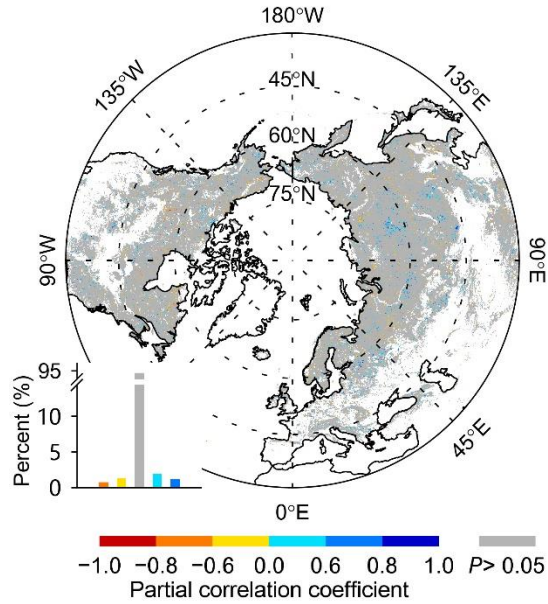


94
 95 **Figure S10.** Spatial pattern of the partial correlation coefficient between the timing of onset of leaf
 96 coloration (D_{LCO}) and pre- D_{LCO} (1 month preceding the multiyear mean D_{LCO}) mean daily minimum
 97 temperature over the period 2000–2018. The bar chart in each panel shows the percentage of area for
 98 each interval of the partial correlation coefficient, with the coefficient value indicated by the color scale
 99 at the bottom. Non-significant correlations ($P > 0.05$) are in gray.

100



101
 102 **Figure S11.** Spatial pattern of the partial correlation coefficient between the timing of onset of leaf
 103 coloration (D_{LCO}) and pre- D_{LCO} (15 days preceding the multiyear mean D_{LCO}) mean daily minimum
 104 temperature while controlling for the corresponding total precipitation over the period 2000–2016. The
 105 bar chart shows the percentage of area for each interval of partial correlation coefficient, with the
 106 coefficient value indicated by the color scale at the bottom. Non-significant correlations ($P > 0.05$) are in
 107 gray.
 108

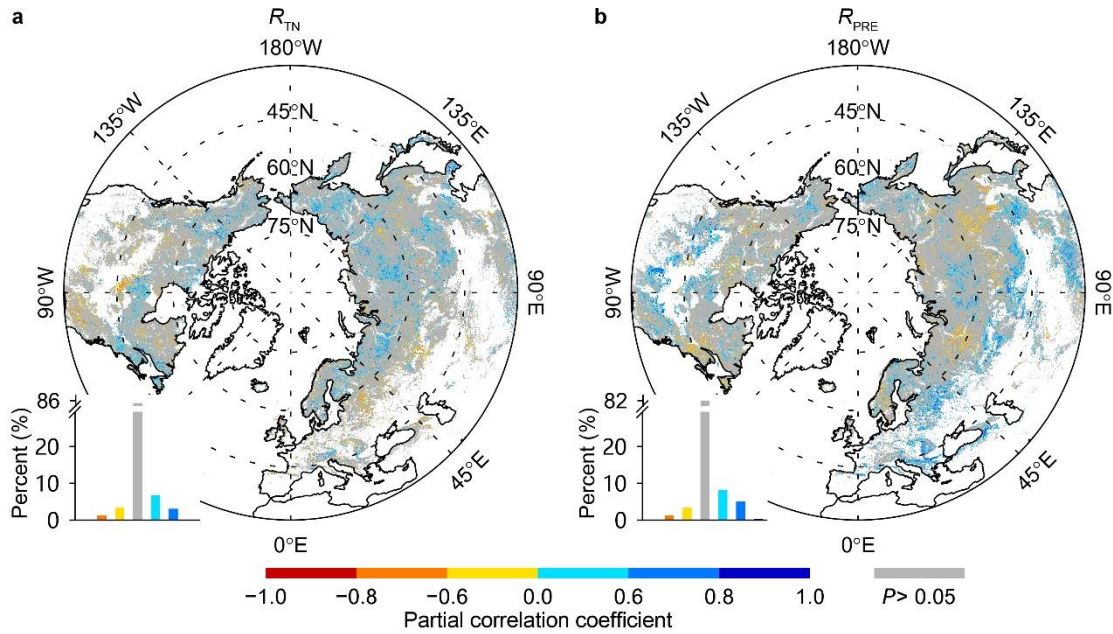


109

110 **Figure S12.** Spatial pattern of the partial correlation coefficient between the timing of the onset of leaf
 111 coloration (D_{LCO}) and the lowest daily minimum temperature (T_{min}) during the 15 days before the
 112 multiyear mean D_{LCO} , with the concurrent mean T_{min} and total precipitation as control variables over the
 113 period 2000–2016. The bar chart shows the percentage of area for each interval of the partial correlation
 114 coefficient ($P < 0.05$), with the coefficient indicated by the color scale at the bottom. Non-significant
 115 correlations ($P > 0.05$) are in gray.

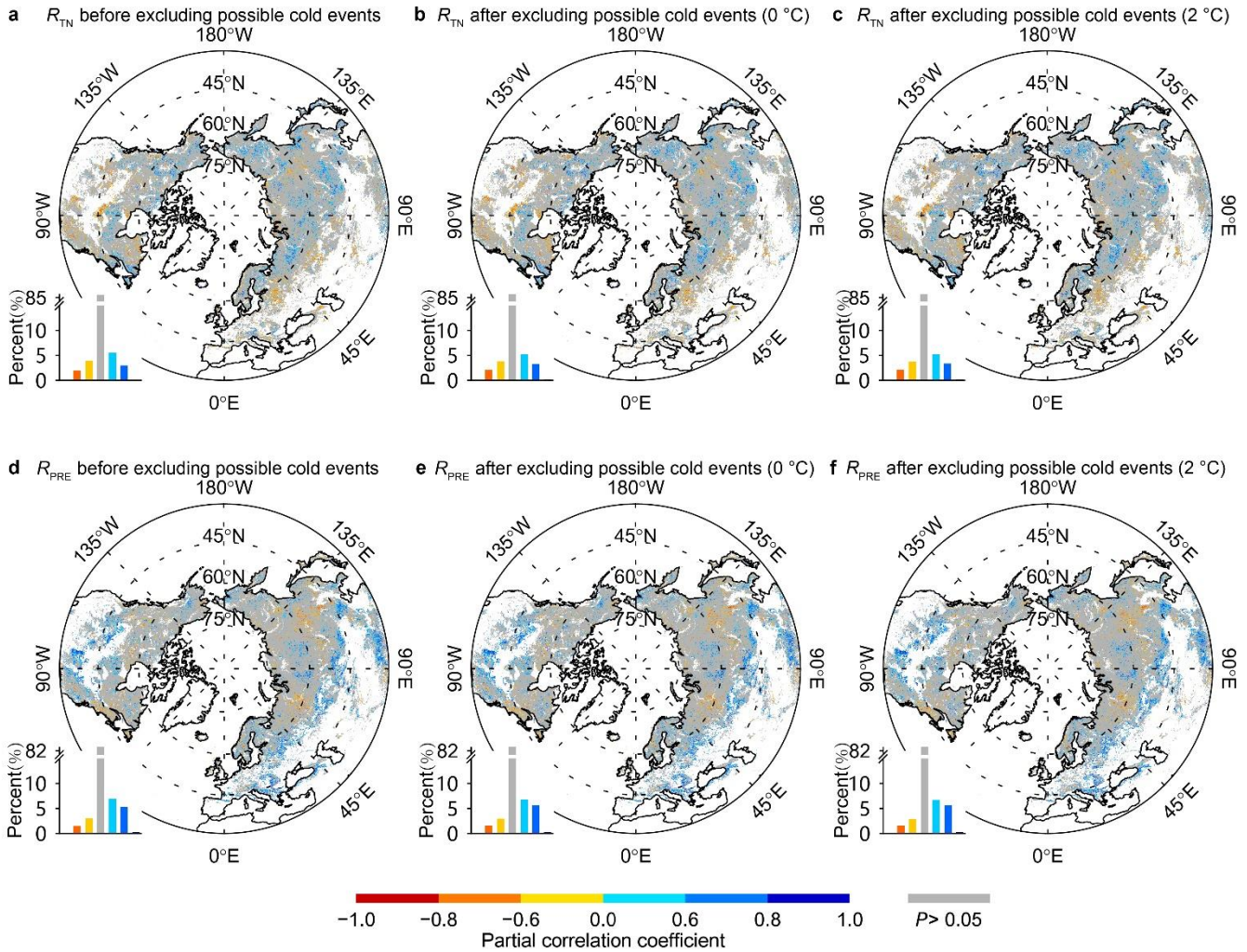
116

117



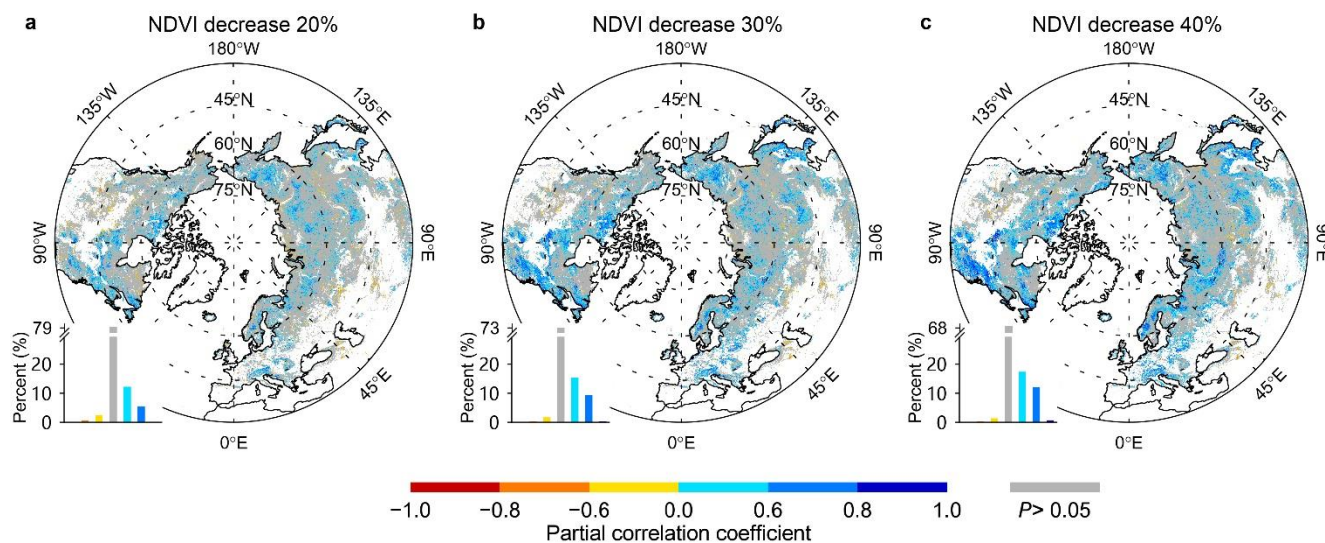
118
 119 **Figure S13.** Spatial pattern of the partial correlation coefficient between the timing of onset of leaf
 120 coloration (D_{LCO}) and pre- D_{LCO} climatic factors, with green-up onset date as an extra control variable
 121 over the period 2000–2018. a, Spatial pattern of the partial correlation coefficient (R_{TN}) between D_{LCO}
 122 and pre- D_{LCO} mean daily minimum temperature (T_{min}) while controlling for the corresponding total
 123 precipitation and green-up onset date. b, Spatial pattern of the partial correlation coefficient (R_{PRE})
 124 between D_{LCO} and pre- D_{LCO} total precipitation while controlling for the corresponding T_{min} and green-up
 125 onset date. The bar chart in each panel shows the percentage of area for each interval of the partial
 126 correlation coefficient, with the coefficient value indicated by the color scale at the bottom. Non-
 127 significant correlations ($P > 0.05$) are in gray.

128



129
 130 **Figure S14.** Spatial pattern of the partial correlation coefficient between the timing of onset of leaf
 131 coloration ($DLCO$) and pre- $DLCO$ climatic factors over the period 2000–2016 before and after the
 132 exclusion of years with possible cold events before $DLCO$. a–c, Spatial pattern of the partial correlation
 133 coefficient (R_{TN}) between $DLCO$ and pre- $DLCO$ mean daily minimum temperature (T_{min}) before (a) and
 134 after (b and c) the exclusion of years with possible cold events. d–f, The same as (a–c), but for the
 135 partial correlation between $DLCO$ and pre- $DLCO$ total precipitation (R_{PRE}). The bar chart in each panel
 136 shows the percentage of area for each interval of the partial correlation coefficient, with the coefficient
 137 value indicated by the color scale at the bottom. Non-significant correlations ($P > 0.05$) are in gray, and
 138 the percentage for each interval is provided in Table S6. Possible cold events were determined mainly
 139 by using a threshold-based method with a daily minimum temperature of 0 °C (b and e) or 2 °C (c and f).

140



142

143

144

145

146

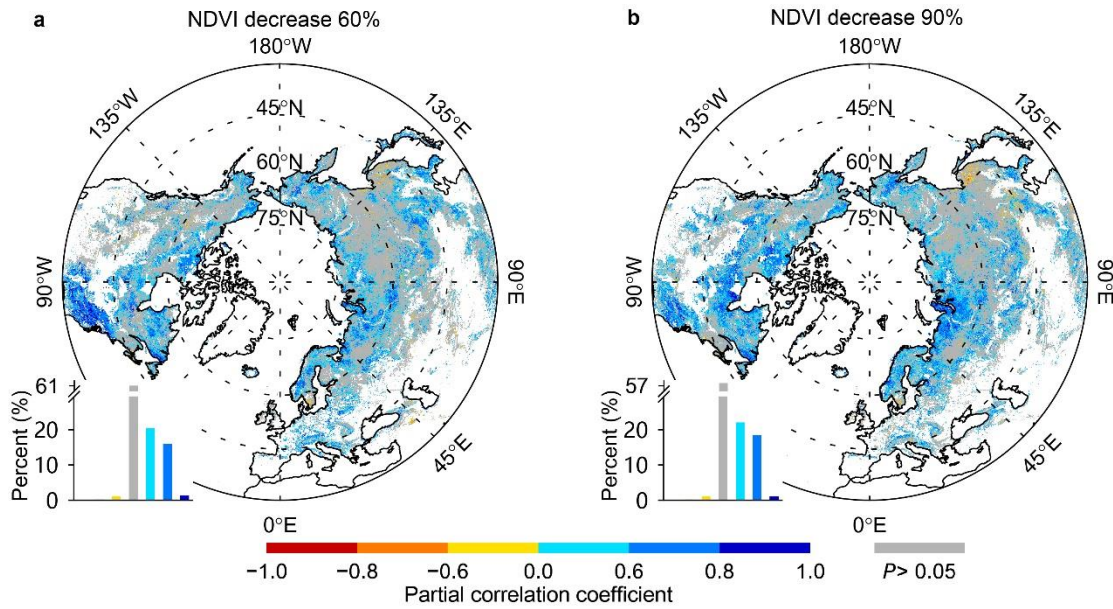
147

148

149

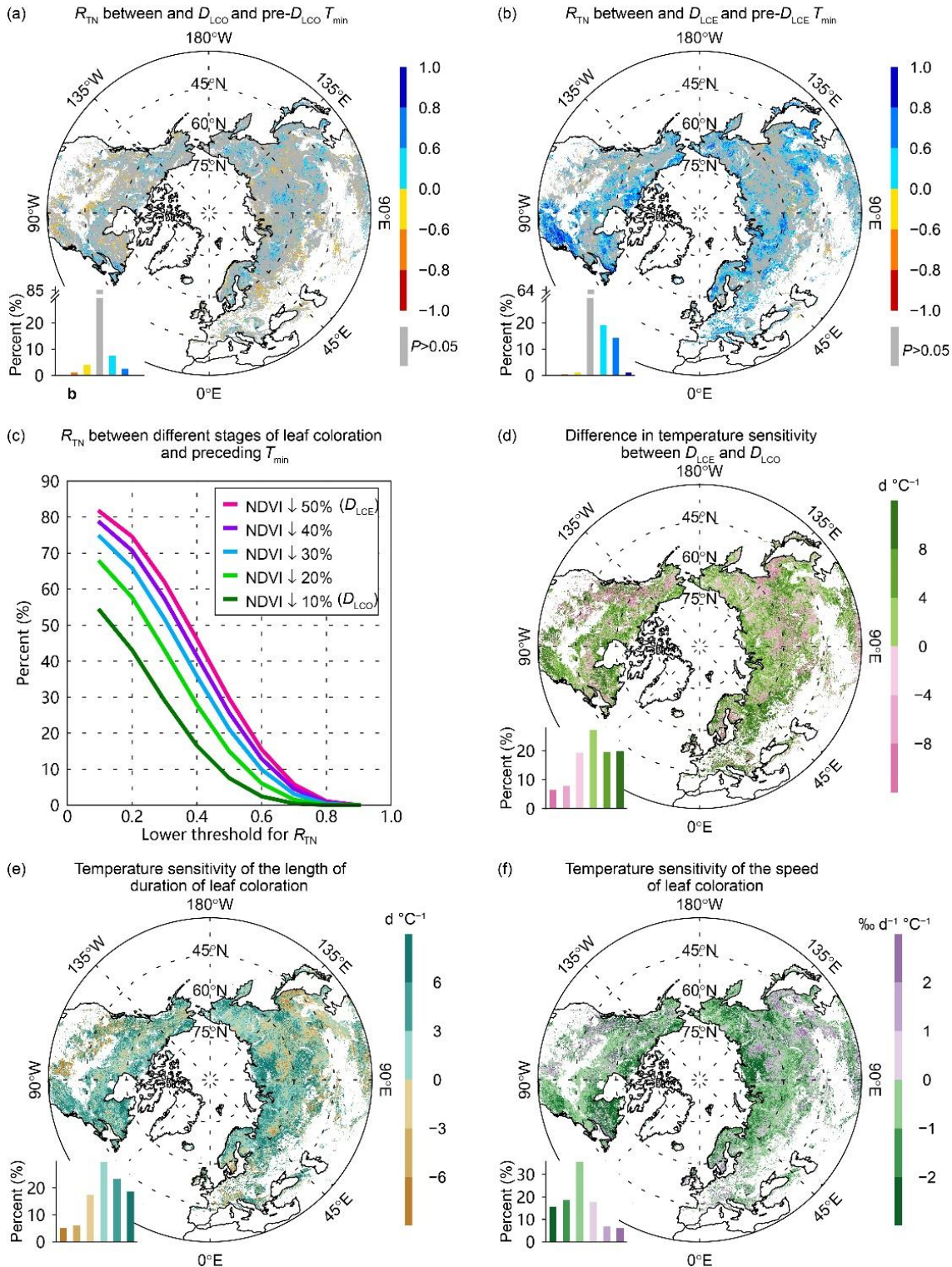
150

Figure S15. Spatial pattern of the partial correlation coefficient between the timing of different stages of leaf coloration and the mean daily minimum temperature for an optimized period preceding each stage for 2000–2018. The timings of different stages of leaf coloration are determined as the first dates when NDVI decreased by 20% (a), 30% (b), or 40% (c) of its annual amplitude in autumn. The bar chart in each panel shows the percentage of area for each interval of the partial correlation coefficient, with the coefficient value indicated by the color scale at the bottom. Non-significant correlations ($P > 0.05$) are in gray.



151
 152 **Figure S16.** Spatial pattern of the partial correlation coefficient between the timing of the end of leaf
 153 coloration (D_{LCE}) and pre- D_{LCE} T_{min} over the period 2000–2018. D_{LCE} was determined as the date when
 154 NDVI drops by 60% (a) and 90% (b), respectively. The bar chart in the bottom-left corner shows the
 155 percentage of area for each interval of the partial correlation coefficient, with the coefficient values
 156 indicated by the color scale at the bottom. Non-significant correlations ($P > 0.05$) are in gray.

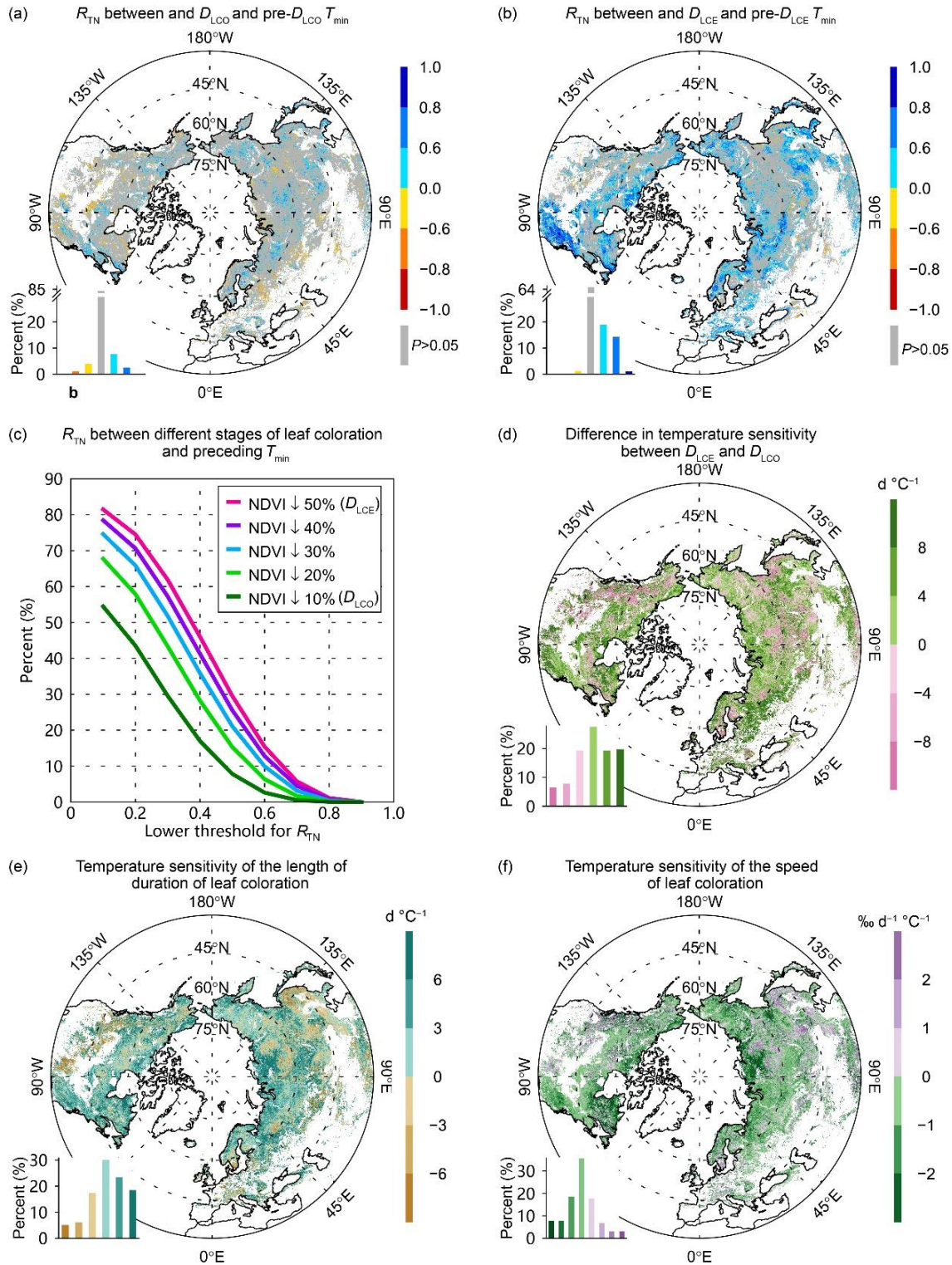
157
 158



159
 160 **Figure S17.** Impacts of temperature on the timing of different stages of leaf coloration and on the
 161 progress of leaf coloration over the period 2000–2018. (a) Spatial pattern of the partial correlation
 162 coefficient (R_{TN}) between D_{LCO} and pre- D_{LCO} mean daily minimum temperature (T_{min}). (b) Spatial
 163 pattern of R_{TN} between timing of the end of leaf coloration (D_{LCE}) and pre- $D_{LCE} T_{min}$. For pixels

164 identified as deciduous broadleaved forests, D_{LCO} and D_{LCE} were defined as the dates when NDVI
165 decreased by 10% and 50%, respectively, of their annual amplitude from 1 August (see section 2.4.4 for
166 details). The bar charts in (a) and (b) show the percentage of area for each interval of the partial
167 correlation coefficient ($P < 0.05$), with the coefficient indicated by the color scale on the right. Non-
168 significant correlations ($P > 0.05$) are in gray. (c) Percentage of area for which R_{TN} between the timing
169 of a given stage of leaf coloration and preceding T_{min} is higher than a given threshold indicated by the
170 horizontal axis. For example, R_{TN} for the onset of leaf coloration is higher than 0.2 in about 40% of the
171 area. (d) Difference in temperature sensitivity between D_{LCE} and D_{LCO} . Positive values indicate that
172 D_{LCE} is more sensitive to temperature than D_{LCO} , whereas negative values indicate that D_{LCO} is more
173 sensitive to temperature than D_{LCE} . (e) Temperature sensitivity of the length of duration of leaf
174 coloration. Positive values indicate that warming extends the duration of leaf coloration, whereas
175 negative values indicate that warming shortens the leaf coloration duration. (f) Temperature sensitivity
176 of the speed of leaf coloration. Positive values indicate that warming increases the speed of leaf
177 coloration, whereas negative values indicate that warming reduces the speed of leaf coloration. The bar
178 charts in (d), (e) and (f) show the percentage of area for each interval of the temperature sensitivity
179 indicated by the color scale on the right.

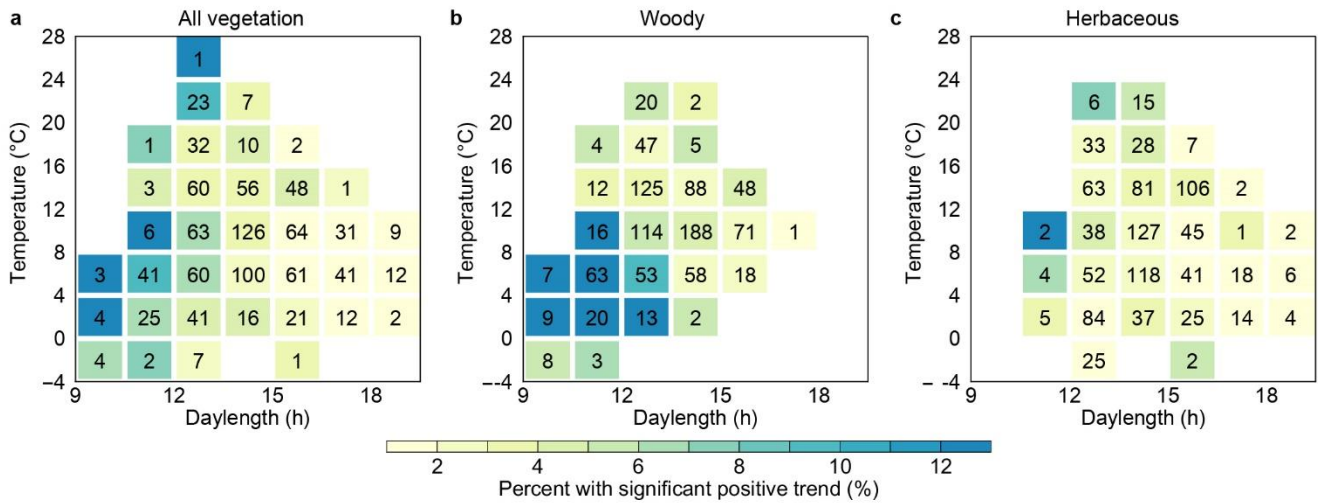
180



181
 182 **Figure S18.** Impacts of temperature on the timing of different stages of leaf coloration and on the
 183 progress of leaf coloration over the period 2000–2018. (a) Spatial pattern of the partial correlation
 184 coefficient (R_{TN}) between D_{LCO} and pre- D_{LCO} mean daily minimum temperature (T_{min}). (b) Spatial
 185 pattern of R_{TN} between timing of the end of leaf coloration (D_{LCE}) and pre- $D_{LCE} T_{min}$. For pixels

186 identified as deciduous broadleaved forests, D_{LCO} and D_{LCE} were defined as the dates when NDVI
187 decreased by 10% and 50%, respectively, of their annual amplitude from 16 August (see section 2.4.4
188 for details). The bar charts in (a) and (b) show the percentage of area for each interval of the partial
189 correlation coefficient ($P < 0.05$), with the coefficient indicated by the color scale on the right. Non-
190 significant correlations ($P > 0.05$) are in gray. (c) Percentage of area for which R_{TN} between the timing
191 of a given stage of leaf coloration and preceding T_{min} is higher than a given threshold indicated by the
192 horizontal axis. For example, R_{TN} for the onset of leaf coloration is higher than 0.2 in about 40% of the
193 area. (d) Difference in temperature sensitivity between D_{LCE} and D_{LCO} . Positive values indicate that
194 D_{LCE} is more sensitive to temperature than D_{LCO} , whereas negative values indicate that D_{LCO} is more
195 sensitive to temperature than D_{LCE} . (e) Temperature sensitivity of the length of duration of leaf
196 coloration. Positive values indicate that warming extends the duration of leaf coloration, whereas
197 negative values indicate that warming shortens the leaf coloration duration. (f) Temperature sensitivity
198 of the speed of leaf coloration. Positive values indicate that warming increases the speed of leaf
199 coloration, whereas negative values indicate that warming reduces the speed of leaf coloration. The bar
200 charts in (d), (e) and (f) show the percentage of area for each interval of the temperature sensitivity
201 indicated by the color scale on the right.

202



204

205

206

207

208

209

210

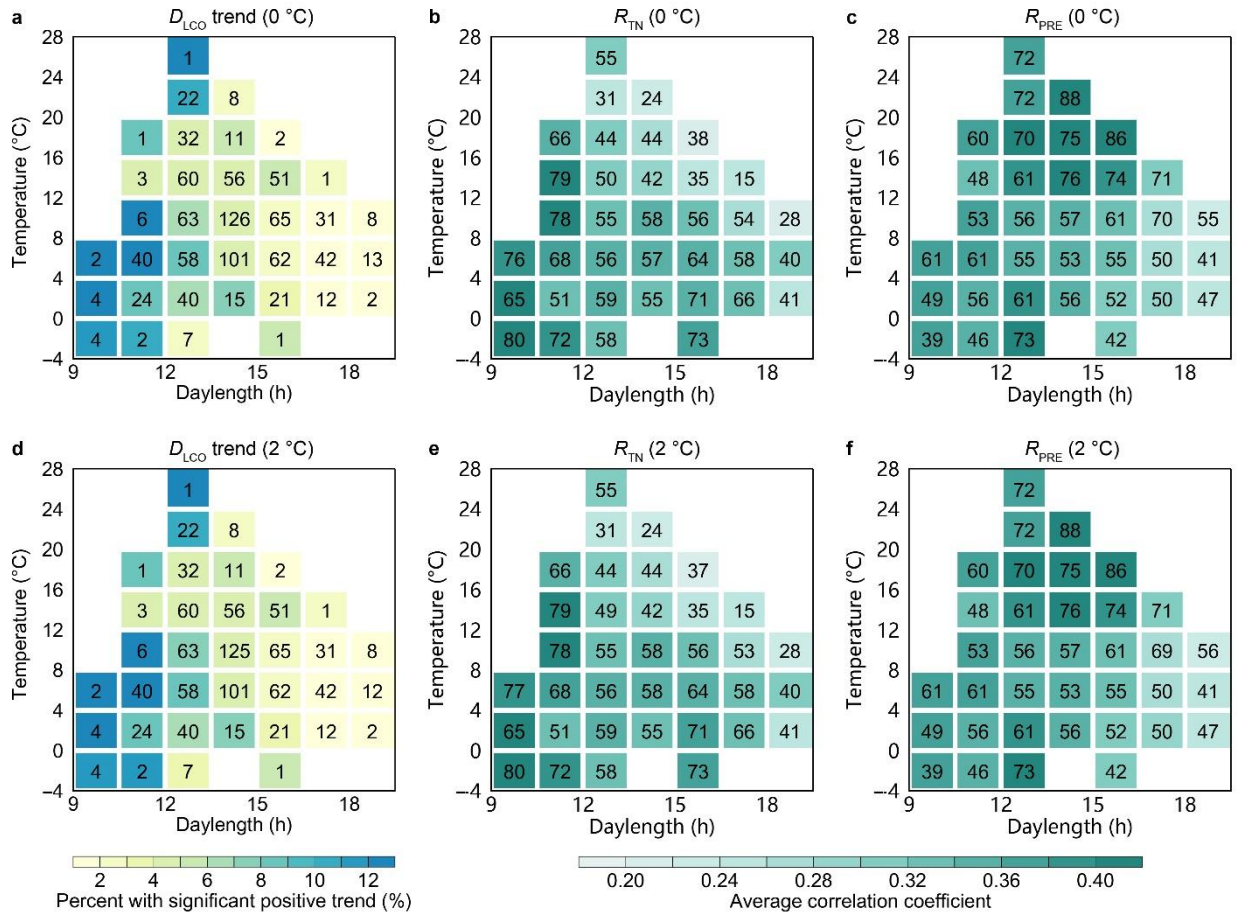
211

212

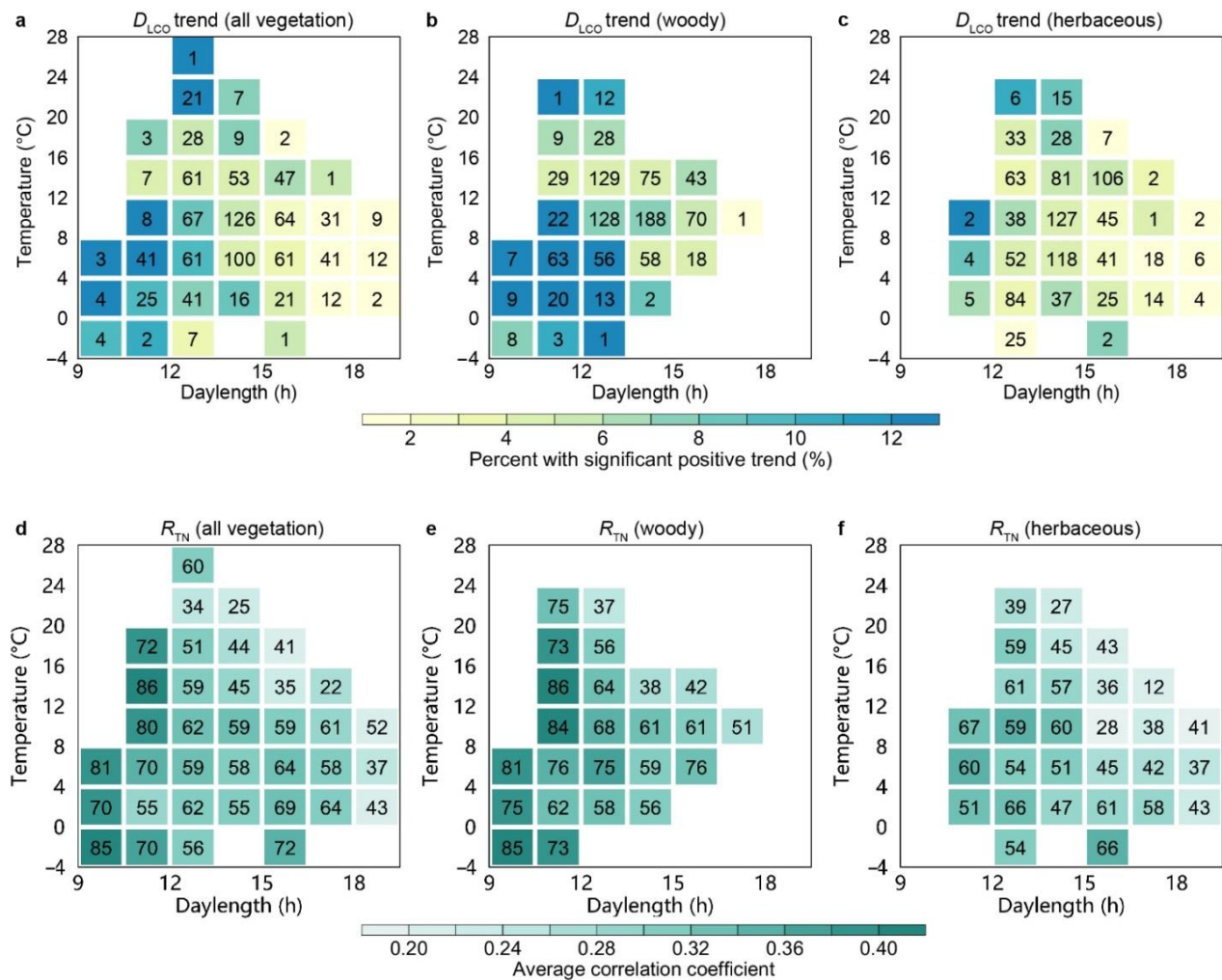
Figure S19. Dependence of temporal trends in the timing of onset of leaf coloration (D_{LCO}) on daylength and temperature at D_{LCO} over the period 2000–2018 for all (a), woody (b), and herbaceous (c) vegetation. a, Color indicates the percentage of area with significant ($P < 0.05$) D_{LCO} delays in each cell (i.e., a specific temperature \times daylength combination), as indicated by the color scale at the bottom. The number in each cell indicates the ratio (unit: %) of the area in each cell to the total area with D_{LCO} retrieval. Temporal trends and their significances were determined by using the Theil-Sen estimator and Mann-Kendall tests. b and c, The same as (a), but for woody and herbaceous vegetation, respectively. Only cells where the ratio of the area of the cell to the total area is $>1\%$ are represented.

213

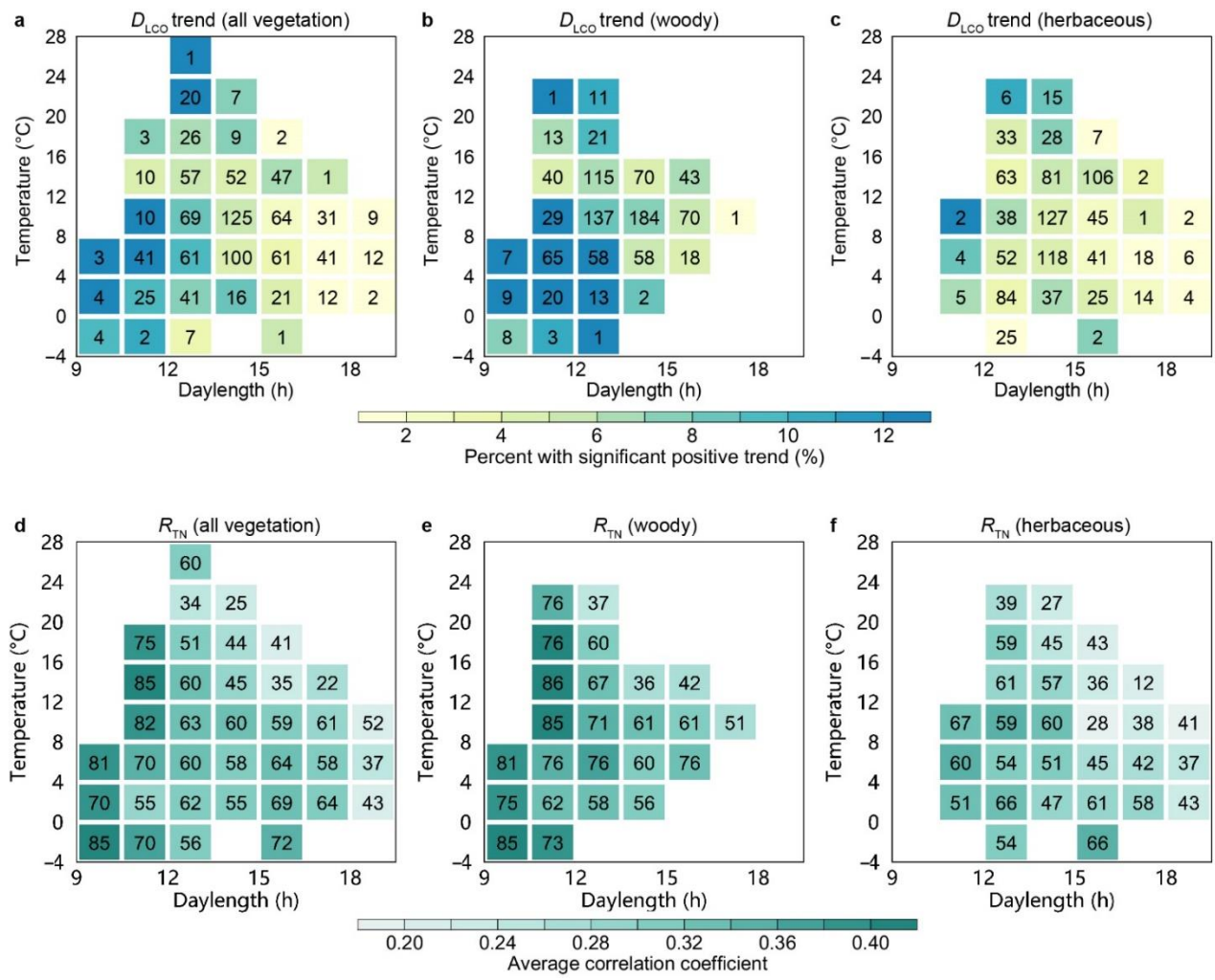
214



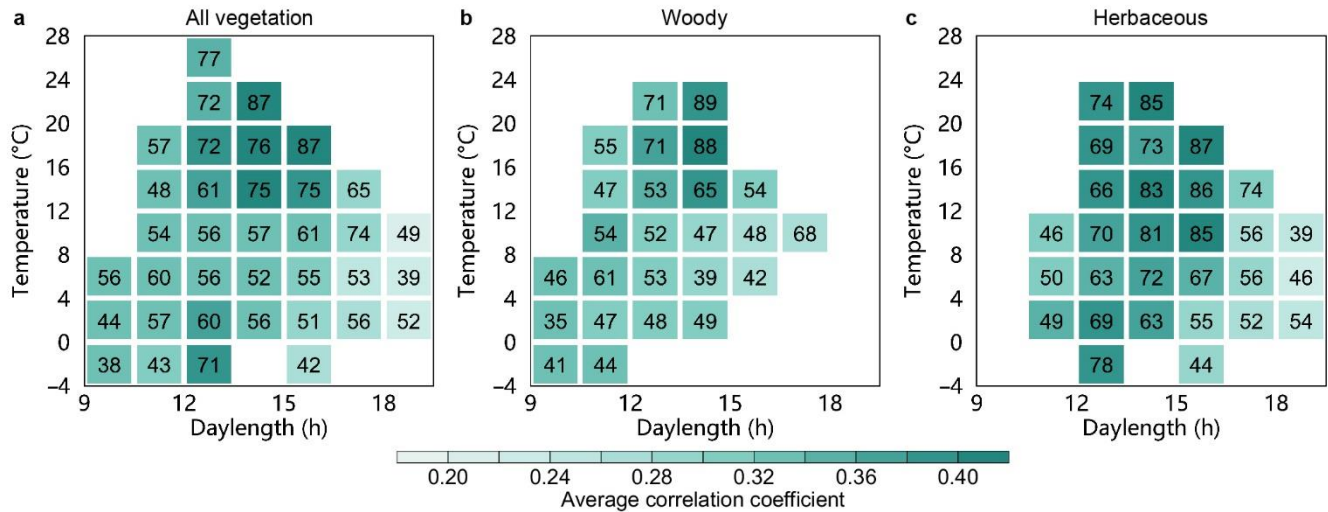
215
 216 **Figure S20.** Dependence of temporal trends in the timing of onset of leaf coloration (D_{LCO} , a and d), of
 217 the partial correlation coefficient (R_{TN} , b and e) between D_{LCO} and pre- D_{LCO} mean daily minimum
 218 temperature, and of the partial correlation coefficient (R_{PRE} , c and f) between D_{LCO} and pre- D_{LCO} total
 219 precipitation on daylength and temperature at D_{LCO} over the period 2000–2016 after the exclusion of
 220 years with possible cold events before D_{LCO} . Possible cold events were determined mainly by using a
 221 threshold-based method with a daily minimum temperature of 0 °C (a–c) or 2 °C (d–f). a and d, Color
 222 indicates the percentage of area with significant ($P < 0.05$) D_{LCO} delays in each cell (i.e., a specific
 223 temperature \times daylength combination), as indicated by the color scale at the bottom. The number in each
 224 cell indicates the ratio (unit: %) of the area in each cell to the total area with D_{LCO} retrieval. b and e,
 225 Color indicates the average of the positive R_{TN} , as indicated by the color scale at the bottom. The
 226 number indicates the percentage of area with a positive correlation in each cell. c and f, The same as (b
 227 and e), but for the positive R_{PRE} . Only cells where the ratio of the area of the cell to the total area is $>1\%$
 228 are represented.



229
 230 **Figure S21.** Dependence of temporal trends in the timing of onset of leaf coloration (D_{LCO} , a–c) and of
 231 the partial correlation coefficient (R_{TN} , d–f) between D_{LCO} and pre- D_{LCO} mean daily minimum
 232 temperature (T_{min}) on daylength and temperature at D_{LCO} over the period 2000–2018. a, Color indicates
 233 the percentage of area with significant ($P < 0.05$) D_{LCO} delays in each cell (i.e., a specific temperature \times
 234 daylength combination), as indicated by the color scale at the bottom. The number in each cell indicates
 235 the ratio (unit: %) of the area in each cell to the total area with D_{LCO} retrieval. The temporal trends and
 236 their significances were determined by ordinary least squares regression and t -tests. b and c, The same as
 237 (a) but for woody and herbaceous vegetation, respectively. d, Color indicates the average of the positive
 238 R_{TN} . The number indicates the percentage of area with a positive correlation in each cell, as indicated by
 239 the color scale at the bottom. e and f, The same as (d) but for woody and herbaceous vegetation,
 240 respectively. For the pixels identified as deciduous broadleaved forests, D_{LCO} was defined as the date
 241 when NDVI decreased by 10% of its annual amplitude from 1 August (see Section 2.4.4 for details).
 242 Only cells where the ratio of the area of the cell to the total area is $>1\%$ are represented.



243
 244 **Figure S22.** Dependence of temporal trends in the timing of onset of leaf coloration (D_{LCO} , a–c) and of
 245 the partial correlation coefficient (R_{TN} , d–f) between D_{LCO} and pre- D_{LCO} mean daily minimum
 246 temperature (T_{min}) on daylength and temperature at D_{LCO} over the period 2000–2018. a, Color indicates
 247 the percentage of area with significant ($P < 0.05$) D_{LCO} delays in each cell (i.e., a specific temperature \times
 248 daylength combination), as indicated by the color scale at the bottom. The number in each cell indicates
 249 the ratio (unit: %) of the area in each cell to the total area with D_{LCO} retrieval. The temporal trends and
 250 their significances were determined by ordinary least squares regression and t -tests. b and c, The same as
 251 (a) but for woody and herbaceous vegetation, respectively. d, Color indicates the average of the positive
 252 R_{TN} , as indicated by the color scale at the bottom. The number indicates the percentage of area with a
 253 positive correlation in each cell. e and f, The same as (d) but for woody and herbaceous vegetation,
 254 respectively. For the pixels identified as deciduous broadleaved forests, D_{LCO} was defined as the date
 255 when NDVI decreased by 10% of its annual amplitude from 16 August (see Section 2.4.4 for details).
 256 Only cells where the ratio of the area of the cell to the total area is $>1\%$ are represented.



257
 258 **Figure S23.** Dependence of the partial correlation coefficient (R_{PRE}) between the timing of onset of leaf
 259 coloration (D_{LCO}) and pre- D_{LCO} total precipitation on daylength and temperature at D_{LCO} over the period
 260 2000–2018 for all (a), woody (b), and herbaceous (c) vegetation. a, Color indicates the average of the
 261 positive R_{PRE} , as indicated by the color scale at the bottom. The number indicates the percentage of area
 262 with a positive correlation in each cell (i.e., a specific temperature \times daylength combination); b and c,
 263 The same as (a), but for woody and herbaceous vegetation, respectively. Only cells where the ratio of
 264 the area of the cell to the total area is $>1\%$ are represented.
 265

267
268 **Table S1.** Experiments on photoperiodic control of plant growth.

Species	Life-form	Findings from experiments	Experimental setting	Reference
<i>Acer rubrum</i> L.	Deciduous tree	Growth stopped after about four weeks of short photoperiod treatment (8 hours).	Chamber cultivating +controlled photoperiod	Downs and Borthwick (1956)
<i>Acer saccharum</i> Marsh.	Deciduous tree	Long photoperiod treatment (16 hours) resulted in delayed senescence and abscission for up to five months.	Chamber cultivating +controlled photoperiod	Olmsted (1951)
<i>Aesculus hippocastanum</i> L.	Deciduous tree	Growth stopped after about four weeks of short photoperiod treatment (8 hours).	Chamber cultivating +controlled photoperiod	Downs and Borthwick (1956)
<i>Betula mandshurica</i> [Regel] Nakai.	Deciduous tree	Growth stopped after about four weeks of short photoperiod treatment (8 hours).	Chamber cultivating +controlled photoperiod	Downs and Borthwick (1956)
<i>Betula pubescens</i> Ehrh.	Deciduous tree	Elongation growth ceased after 7–8 days of short photoperiod treatment (12 hours).	Chamber cultivating +controlled photoperiod	Rinne, Saarelainen, and Junttila (1994)
<i>Catalpa bignonioides</i> Walt.	Deciduous tree	Growth stopped after about four weeks of short photoperiod treatment (8 hours).	Chamber cultivating +controlled photoperiod	Downs and Borthwick (1956)
<i>Catalpa speciosa</i> Warder	Deciduous tree	Growth stopped after about four weeks of short photoperiod treatment (8 hours).	Chamber cultivating +controlled photoperiod	Downs and Borthwick (1956)
<i>Cornus florida</i> L.	Deciduous tree	Growth stopped after about four weeks of short photoperiod treatment (8 hours).	Chamber cultivating +controlled photoperiod	Downs and Borthwick (1956)
<i>Liquidambar styraciflua</i> L.	Deciduous tree	Growth stopped after about four weeks of short photoperiod treatment (8 hours).	Chamber cultivating +controlled photoperiod	Downs and Borthwick (1956)
<i>Liquidambar styraciflua</i> L.	Deciduous tree	The plant grew nearly all winter under a 16 hours photoperiod.	Chamber cultivating +controlled photoperiod	Kramer (1936)
<i>Liriodendron tulipifera</i> L.	Deciduous tree	Growth stopped after about ten days of short photoperiod treatment (8 hours).	Chamber cultivating +controlled photoperiod	Downs and Borthwick (1956)
<i>Liriodendron tulipifera</i> L.	Deciduous tree	The plant grew all winter under a 16 hours photoperiod.	Chamber cultivating +controlled photoperiod	Kramer (1936)
<i>Paulownia tomentosa</i> [Thunb.] Steud.	Deciduous tree	Growth stopped after about four weeks of short photoperiod treatment (8 hours).	Chamber cultivating +controlled photoperiod	Downs and Borthwick (1956)
<i>Populus trichocarpa</i> Torr. & Gray	Deciduous tree	Plant set bud after 18 days of short photoperiod treatment (13 hours), which is regulated by phytochrome.	Stem cutting + controlled photoperiod	Howe, Gardner GHackett, and Furnier (1996)

Species	Life-form	Findings from experiments	Experimental setting	Reference
<i>Populus tremula</i>	Deciduous tree	Shortening photoperiod was the main trigger for the initiation of autumn senescence.	Chamber cultivating +controlled photoperiod	Fracheboud et al. (2009)
<i>Populus tremula</i>	Deciduous tree	Photoperiod is the sole trigger for the onset of autumn senescence.	Observation under natural conditions	Keskitalo, Bergquist, Gardeström, and Jansson (2005)
<i>Populus tremula x tremuloides</i>	Deciduous tree	When plants are shifted from long days (16 hours) to short days (8 hours), they respond by growth cessation and bud set after 32 days.	Chamber cultivating +controlled photoperiod	Böhlenius et al. (2006)
<i>Ulmus americana</i> L.	Deciduous tree	Growth stopped after about twenty weeks of short photoperiod treatment (8 hours).	Chamber cultivating +controlled photoperiod	Downs and Borthwick (1956)
<i>Picea abies</i> (L.) Karst.	Evergreen tree	Growth cessation occurred within two weeks after exposure to short photoperiods (≤ 15 hours).	Chamber cultivating +controlled photoperiod	Heide (1974)
<i>Picea glauca</i> (Moench) Voss	Evergreen tree	Growth cessation occurred after five weeks of short photoperiod treatment (8 hours) under warm temperature conditions.	Chamber cultivating +controlled photoperiod	Hamilton et al. (2016)
<i>Pinus sylvestris</i> L.	Evergreen tree	Northern populations grown under 50°N photoperiod (shorter) stopped growth earlier than that under 60°N photoperiod (longer).	Chamber cultivating +controlled photoperiod	Oleksyn, Tjoelker, and Reich (1992)
<i>Pinus sylvestris</i> L.	Evergreen tree	Growth stopped after about four weeks of short photoperiod treatment (8 hours).	Chamber cultivating +controlled photoperiod	Downs and Borthwick (1956)
<i>Pinus taeda</i> L.	Evergreen tree	Growth stopped after about four weeks of short photoperiod treatment (8 hours).	Chamber cultivating +controlled photoperiod	Downs and Borthwick (1956)
<i>Pinus taeda</i> L.	Evergreen tree	The plant grew all winter with a 14.5 hours photoperiod.	Chamber cultivating +controlled photoperiod	Kramer (1936)
<i>Pinus virginiana</i> Mill.	Evergreen tree	Growth stopped after about four weeks of short photoperiod treatment (8 hours).	Chamber cultivating +controlled photoperiod	Downs and Borthwick (1956)
<i>Salix pentandra</i> L.	Deciduous small tree or shrub	Short photoperiod (≤ 22 hours for a northern ecotype and ≤ 15 hours for a southern ecotype) induced apical growth cessation.	Chamber cultivating +controlled photoperiod	Junttila (1980)
<i>Salix polaris</i> L.	Deciduous small tree or shrub	Leaf abscission in the arctic ecotype was stimulated by short photoperiod when grown at 15°C.	Collected with roots + controlled photoperiod	Paus, Nilsen, and Junttila (1986)

Species	Life-form	Findings from experiments	Experimental setting	Reference
<i>Syringa vulgaris</i> L.	Deciduous small tree or shrub	Photosynthetic efficiency has a more consistent relationship with photoperiod than with temperature.	Observation under natural conditions	Aikio, Taulavuori, Hurskainen, Taulavuori, and Tuomi (2019)
<i>Hibiscus rosa-sinensis</i> L.	Evergreen small tree or shrub	Leaves under long photoperiod treatment (16 hours) spend ten more days to complete senescence than that under short photoperiod treatment (8 hours).	Leaves cutting + controlled photoperiod	Misra and Biswal (1973)
<i>Hibiscus syriacus</i> L.	Deciduous shrub	Short photoperiod (8 hours) induced dormancy while long photoperiod (16 hours) delayed dormancy and resulted in considerable winter injury	Chamber cultivating +controlled photoperiod	Davidson (1957)
<i>Weigela florida</i> A. DC.	Deciduous shrub	Short photoperiod (8 hours) induced dormancy while long photoperiod (16 hours) delayed dormancy and resulted in considerable winter injury.	Chamber cultivating +controlled photoperiod	Davidson (1957)
<i>Rhododendron catawbiense</i> Michx.	Evergreen shrub	Short photoperiod (8 hours) induced dormancy while long photoperiod (16 hours) delayed dormancy and resulted in considerable winter injury.	Chamber cultivating +controlled photoperiod	Davidson (1957)
<i>Cucurbita pepo</i> Linn.	Herbaceous	After three months of growth, much larger percentage of mesophyll cell death was detected in short photoperiod (9 hours) than that in long photoperiod (18 hours).	Chamber cultivating +controlled photoperiod	Wang, Hu, Li, Cui, and Zhu (2002)
<i>Sedum telephium</i> L. subsp. <i>maximum</i> (L.) Krockner	Herbaceous	After eight weeks of growth, plants in long photoperiod (24 hours) elongated rapidly while those in short photoperiod (10 hours) became dormant.	Chamber cultivating +controlled photoperiod	Heide (2001)
<i>Vitis labruscana</i> Bailey	Herbaceous	Cane elongation was less in response to short photoperiod treatments (12 or 13 hours), as compared to natural photoperiod (13.7 or 14.3 hours).	Stem cutting + controlled photoperiod	Fennell and Hoover (1991)
<i>Vitis riparia</i> Michx.	Herbaceous	Cane elongation was less in response to short photoperiod treatments (12 or 13 hours), as compared to natural photoperiod (13.7 or 14.3 hours).	Stem cutting + controlled photoperiod	Fennell and Hoover (1991)

271 **Table S2.** *In situ* observations in China used in this study.

Site Name	Latitude	Longitude	Species number	Start year	End year	Year length
Nunkiang	49	125	5	1975±0	1993±4	17±4
Wudalianchi	48	126	11	1976±3	1995±3	18±3
Kiamusze	47	130	6	1981±1	1996±0	16±1
Minqin	38	103	29	1981±1	1996±1	12±1
Hohhot	41	112	10	1981±2	1996±1	13±2
Mutankiang	44	130	41	1980±2	1996±2	13±2
Beijing	40	116	42	1972±1	1994±3	20±4
Chengteh	41	118	5	1983±2	1996±0	12±1
Qinhuangdao	39	119	15	1980±0	1993±0	13±1
Gaizhou	40	122	12	1979±1	1996±0	17±1
Yixian	39	115	17	1980±0	1993±0	12±1
Liaocheng	36	115	5	1974±4	1993±2	15±3
Tyan	36	117	5	1974±0	1986±0	11±0
Sian	34	109	33	1977±3	1994±3	15±3
Luoyang	35	113	27	1977±4	1996±1	18±4
Yancheng	33	120	19	1981±4	1996±0	15±3
Zhengjiang	32	119	15	1976±3	1993±2	17±3
Hefei	32	117	19	1979±1	1995±1	17±2
Wuhu	31	118	16	1982±1	1996±0	13±1

272 The mean ± standard deviation of start year, end year and length of time series are provided for each site.

273

274 **Table S3.** FLUXNET2015 flux tower sites used in this study.

Fluxnet ID	Vegetation type	Latitude	Longitude	Year range	Reference
BE-Bra	Mixed Forests	51.31	4.52	1999-2002, 2004-2014	Janssens (2016)
BE-Vie	Mixed Forests	50.31	6.00	1996-2014	De Ligne, Manise, Heinesch, Aubinet, and Vincke (2016)
CA-Gro	Mixed Forests	48.22	-82.16	2003-2013	McCaughey (2016)
CA-Man	Evergreen Needleleaf Forest	55.88	-98.48	1994-2004, 2006-2008	Amiro (2016)
CA-Oas	Mixed Forests	53.63	-106.20	1996-2010	Black (2016a)
CA-Obs	Evergreen Needleleaf Forest	53.99	-105.12	1999-2010	Black (2016b)
CA-TP3	Mixed Forests	42.71	-80.35	2003-2014	Arain (2016a)
CA-TP4	Mixed Forests	42.71	-80.36	2002-2014	Arain (2016b)
CH-Dav	Evergreen Needleleaf Forest	46.82	9.86	1997-2014	Hörtnagl, Eugster, Merbold, et al. (2016)
CH-Lae	Mixed Forests	47.48	8.37	2004-2014	Hörtnagl, Eugster, Buchmann, et al. (2016)
CZ-BK1	Evergreen Needleleaf Forest	49.50	18.54	2004-2014	Šigut, Havrankova, Jocher, Pavelka, and Janouš (2016)
DE-Gri	Mixed Forests	50.95	13.51	2004-2014	Bernhofer et al. (2016a)
DE-Hai	Mixed Forests	51.08	10.45	2000-2012	Knohl et al. (2016)
DE-Tha	Evergreen Needleleaf Forest	50.96	13.57	1996-2014	Bernhofer et al. (2016b)
DK-Sor	Deciduous Broadleaf Forest	55.49	11.64	1996-2014	Ibrom and Pilegaard (2016)
DK-ZaH	Open Shrublands	74.47	-20.55	2000-2010, 2012-2014	Lund, Jackowicz-Korczynski, and Abermann (2016)
FI-Hyy	Evergreen Needleleaf Forest	61.85	24.30	1996-2014	Mammarella et al. (2016)
FI-Sod	Evergreen Needleleaf Forest	67.36	26.64	2001-2014	Aurela et al. (2016)
FR-Fon	Deciduous Broadleaf Forest	48.48	2.78	2005-2014	Berveiller et al. (2016)

Fluxnet ID	Vegetation type	Latitude	Longitude	Year range	Reference
IT-Col	Deciduous Broadleaf Forest	41.85	13.59	1997-2002, 2004-2014	Matteucci (2016)
IT-Lav	Evergreen Needleleaf Forest	45.96	11.28	2003-2014	Gianelle, Zampedri, Cavagna, and Sottocornola (2016)
IT-MBo	Grasslands	46.01	11.05	2003-2013	Gianelle, Cavagna, Zampedri, and Marcolla (2016)
IT-Ren	Evergreen Needleleaf Forest	46.59	11.43	1999, 2002-2003, 2005-2013	Minerbi and Montagnani (2016)
NL-Loo	Evergreen Needleleaf Forest	52.17	5.74	1996-2014	Moors and Elbers (2016)
RU-Cok	Open Shrublands	70.83	147.49	2003-2013	Dolman et al. (2016)
RU-Fyo	Mixed Forests	56.46	32.92	1998-2014	Varlagin, Kurbatova, and Vygodskaya (2016)
US-GLE	Evergreen Needleleaf Forest	41.36	-106.24	2005-2014	Massman (2016)
US-Ha1	Mixed Forests	42.54	-72.17	1992-2012	Munger (2016)
US-MMS	Deciduous Broadleaf Forest	39.32	-86.41	1999-2014	Novick and Phillips (2016)
US-Me2	Evergreen Needleleaf Forest	44.45	-121.56	2002-2014	Law (2016)
US-NR1	Evergreen Needleleaf Forest	40.03	-105.55	1999-2014	Blanken (2016)
US-Oho	Deciduous Broadleaf Forest	41.55	-83.84	2004-2013	Chen (2016)
US-PFa	Mixed Forests	45.95	-90.27	1996-2014	Desai (2016)
US-SRM	Open Shrublands	31.82	-110.87	2004-2014	Scott (2016a)
US-UMB	Deciduous Broadleaf Forest	45.56	-84.71	2000-2014	Gough, Bohrer, and Curtis (2016)
US-Wkg	Grasslands	31.74	-109.94	2004-2014	Scott (2016b)

276 **Table S4.** Percentage of time series for each interval of the temporal trend in D_{LCO} before and after the
 277 exclusion of years with cold events.

Metrics	Number of time-series	Cold events	Interval of significant temporal trend ($d\ y^{-1}$) ($P < 0.05$)				$P > 0.05$
			<-1	[-1, 0)	(0, 1]	>1	
Satellite D_{LCO} (2000–2016)	2.01×10^6	Not excluded	2	2	2	4	90
		Excluded (0 °C)	2	2	2	4	90
		Excluded (2 °C)	2	2	2	54	90
<i>in situ</i> D_{LCO} China	326	Not excluded	12	4	4	6	74
		Excluded (0 °C)	12	4	5	6	73
		Excluded (2 °C)	12	3	5	7	73

278 D_{LCO} , timing of onset of leaf coloration in autumn. Temporal trends were determined by using the ordinary least squares
 279 regression between D_{LCO} and the respective years, with t -tests. Only time series with at least 10 continuous years of data after
 280 exclusion of years with cold events were included. Cold events were determined mainly by using a threshold-based method
 281 with a daily minimum temperature of 0 °C or 2 °C. Data in the farthest right column indicate the percentage of area or time-
 282 series with a non-significant trend.
 283

284 **Table S5.** Percentage of time series for each interval of the temporal trend in D_{LCO} .

Metrics	Number of time-series	Interval of significant temporal trend ($d\ y^{-1}$) ($P < 0.05$)				$P > 0.05$
		<-1	$[-1, 0)$	$(0, 1]$	>1	
Satellite D_{LCO} (2000–2018)	2.07×10^6	1	2	1	3	93
<i>in situ</i> D_{LCO} China	332	8	2	3	3	84

285 D_{LCO} , timing of the onset of leaf coloration in autumn. Temporal trends were determined by using the Theil-Sen estimator
 286 between D_{LCO} and the respective years, with Mann-Kendall tests. Data in the farthest right column indicate the percentage of
 287 area or time-series with a non-significant trend.
 288

289 **Table S6.** Percentage of correlations between D_{LCO} or D_{PDO} and each climate factor for each interval of
 290 the partial correlation coefficient before and after the exclusion of years with cold events.

Metrics	Climatic Factor	Cold Events	Interval of the partial correlation coefficient ($P < 0.05$)						$P > 0.05$
			$[-1.0, -0.8)$	$[-0.8, -0.6)$	$[-0.6, 0)$	$(0, 0.6]$	$(0.6, 0.8]$	$(0.8, 1.0]$	
Satellite D_{LCO} (2000–2016)	Temperature	Not excluded	0	2	4	5	3	0	86
		Excluded (0 °C)	0	2	4	5	3	0	86
		Excluded (2 °C)	0	2	4	5	3	0	86
	Precipitation	Not excluded	0	2	3	7	5	0	83
		Excluded (0 °C)	0	2	3	7	5	0	83
		Excluded (2 °C)	0	2	3	7	5	0	83
<i>in situ</i> D_{LCO} China	Temperature	Not excluded	0	2	3	4	8	1	82
		Excluded (0 °C)	0	2	2	4	9	1	82
		Excluded (2 °C)	0	3	1	4	9	1	82
	Precipitation	Not excluded	0	3	3	4	5	0	85
		Excluded (0 °C)	0	3	3	3	6	0	85
		Excluded (2 °C)	0	3	3	3	6	0	85
FLUXNET2015 D_{PDO}	Temperature	Not excluded	0	5	3	0	3	0	89
		Excluded (0 °C)	0	5	3	0	0	0	92
		Excluded (2 °C)	0	5	3	0	0	0	92
	Precipitation	Not excluded	0	6	0	8	3	5	78
		Excluded (0 °C)	0	6	0	8	3	5	78
		Excluded (2 °C)	0	6	0	8	3	5	78

291 D_{PDO} , timing of onset of decrease in maximum canopy photosynthetic capacity in autumn; D_{LCO} , timing of onset of leaf
 292 coloration in autumn. Cold events were determined mainly by using a threshold-based method with a daily minimum
 293 temperature of 0 °C or 2 °C. Data in the farthest right column indicate the percentage of area or time-series with a non-
 294 significant correlation.
 295

296 **Table S7.** Percentage of correlations between D_{LCO} or D_{PDO} and each climate factor for each interval of
 297 the partial correlation coefficient.

Climatic factor	Metrics	Interval of the partial correlation coefficient ($P < 0.05$)						$P > 0.05$
		[-1.0, -0.8)	[-0.8, -0.6)	[-0.6, 0)	(0, 0.6]	(0.6, 0.8]	(0.8, 1.0]	
Temperature	FLUXNET2015 D_{PDO}	0	7	0	0	3	0	90
	Satellite D_{LCO}	0	4	3	3	3	0	87
Precipitation	FLUXNET2015 D_{PDO}	0	7	0	0	3	7	83
	Satellite D_{LCO}	0	0	0	0	7	0	93

298 D_{PDO} , timing of onset of decrease in maximum canopy photosynthetic capacity in autumn; D_{LCO} , timing of onset of leaf
 299 coloration in autumn. The relationships between D_{LCO} (or D_{PDO}) and temperature were determined by using a partial
 300 correlation analysis between D_{LCO} (or D_{PDO}) and pre- D_{LCO} (or pre- D_{PDO}) mean daily minimum temperature, with concurrent
 301 total precipitation as the control variable. The relationships between D_{LCO} (or D_{PDO}) and pre- D_{LCO} (or pre- D_{PDO}) precipitation
 302 were determined similarly. Only sites with at least 10 continuous years of valid data for both D_{LCO} and D_{PDO} were included.
 303 Data in the farthest right column indicate the percentage of area or time-series with a non-significant correlation. To make the
 304 satellite D_{LCO} and FLUXNET2015 D_{PDO} more comparable, MOD09A1 with a spatial resolution of 500 m was used for
 305 extracting satellite D_{LCO} .
 306

307 **Supplementary Methods**

308 **1 Preparation of high quality 5-day NDVI time series**

309 The quality of the daily surface reflectance data from MOD09CMG was unsatisfactory owing to
 310 cloud contamination (Vermote, 2015), so we used the 5-day maximum value composite approach
 311 (Zhang, 2015), combined with a Savitzky-Golay filter (Cao et al., 2018), to produce a high-quality
 312 NDVI time series before determining D_{LCO} . Details of the data preprocessing are given in the following
 313 text.

314 1) Calculating daily NDVI. We calculated the daily NDVI time series with the quality flag from
 315 surface reflectance in the red and near-infrared bands as $NDVI = (NIR - RED)/(NIR + RED)$. The
 316 quality flags for daily NDVI were derived from the two quality bands (i.e., Internal CM and State QA)
 317 of the reflectance product MOD09CMG (Vermote, Roger, & Ray, 2015). We determined four types of
 318 conditions that corresponded to the assigned quality flags: 1) clear, 2) uncertain, 3) snowy, and 4)
 319 cloudy (with deteriorating data quality), according to Cao et al. (2018) These were subsequently used in
 320 the Savitzky-Golay filtering (Cao et al., 2018). To be precise, the quality flag was set to “cloudy” if the
 321 cloud state in either Internal CM or State QA was labeled as “yes” or “cloudy or mixed”; the quality flag
 322 was set to “snowy” if the snow/ice flag in State QA was labeled as “yes”; and the quality flag was set to
 323 “uncertain” if the cloud state in State QA was not set (assumed clear). All the other data flags were set to
 324 “clear” (see the index table below). In addition, considering that the NDVI value of a vegetation pixel
 325 ranged from -0.2 to 1.0 , NDVI data outside this range were treated as gaps in the NDVI time series.

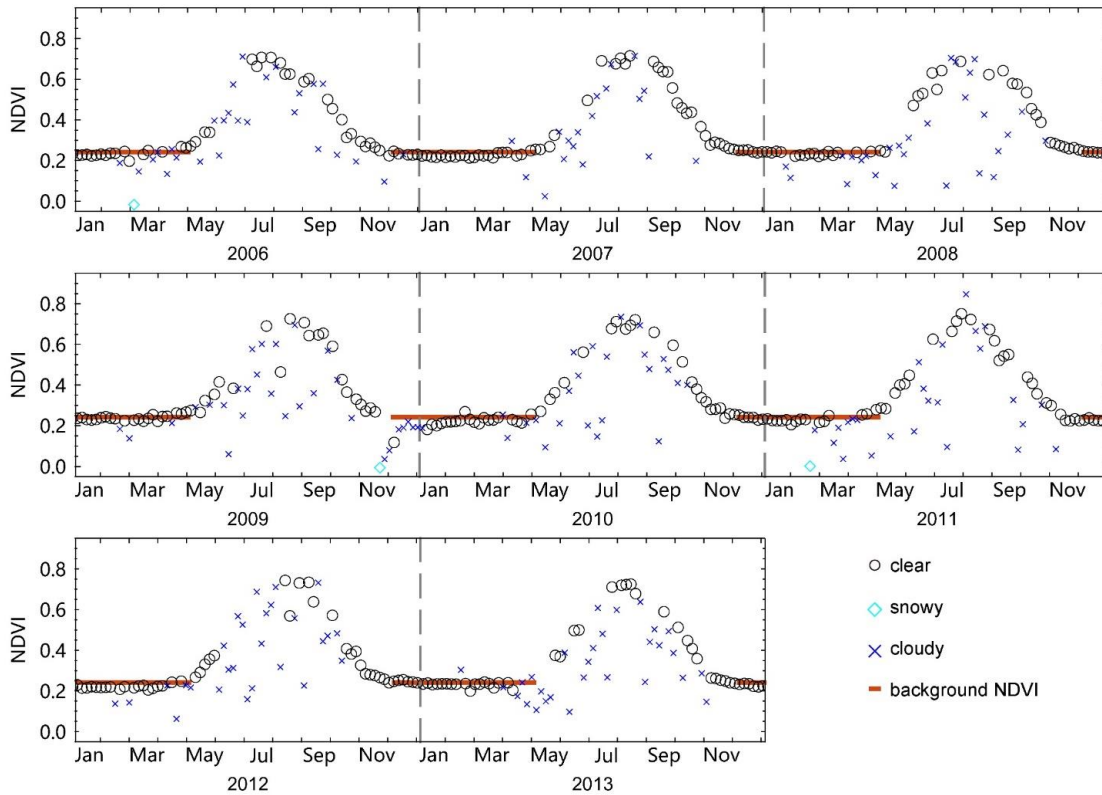
Quality flag of daily NDVI	MOD35 snow/ice flag in State QA	Cloud state in State QA	Cloud state in Internal CM
clear	no	clear	no
uncertain	no	not set (assumed clear)	no
snowy	yes	clear or not set (assumed clear)	no
cloudy	-	cloudy or mixed	-
	-	-	yes

326 “No” and “yes” in the snow/ice flag indicate absence and presence of snow or ice, respectively; “no” and “yes” in the internal
 327 CM indicate absence and presence of cloud, respectively; “-” means no specific snow/ice or cloud state was required.

328 2) Determining the background NDVI value for each pixel. The background value represents the
 329 annual minimum NDVI during winter (December–February), in which NDVI was expected to be stable
 330 for winter deciduous vegetation if there was no snow/ice or cloud contamination. The background NDVI
 331 value was calculated as the mean of high winter NDVI values, because snow/ice or cloud contamination

332 decreases NDVI owing to the uncertainties in the snow/ice and cloud flags (Beck, Atzberger, Høgda,
 333 Johansen, & Skidmore, 2006). To obtain high winter NDVI values for a given pixel, we first calculated
 334 a time series of winter NDVI higher than 0.10 (snow-contaminated NDVI is usually lower than 0.10).
 335 The high winter NDVI values were expected to be higher than the 50th percentile of this time series of
 336 winter NDVI and lower than the mean + 2SD of this time series of winter NDVI. In some cases, there
 337 would be no winter NDVI values higher than 0.10; for these cases the background NDVI value was set
 338 at 0.10.

339 3) Compositing the 5-day NDVI time series from daily NDVI time series. The daily NDVI time-
 340 series were aggregated to a 5-day composite as follows: if there were one or more NDVI values meeting
 341 the quality level (i.e., the quality flag is “clear” in step 1) within the 5-day period, the median value was
 342 used as the composite value to reduce noise, and the composite value was flagged as “clear”. If no
 343 acceptable NDVI data were found in the 5-day period, the maximum value was used as the composite value
 344 value (see Figure SM1), and the composite value was flagged as the corresponding daily quality flag of
 345 the maximum value.

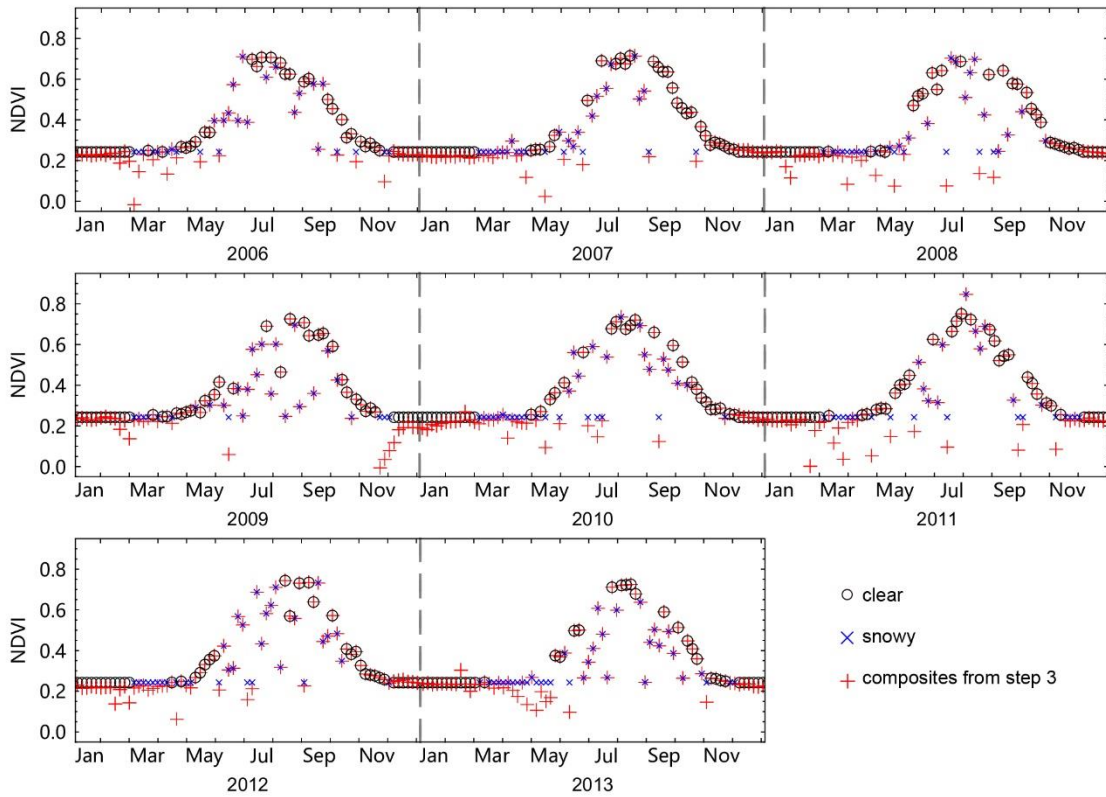


346

347 **Figure SM1.** An example (31.325°N, 98.125°E) showing composite 5-day NDVI time series from

348 daily NDVI time series.

349 4) Eliminating snow cover contamination in NDVI data. NDVI values in winter (December–
350 February) were all replaced by the background NDVI value, and their flag was set to “clear”, meaning
351 that those NDVI values were not changed in the Savitzky-Golay filtering. In the other three seasons
352 (March–November), the NDVI values lower than this background NDVI value were then substituted for
353 the latter one (see Figure SM2) and their flag values were set to “cloudy”.



354

355 **Figure SM2.** An example showing the elimination of snow cover contamination in NDVI data.

356

357 5) Identifying irregularly high and low NDVI values. Disturbances in surface reflectance data,
358 which are caused by cloud contamination, bidirectional effects, and data transmission errors, result in
359 irregularly high and low NDVI values. Most of these irregular NDVI values could be marked by using
360 the quality flag in step 1. However, because of the uncertainty of the quality flag, there was still a sharp
361 increase or sudden large decrease of NDVI values flagged as “clear” in the 5-day NDVI profile from
362 March to November. Because vegetation growth is a continuous process without large increases or
363 decreases in greenness over a few days, NDVI values that showed sharp decreases or increases were

364 defined as irregularly low or high NDVI values, respectively, and they were identified by using the
365 shape of the NDVI curve and an outlier detection method.

366 The irregularly low NDVI values were identified by using the shape of the NDVI curve.
367 Assuming that the 5-day NDVI increased or decreased gradually in a seasonal course, for any 5-day
368 NDVI at time t , denoted as $NDVI(t)$, an $NDVI(t)$ was identified as an irregularly low value, if there
369 existed two positive integers k and m satisfying

$$370 \quad NDVI(t) - NDVI(t - k) \leq -k \times (0.15 \times \max NDVI)$$

$$371 \quad NDVI(t) - NDVI(t + m) \leq -m \times (0.15 \times \max NDVI)$$

372 where $1 \leq k \leq 6$, $1 \leq m \leq 6$, and $\max NDVI$ was the 75th percentile of the time series of annual maximum
373 NDVI from 2000 to 2018. In a few cases, there may have been two consecutive irregularly low values,
374 which were identified as follows. Two consecutive NDVI values, $NDVI(t)$ and $NDVI(t + 1)$, were
375 identified as consecutive irregularly low values if they satisfied the following inequalities:

$$376 \quad NDVI(t) - NDVI(t - 1) \leq -1 \times (0.15 \times \max NDVI)$$

$$377 \quad NDVI(t + 1) - NDVI(t - 1) \leq -0.9 \times (0.15 \times \max NDVI)$$

$$378 \quad NDVI(t + 1) - NDVI(t + 2) \leq -2 \times (0.15 \times \max NDVI).$$

379 The irregularly high NDVI values were identified by using the shape of the NDVI curve and an
380 outlier detection method. The NDVI curve shape-based method included two procedures. Procedure 1
381 was to detect non-consecutive irregularly high NDVI values. Assuming that the 5-day NDVI increased
382 or decreased gradually in a seasonal course, an NDVI value at time t , $NDVI(t)$, was identified as an
383 irregularly high value if it satisfied

$$384 \quad NDVI(t) \geq 1.15 \times \max\{NDVI(t - 6), NDVI(t - 5), \dots, NDVI(k), \dots, NDVI(t + 6)\}$$

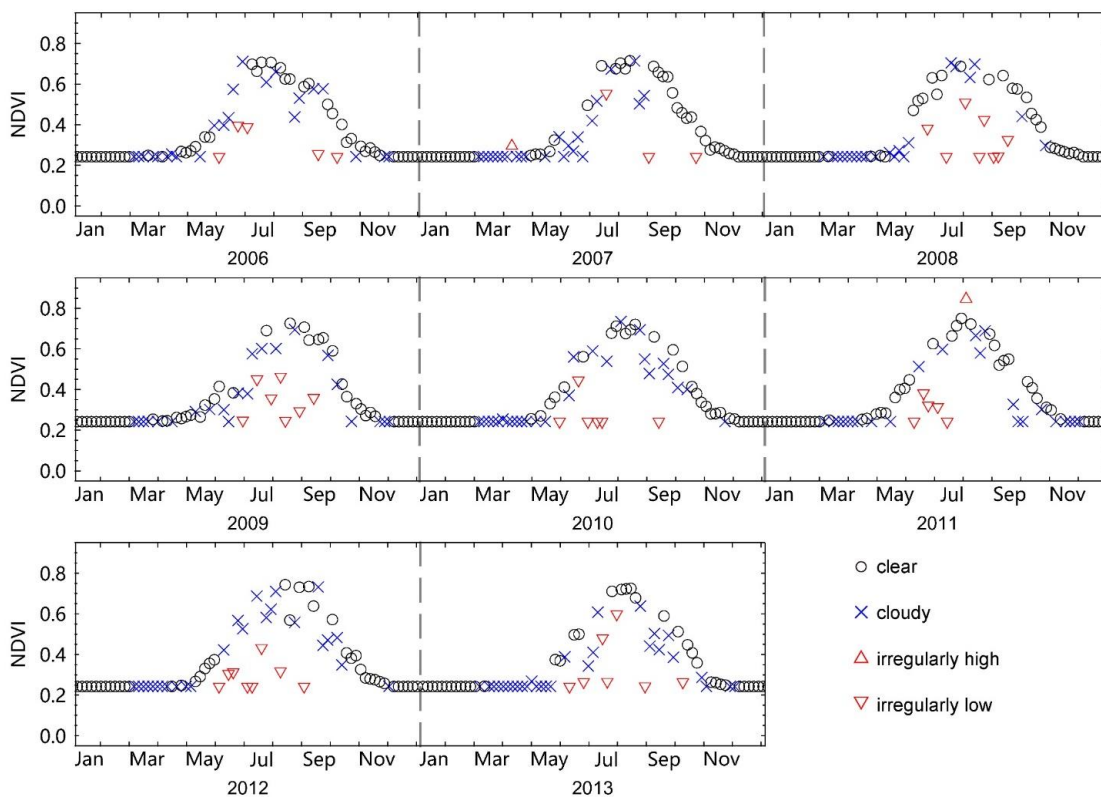
385 where $t - 6 \leq k \leq t + 6$ and $k \neq t$.

386 In some cases, there could be two or more irregularly high NDVI values within 1 month around
387 peak season that could not be detected by using the above algorithm. Such irregularly high NDVI values
388 were identified in Procedure 2, which used the information of a non-consecutive irregularly high NDVI
389 value identified in Procedure 1. We first constructed an array by selecting non-consecutive irregularly
390 high NDVI values in Procedure 1, which were the annual maximum values (denoted as $NDVI_{IHM}$). Then,
391 the NDVI values were identified as irregularly high NDVI values if they were 15% higher than the

392 median value of the array of $NDVI_{IHM}$.

393 Because the NDVI values around the peak season were essential for retrieving D_{LCO} , to be more
394 robust, the irregularly high NDVI values were also identified by using Grubb's test (Grubbs, 1950). We
395 first composed an array by using the three highest NDVI values of each year. The outliers in this array
396 were then detected by using Grubb's test at a significance level of $\alpha = 0.05$. Owing to inter-annual
397 variations in the annual maximum greenness, the outliers detected by Grubb's test may not necessarily
398 have been the irregularly high NDVI values. Therefore, in a given year, only outliers that were 15%
399 higher than the mean of the three highest non-outlier NDVI values for that year were identified as
400 irregularly high NDVI values. Finally, all the irregularly high NDVI values identified above were used
401 as irregularly high NDVI values.

402 The figure SM3 gives examples of irregularly low and high NDVI values.



403

404 **Figure SM3.** An example showing irregularly high and low NDVI values identified in the 5-day
405 composited NDVI time series.

406

407 6) Processing the NDVI values flagged as “cloudy”. Because clouds are overestimated by the

408 cloud flag (Wilson, Parmentier, & Jetz, 2014), there were a considerable number of high NDVI values
409 during March–November that were flagged as “cloudy” but that appeared to be reasonable in the
410 seasonal NDVI profile. We detected these NDVI values and promoted their flags to be “uncertain”
411 (“uncertain” indicates a quality higher than “cloudy” but lower than “clear”, see Cao et al. (2018) for
412 details). First, a pixel-year was excluded from our study if each of the NDVI values from May to
413 September was either “cloudy” or “irregular”. Second, for NDVI values lower than 90% of their annual
414 range plus the background NDVI value, the NDVI at time t , $NDVI(t)$, was flagged as “uncertain” if it
415 satisfied the following,

$$416 \quad NDVI(t) \geq \max\{NDVI(t - 2), NDVI(t - 1), NDVI(t), NDVI(t + 1), NDVI(t + 2)\},$$

417 where $NDVI(t)$ had been flagged as “cloudy”, and $NDVI(t-2)$, $NDVI(t-1)$, $NDVI(t+1)$, and $NDVI(t+2)$
418 had all been flagged as “cloudy” or “irregular”.

419 Moreover,

$$420 \quad NDVI(t) \geq 0.85 \times \max\{NDVI(t - 12), NDVI(t - 11), \dots, NDVI(t - 1)\}$$

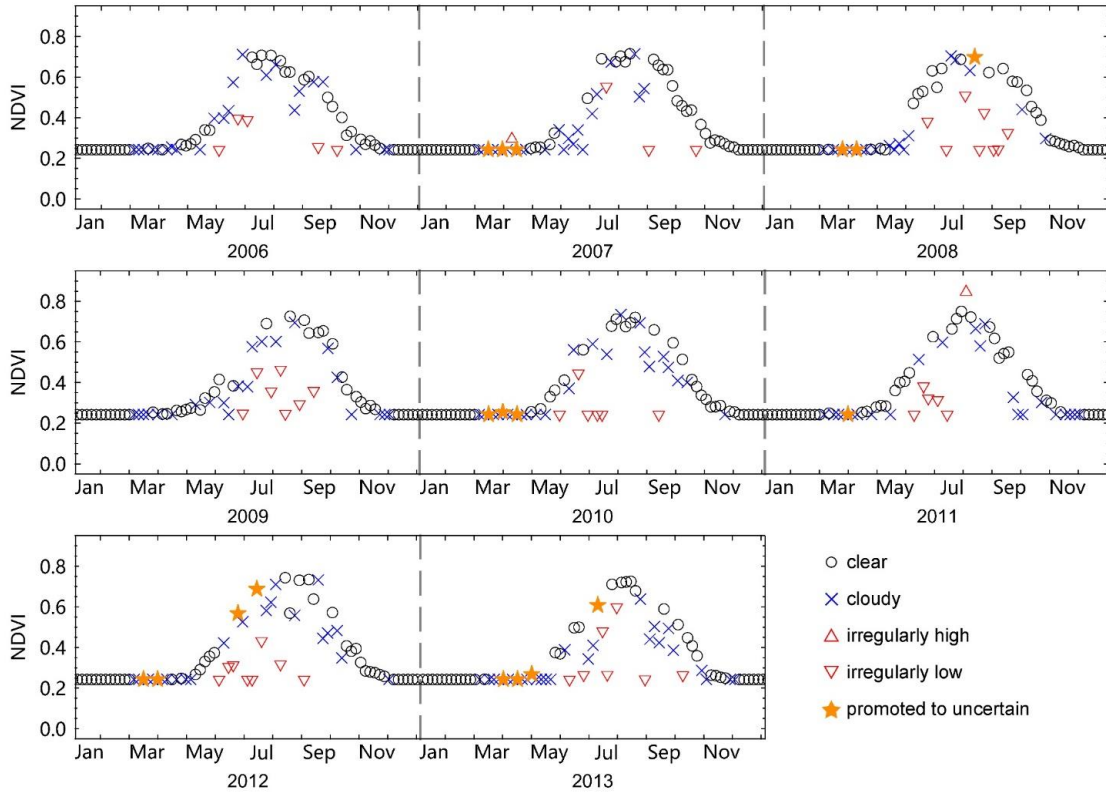
421 for $NDVI(t)$ in an ascending period (i.e., from early March to the time of annual maximum NDVI), and

$$422 \quad NDVI(t) \geq 0.85 \times \max\{NDVI(t + 1), NDVI(t + 2), \dots, NDVI(t + 12)\}$$

423 for $NDVI(t)$ in a descending period (i.e., from the time of annual maximum NDVI to late November).

424 The figure SM4 gives an example of NDVI values that were promoted from “cloudy” to “uncertain”.

425

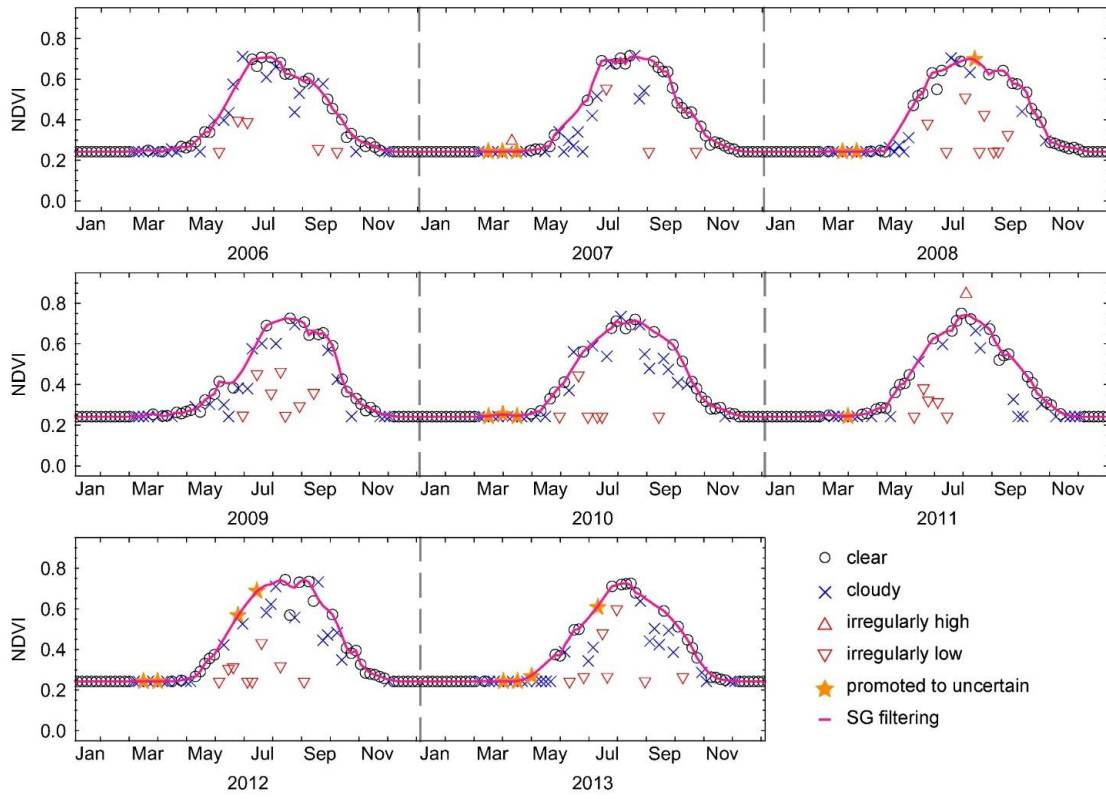


426

427 **Figure SM4.** An example showing NDVI values with flags promoted from “cloudy” to “uncertain”.

428

429 7) Reconstructing 5-day continuous high-quality NDVI time series. Because clouds and poor
 430 atmospheric conditions contaminate NDVI values, we applied a Savitzky-Golay filter to reconstruct a
 431 high-quality NDVI time-series as described by Cao et al. (2018) and Shen et al. (2014). The source code
 432 of Spatial-Temporal Savitzky-Golay (STSG) is available at [https://github.com/cao-](https://github.com/cao-sre/STSG_IDL_program)
 433 [sre/STSG_IDL_program](https://github.com/cao-sre/STSG_IDL_program) (assessed on 19 December 2018). Before we applied the filter, the “irregular”
 434 quality flags were merged to “cloudy”. In our study, we used the same parameter setting as Cao et al.
 435 (2018), except that the half width of the search window and the half width of the smoothing window
 436 were both set to 5. The figure SM5 gives an example of the filtering.



437

438 **Figure SM5.** An example showing the output of SG filtering.

439

440

441

442 **2 Comparison between satellite D_{LCO} and D_{LCO} from PhenoCam dataset**

443 To better match the PhenoCam images, we used the satellite MOD09A1 dataset (collection 6)
444 which has a spatial resolution of 500 m and temporal resolution of 8 days. The dataset was downloaded
445 from <https://modis.ornl.gov/globalsubset/> on March 10, 2021. The PhenoCam dataset V2.0 was
446 downloaded from https://daac.ornl.gov/cgi-bin/dsviewer.pl?ds_id=1674 on August 29, 2020. From the
447 high-frequency (typically, 30 minute) imagery collected over several years, the GCC (green chromatic
448 coordinate) time series of a region-of-interest (ROI) that delineates an area of specific vegetation type
449 was provided by the PhenoCam dataset. The VCI (vegetation contrast index) time series was calculated
450 as the ratio of the green to the sum of the red and blue bands (Zhang et al., 2018). For the comparison
451 between satellite D_{LCO} and D_{LCO} from the PhenoCam dataset, processing steps are as follows:

452 Step 1, the sites for agricultural lands, urban areas, or heterogeneous landscape within the area of
453 a 500 m \times 500 m pixel were excluded by visually examining the images in Google Earth. Then, daily
454 time series were created by calculating the 90th percentile of GCC or VCI for each day. After that, 5-day
455 medium value filtering was used to smooth the short term fluctuations and noises.

456 Step 2, a time series was excluded if there was no data in any consecutive 30 days from annual
457 maximum and to the end of year.

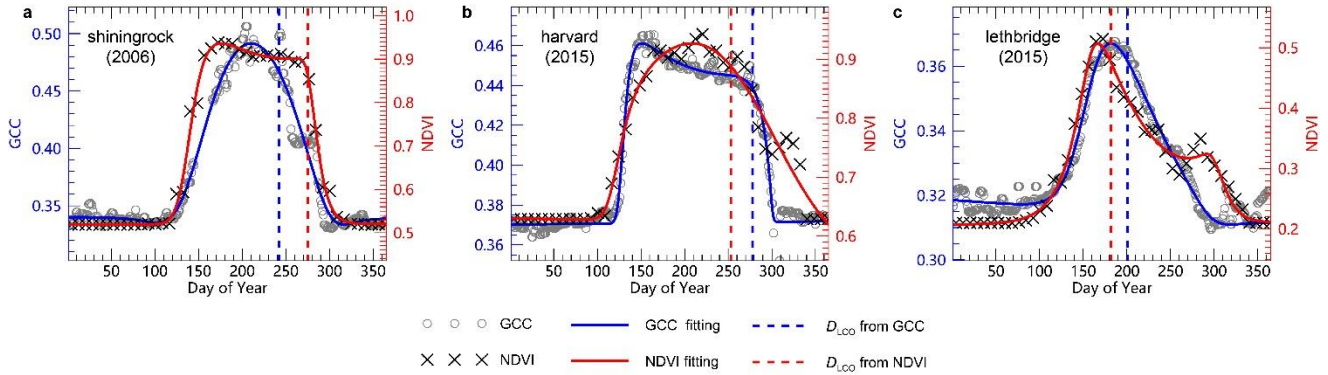
458 Step 3, the annual time series were fitted to a generalized sigmoid function (eq 7 in Klosterman et
459 al (Klosterman et al., 2014)).

460 Step 4, in many of the sites, there was considerable mismatch between the annual NDVI and GCC
461 (or VCI) trajectories. To remove some of those mismatched annual trajectories, we excluded the site-
462 years for which the date of annual maximum NDVI differed by more than 30 days from that of GCC (or
463 VCI) or the Pearson's correlation coefficient between NDVI and GCC (or VCI) lower than 0.75. In this
464 step, the date of annual maximum NDVI (or GCC, VCI) was determined using 25-day smoothed times
465 series of the fitted curves to eliminate short time variations. The Pearson's correlation coefficient was
466 calculated between fitted daily NDVI and GCC (or VCI) for the period from the date of annual
467 maximum greenness and the date when greenness dropped by 60%. The period for calculating
468 correlation coefficient was determined using the earlier one of the dates of annual maximum NDVI and
469 GCC (or VCI) and the later one of the dates when NDVI and GCC (or VCI) dropped by 60%. This
470 criterion was not applied to deciduous broadleaf forest, because annual maximum of GCC or VCI
471 usually occurred in late May or early June whereas annual maximum of NDVI was usually in late July
472 or early August. After that, we excluded the annual NDVI time series for which the mean NDVI of the

473 31 days period with annual maximum NDVI in the 16th day was less than 1.15 times the mean NDVI of
474 December.

475 The satellite D_{LCO} explained about 80% of the variations in PhenoCam derived D_{LCO} (Fig. 2 in the
476 main text), although the mismatch between the annual NDVI and GCC trajectories leads to large D_{LCO}
477 difference between NDVI and GCC (Figure SM6) or VCI (Figure SM7).

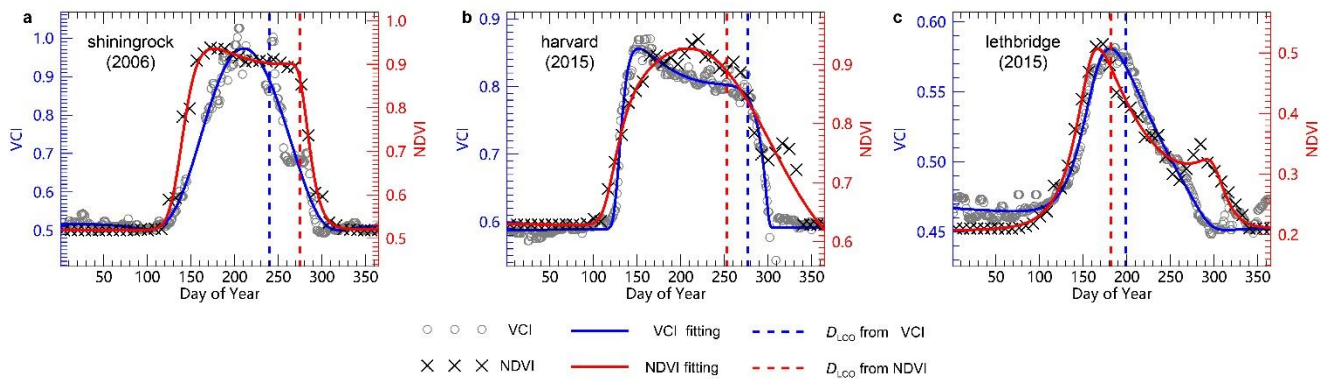
478



479

480 **Figure SM6.** Examples that mismatch between the annual NDVI and GCC trajectories leads to large
481 D_{LCO} difference between NDVI and GCC.

482



483

484 **Figure SM7.** Examples that mismatch between the annual NDVI and VCI trajectories leads to large
485 D_{LCO} difference between NDVI and VCI.

486

487

488 **Supplementary References**

- 489 Aikio, S., Taulavuori, K., Hurskainen, S., Taulavuori, E., & Tuomi, J. (2019). Contributions of day
490 length, temperature and individual variability on the rate and timing of leaf senescence in the
491 common lilac *Syringa vulgaris*. *Tree Physiology*, 39(6), 961-970. doi:10.1093/treephys/tpz013
- 492 Amiro, B. (2016). FLUXNET2015 CA-Man Manitoba - Northern Old Black Spruce (former BOREAS
493 Northern Study Area). In: FluxNet; University of Manitoba.
- 494 Arain, M. A. (2016a). FLUXNET2015 CA-TP3 Ontario - Turkey Point 1974 Plantation White Pine. In:
495 FluxNet; McMaster University.
- 496 Arain, M. A. (2016b). FLUXNET2015 CA-TP4 Ontario - Turkey Point 1939 Plantation White Pine. In:
497 FluxNet; McMaster University.
- 498 Aurela, M., Tuovinen, J.-P., Hatakka, J., Lohila, A., Mäkelä, T., Rainne, J., & Lauria, T. (2016).
499 FLUXNET2015 FI-Sod Sodankyla. In: FluxNet; Finnish Meteorological Institute.
- 500 Beck, P. S. A., Atzberger, C., Høgda, K. A., Johansen, B., & Skidmore, A. K. (2006). Improved
501 monitoring of vegetation dynamics at very high latitudes: A new method using MODIS NDVI.
502 *Remote Sensing of Environment*, 100(3), 321-334. doi:10.1016/j.rse.2005.10.021
- 503 Bernhofer, C., Grünwald, T., Moderow, U., Hehn, M., Eichelmann, U., & Prasse, H. (2016a).
504 FLUXNET2015 DE-Gri Grillenburg. In: FluxNet; TU Dresden.
- 505 Bernhofer, C., Grünwald, T., Moderow, U., Hehn, M., Eichelmann, U., & Prasse, H. (2016b).
506 FLUXNET2015 DE-Tha Tharandt. In: FluxNet; TU Dresden.
- 507 Berveiller, D., Delpierre, N., Dufrêne, E., Pontailleur, J.-Y., Vanbostal, L., Janvier, B., ... Cristinacce, K.
508 (2016). FLUXNET2015 FR-Fon Fontainebleau-Barbeau. In: FluxNet; CNRS.
- 509 Black, T. A. (2016a). FLUXNET2015 CA-Oas Saskatchewan - Western Boreal, Mature Aspen. In:
510 FluxNet; The University of British Columbia.
- 511 Black, T. A. (2016b). FLUXNET2015 CA-Obs Saskatchewan - Western Boreal, Mature Black Spruce.
512 In: FluxNet; The University of British Columbia.
- 513 Blanken, P. (2016). FLUXNET2015 US-NR1 Niwot Ridge Forest (LTER NWT1). In: FluxNet;
514 University of Colorado.
- 515 Böhlenius, H., Huang, T., Charbonnel-Campaa, L., Brunner, A. M., Jansson, S., Strauss, S. H., &
516 Nilsson, O. (2006). CO/FT regulatory module controls timing of flowering and seasonal growth
517 cessation in trees. *Science*, 312(5776), 1040-1043.
- 518 Cao, R., Chen, Y., Shen, M., Chen, J., Zhou, J., Wang, C., & Yang, W. (2018). A simple method to

519 improve the quality of NDVI time-series data by integrating spatiotemporal information with the
520 Savitzky-Golay filter. *Remote Sensing of Environment*, 217, 244-257.
521 doi:<https://doi.org/10.1016/j.rse.2018.08.022>

522 Chen, J. (2016). FLUXNET2015 US-Oho Oak Openings. In: FluxNet; University of Toledo / Michigan
523 State University.

524 Davidson, H. (1957). *Photoperiodic responses on selected woody ornamental shrubs*. Michigan State
525 University of Agriculture and Applied Science. Department of Horticulture,

526 De Ligne, A., Manise, T., Heinesch, B., Aubinet, M., & Vincke, C. (2016). FLUXNET2015 BE-Vie
527 Vielsalm. In: FluxNet; University of Liege - Gembloux Agro-Bio Tech; University catholic of
528 Louvain-la-Neuve.

529 Desai, A. (2016). FLUXNET2015 US-PFa Park Falls/WLEF. In: FluxNet; University of Wisconsin.

530 Dolman, H., Van Der Molen, M., Parmentier, F.-J., Marchesini, L. B., Dean, J., Van Huissteden, K., &
531 Maximov, T. (2016). FLUXNET2015 RU-Cok Chokurdakh. In: FluxNet; Vrije Universiteit
532 Amsterdam.

533 Downs, R. J., & Borthwick, H. A. (1956). Effects of photoperiod on growth of trees. *Botanical Gazette*,
534 117(4), 310-326.

535 Fennell, A., & Hoover, E. (1991). Photoperiod influences growth, bud dormancy, and cold acclimation
536 in *Vitis labruscana* and *V. riparia*. *Journal of the American Society for Horticultural Science*.
537 *American Society for Horticultural Science*, 116, 270-273. doi:10.21273/JASHS.116.2.270

538 Fracheboud, Y., Luquez, V., Björkén, L., Sjödin, A., Tuominen, H., & Jansson, S. (2009). The control of
539 autumn senescence in European aspen. *Plant Physiology*, 149(4), 1982-1991.
540 doi:10.1104/pp.108.133249

541 Gianelle, D., Cavagna, M., Zampedri, R., & Marcolla, B. (2016). FLUXNET2015 IT-MBo Monte
542 Bondone. In: FluxNet; Edmund Mach Foundation.

543 Gianelle, D., Zampedri, R., Cavagna, M., & Sottocornola, M. (2016). FLUXNET2015 IT-Lav Lavarone.
544 In: FluxNet; Edmund Mach Foundation.

545 Gough, C., Bohrer, G., & Curtis, P. (2016). FLUXNET2015 US-UMB Univ. of Mich. Biological
546 Station. In: FluxNet; Ohio State University; Virginia Commonwealth University.

547 Grubbs, F. E. (1950). Sample criteria for testing outlying observations. *Annals of Mathematical*
548 *Statistics*, 21(1), 27-58.

549 Hamilton, J. A., El, K. W., Hart, A. T., Runcie, D. E., Arango-Velez, A., & Cooke, J. E. (2016). The joint

550 influence of photoperiod and temperature during growth cessation and development of dormancy
551 in white spruce (*Picea glauca*). *Tree Physiology*, 36(11), tpw061.

552 Heide, O. M. (1974). Growth and Dormancy in Norway Spruce Ecotypes (*Picea abies*) I. Interaction of
553 Photoperiod and Temperature. *Physiologia Plantarum*, 30(1), 1-12. doi:10.1111/j.1399-
554 3054.1974.tb04983.x

555 Heide, O. M. (2001). Photoperiodic control of dormancy in *Sedum telephium* and some other
556 herbaceous perennial plants. *Physiologia Plantarum*, 113(3), 332-337.

557 Hörtnagl, L., Eugster, W., Buchmann, N., Paul-Limoges, E., Etzold, S., & Haeni, M. (2016).
558 FLUXNET2015 CH-Lae Laegern. In: FluxNet; ETH Zurich.

559 Hörtnagl, L., Eugster, W., Merbold, L., Buchmann, N., Etzold, S., Haesler, R., & Haeni, M. (2016).
560 FLUXNET2015 CH-Dav Davos. In: FluxNet; ETH Zurich.

561 Howe, G. T., Gardner GHackett, W. P., & Furnier, G. R. (1996). Phytochrome control of short-day-
562 induced bud set in black cottonwood. *Physiologia Plantarum*, 97(1), 95-103.

563 Ibrom, A., & Pilegaard, K. (2016). FLUXNET2015 DK-Sor Soroe. In: FluxNet; Technical University of
564 Denmark (DTU).

565 Janssens, I. (2016). FLUXNET2015 BE-Bra Brasschaat. In: FluxNet; University of Antwerp.

566 Junttila, O. (1980). Effect of photoperiod and temperature on apical growth cessation in two ecotypes of
567 *Salix* and *Betula*. *Physiologia Plantarum*, 48(3), 347-352.

568 Keskitalo, J., Bergquist, G., Gardeström, P., & Jansson, S. (2005). A cellular timetable of autumn
569 senescence. *Plant Physiol*, 139(4), 1635-1648. doi:10.1104/pp.105.066845

570 Klosterman, S. T., Hufkens, K., Gray, J. M., Melaas, E., Sonnentag, O., Lavine, I., ... Richardson, A. D.
571 (2014). Evaluating remote sensing of deciduous forest phenology at multiple spatial scales using
572 PhenoCam imagery. *Biogeosciences*, 11(16), 4305-4320. doi: [https://doi.org/10.5194/bg-11-
573 4305-2014](https://doi.org/10.5194/bg-11-4305-2014)

574 Knohl, A., Tiedemann, F., Kolle, O., Schulze, E.-D., Kutsch, W., Herbst, M., & Siebicke, L. (2016).
575 FLUXNET2015 DE-Hai Hainich. In: FluxNet; University of Goettingen, Bioclimatology.

576 Kramer, P. J. (1936). Effect of variation in length of day on growth and dormancy of trees. *Plant
577 Physiology*, 11(1), 127-137.

578 Law, B. (2016). FLUXNET2015 US-Me2 *Metolius* mature ponderosa pine. In: FluxNet; Oregon State
579 University.

580 Lund, M., Jackowicz-Korczynski, M., & Abermann, J. (2016). FLUXNET2015 DK-ZaH Zackenberg

581 Heath. In: FluxNet; Aarhus University.

582 Mammarella, I., Vesala, T., Keronen, P., Kolari, P., Launiainen, S., Pumpanen, J., ... Pohja, T. (2016).
583 FLUXNET2015 FI-Hyy Hyytiala. In: FluxNet; University of Helsinki.

584 Massman, B. (2016). FLUXNET2015 US-GLE GLEES. In: FluxNet; USDA Forest Service.

585 Matteucci, G. (2016). FLUXNET2015 IT-Col Collelongo. In: FluxNet; Istituto di Ecologia e Idrologia
586 Forestale CNR.

587 McCaughey, H. (2016). FLUXNET2015 CA-Gro Ontario - Groundhog River, Boreal Mixedwood
588 Forest. In: FluxNet; Queen's University.

589 Minerbi, S., & Montagnani, L. (2016). FLUXNET2015 IT-Ren Renon. In: FluxNet; Autonomous
590 Province of Bolzano, Forest Services.

591 Misra, G., & Biswal, U. C. (1973). Factors Concerned in Leaf Senescence. I. Effects of Age, Chemicals,
592 Petiole, and Photoperiod on Senescence in Detached Leaves of *Hibiscus rosa-sinensis* L.
593 *Botanical Gazette*, 134(1), 5-11. doi:10.1086/336672

594 Moors, E., & Elbers, J. (2016). FLUXNET2015 NL-Loo Loobos. In: FluxNet; ALTErrA / Wageningen
595 Environmental Research.

596 Munger, J. W. (2016). FLUXNET2015 US-Ha1 Harvard Forest EMS Tower (HFR1). In: FluxNet;
597 Harvard University.

598 Novick, K., & Phillips, R. (2016). FLUXNET2015 US-MMS Morgan Monroe State Forest. In: FluxNet;
599 Indiana University.

600 Oleksyn, J., Tjoelker, M. G., & Reich, P. B. (1992). Growth and biomass partitioning of populations of
601 European *Pinus sylvestris* L. under simulated 50° and 60°N daylengths: evidence for
602 photoperiodic ecotypes. *New Phytologist*, 120(4), 561-574.

603 Olmsted, C. E. (1951). Experiments on Photoperiodism, Dormancy, and Leaf Age and Abscission in
604 Sugar Maple. *Botanical Gazette*, 112(4), 365-393.

605 Paus, E., Nilsen, J., & Junttila, O. (1986). Bud Dormancy and Vegetative Growth in *Salix-Polaris* as
606 Affected by Temperature and Photoperiod. *Polar Biology*, 6(2), 91-95.

607 Rinne, P., Saarelainen, A., & Junttila, O. (1994). Growth cessation and bud dormancy in relation to ABA
608 level in seedlings and coppice shoots of *Betula pubescens* as affected by a short photoperiod,
609 water stress and chilling. *Physiologia Plantarum*, 90(3), 451-458.

610 Scott, R. (2016a). FLUXNET2015 US-SRM Santa Rita Mesquite. In: FluxNet; United States
611 Department of Agriculture.

612 Scott, R. (2016b). FLUXNET2015 US-Wkg Walnut Gulch Kendall Grasslands. In: FluxNet; United
613 States Department of Agriculture.

614 Shen, M., Zhang, G., Cong, N., Wang, S., Kong, W., & Piao, S. (2014). Increasing altitudinal gradient of
615 spring vegetation phenology during the last decade on the Qinghai–Tibetan Plateau. *Agricultural
616 and Forest Meteorology*, 189-190, 71-80. doi:10.1016/j.agrformet.2014.01.003

617 Šigut, L., Havrankova, K., Jocher, G., Pavelka, M., & Janouš, D. (2016). FLUXNET2015 CZ-BK1 Bily
618 Kriz forest. In: FluxNet; Global Change Research Institute CAS.

619 Varlagin, A., Kurbatova, J., & Vygorskaya, N. (2016). FLUXNET2015 RU-Fyo Fyodorovskoye. In:
620 FluxNet; A.N. Severtsov Institute of Ecology and Evolution.

621 Vermote, E. F. (2015). MOD09CMG MODIS/Terra Surface Reflectance Daily L3 Global 0.05Deg CMG
622 V006. In *NASA EOSDIS Land Processes DAAC*.

623 Vermote, E. F., Roger, J. C., & Ray, J. P. (2015). MODIS Surface Reflectance User’s Guide, Collection
624 6, Version 1.4. *MODIS Land Surface Reflectance Science Computing Facility*.

625 Wang, D. Y., Hu, S., Li, Q., Cui, K. M., & Zhu, Y. X. (2002). Photoperiod control of apical bud and leaf
626 senescence in pumpkin (*Cucurbita pepo*) strain 185. *Acta Botanica Sinica*, 44(1), 55-62.

627 Wilson, A. M., Parmentier, B., & Jetz, W. (2014). Systematic land cover bias in Collection 5 MODIS
628 cloud mask and derived products — A global overview. *Remote Sensing of Environment*, 141,
629 149-154. doi:<https://doi.org/10.1016/j.rse.2013.10.025>

630 Zhang, X. (2015). Reconstruction of a complete global time series of daily vegetation index trajectory
631 from long-term AVHRR data. *Remote Sensing of Environment*, 156, 457-472.
632 doi:10.1016/j.rse.2014.10.012

633 Zhang, X., Jayavelu, S., Liu, L., Friedl, M. A., Henebry, G. M., Liu, Y., ... Gray, J. (2018). Evaluation of
634 land surface phenology from VIIRS data using time series of PhenoCam imagery. *Agricultural
635 and Forest Meteorology*, 256-257, 137-149. doi:10.1016/j.agrformet.2018.03.003

636